University of Alberta

Nanostructured Inverted Organic Photovoltaic Cells

by

Michael Thomas

A thesis submitted to the Faculty of Graduate Studies and Research
in partial fulfillment of the requirements for the degree of

Doctor of Philosophy

in

Micro-Electro-Mechanical Systems and Nanosystems

Electrical and Computer Engineering

Spring 2013
Edmonton, Alberta

To my parents who helped me develop my will and character. To my grandparents whose true and unconditional love lights my inspiration. In memoriam Bernd Thomas.

ABSTRACT

Organic photovoltaic cells (OPVs)are promising devices for inexpensive power generation from sunlight. Organic semiconductors, the basic materials for OPVs, can be fabricated using a broad range of fabrication technologies from vapor deposition to solution processing. Upon light absorption, a strongly bound exciton is generated which can diffuse to a donor-acceptor heterojunction. At this interface it can be dissociated into free charge carriers which can be collected by the device electrodes. A major challenge for OPVs are short exciton diffusion lengths of up to 20 nm. Morphology engineering is required in order to harvest the exciton before it recombines and improve OPV performance.

This work focuses on the study of nanostructured morphologies for use in inverted architecture OPVs. Glancing angle deposition (GLAD)is employed to fabricate nanocolumnar acceptor films. Through combining these nanostructured C_{60} films with a conjugated polymer donor P3CBT and a small molecule 3-Q, inverted OPVs are fabricated with the goal to analyze effect of morphology engineering on device performance. A major challenge was that C_{60} were found to be soluble in most commonly used organic solvents such as dichlorobenzene or chloroform. Although this challenge has limited the donor choice and therefore has limited device performance, a significant effect of morphology engineering could be observed. All GLAD structured

C_{60} OPVs outperformed state of the art architectures such as planar films and bulk heterojunctions fabricated with the same materials. For P3CBT in particular the GLAD structured devices exhibited a twofold increase in power conversion efficiency compared with bulk heterojunctions and a fourfold increase compared with planar devices.

In a further study, the acceptor materials PTCDA and C_{60} were co-evaporated into a single film. PTCDA is stable against non-polar organic solvents while C_{60} provides a high electron mobility. Nanocolumnar acceptor blended PTCDA:C_{60} films were proven to remain stable when treated with dichlorobenzene. Furthermore, optical and electronic properties of these acceptor blends were investigated.

Acknowledgements

I would like to thank Dr. Michael Brett for the trust to invite me half-way around the world as his Ph.D. student. In addition, I would like to thank for Dr. Brett's strong mentorship which opened me a broad space to nourish my interests and strengths, for providing strong support, and for creating a strong research environment.

I would like to thank Dr. Jillian Buriak, Dr. Michael Taschuk, Dr. Ken Harris, Dr. Jeremy Sit, Dr. Michael Fleischauer for a marvelous academic leadership and helpful discussions which improved my work.

Brian J. Worfolk, Dr. David. D. Rider, Dr. Weiwei Li, Tate Hauger, Dr. Zhen Wang know the challenges of this work well as they have been a great support on the front lines, provided experimental solutions, and helped developing new approaches.

A big thank you as well to George Braybrook, master of scanning electron microscopy, and Ben Bathgate for "running a tight ship" in our lab. In addition, I would like to thank Dr. Dimitre Karpuzov for the surface characterizations and consulting on the results throughout my research.

I would like to thank Kyle Bothe for troubleshooting the OFET measurement setup and helpful discussions for interpreting the results.

I would like to thank Audrey Lin for the exceptional administrative support which allowed me to focus better on my research.

A big thank you to Dr. Louis Bezuidenhout who took the time to visit me in my home town Dresden and provided helpful insights about the Brett group and research in at the University of Alberta in exchange for a sightseeing tour through the city.

I would like to thank Dr. Jaron Van Dijken and Steven Jim for being great and supportive friends through the ups and downs of this research.

I would like to thank Dr. Katie Krause, Dr. Matthew Hawkeye, Dr. Jason Sorge, Allan Beaudry, Graeme Dice, Sumudu Fernando, Joshua Krabbe, Jonathan Kwan, Abeed Lalany, Graham Hunt, Ryan Shewchuk, Joshua Siewert, Daniel Smetaniuk, Ryan Tucker for creating a strong and fruitful research environment.

I would like to acknowledge funding from the Vanier Canada Graduate Scholarships, Alberta Innovates Technology Futures, the Killam Trusts, Micralyne Inc., the School of Energy and Environment at the University of Alberta, and the University of Alberta.

Finally, thank you to my parents, grandparents, and my brother Roman for the amazing support on this journey; a journey which introduced me to a new culture, a fascinating wild life, majestic mountains, and new friends.

Table of Contents

LIST OF TABLES

List of Figures

Symbols and Abbreviations

Symbols

α	Deposition Angle
β	Column tilt angle
γ	Angular amplitude of ϕ-sweep
Δ	Interface dipol
η	Efficiency
ε_0	Vacuum permittivity
ε_r	Dielectric constant
μ	Charge carrier mobility
ν	Wavelength
ϕ	Substrate polar rotation angle
Φ	Work function
A	Area
C	Capacitance
E	Energy
E_g	Band gap
$E_{cut-off}$	Secondary electron cut-off
EA	Electron affinity
FF	Fill factor

h	Planck constant
I_{ds}	Drain current
IP	Ionization potential
J	Current density
J_{ph}	Photocurrent
J_{SC}	Short-Circuit Current
k_B	Boltzmann constant
L	Transistor channel length
L_D	Exciton diffusion length
m	Mass
n	Charge carrier density
p	Pressure
P	Power
PCE	Power conversion efficiency
q	Charge
R	Resistance
R_{dep}	Deposition ratio
R_S	Series resistance
R_P	Parallel resistance
t	Film thickness
T	Temperature in Kelvin
T_m	Melting temperature
$U(x)$	Electric potential
V	Voltage
V_{bi}	Built-in potential
V_{ds}	Drain voltage

V_{gs}	Gate voltage
V_{OC}	Open-circuit voltage
V_{th}	Threshold voltage
W	Transistor channel width

Abbreviations

AM	Air mass
BHJ	Bulk heterojunction
C_{60}	C_{60} fullerene
CB	Chlorobenzene
CTM	Crystal thickness monitor
DCB	Dichlorobenzene
DMSO	Dimethyl-sulfoxide
EQE	External quantum efficiency
FWHM	Full-width at half maximum
GLAD	Glancing angle deposition
HOMO	Highest occupied molecular orbital
IPA	2-propanol
IQE	Internal quantum efficiency
ITO	Indium tin oxide
LUMO	Lowest unoccupied molecular orbital
MIM	Metal-insulator-metal model
MOSFET	Metal-oxide-semiconductor field-effect transistor
mpp	Maximum power point
NIR	Near infrared

NREL	National Renewable Energy Laboratory
OFET	Organic field-effect transistor
OPV	Organic Photovoltaic Cell
OTS	n-octadecyltrichlorosilane
P3HT	regioregular 2,5-diyl-poly(3-hexylthiophene)
P3CBT	poly[3-(4-carboxybutyl)thiophene-2,5-diyl]
PCBM	[6,6]-phenyl-C_{61}-butyric acid methyl ester
PL	Photoluminescence
PTCDA	perylene-3,4,9,10-tetracarboxylic dianhydride
PV	Photovoltaic
QCM	Quartz crystal microbalance
RIE	Reactive ion etch
SAM	Self-assembled monolayer
SEM	Scanning electron microscope
Si	Silicon
TEM	Transmission electron microscope
UPS	Ultraviolet photoelectron spectroscopy
UV	Ultraviolet
vis	Visible
WF	Work function
XPS	X-ray photoelectron spectroscopy
XRD	X-ray diffractometry

CHAPTER 1

INTRODUCTION

1.1 The Potential of Organic Photovoltaic Cells

Organic photovoltaic cells (OPVs) are widely researched with an exponentially increasing number of scientifically reviewed publications each year. OPV panels play a minor role in the PV market as it is a technology still in development [1,2], but present a strong opportunity for future power generation. OPV panels are a growing segment in the overall photovoltaic (PV) market. This world's PV market volume is shown in Figure 1.1, starting in year 2006 and forecasted until 2016 [1]. Despite drawbacks which can affect the industry in the short and mid term, the diagram shows overall exponential growth of cumulative installed PV capacity and revenues. Thus, the world is adapting PV technology at an increasing rate. Capacity has a slightly higher growth rate as compared to revenue which indicates that average PV prices are slightly decreasing due to increased competition and technology improvements. The compounded annual growth rate is 26.7% for revenues and 33.5% for cumulative installed capacity.

Strong exponential market growth is forecasted for the OPV industry [3–

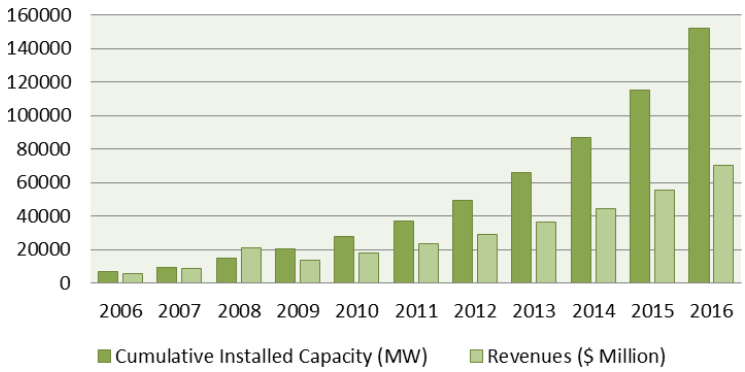

Figure 1.1. *Development of the cumulative installed capacity and revenues of the entire PV industry worldwide. Data acquired from [1]*

5], however these predictions have yet to be met. Being in a development stage however, the industry is still focused on product development in order to improve OPV panel quality. Critical success factors for OPV panels are cost, power conversion efficiency, device lifetime, and scalability [2]. In order to achieve successful market penetration, OPV panels must be stable and efficient at a low cost. However, these are competing factors: an increased efficiency could increase manufacturing cost, a higher lifetime might result in lower efficiency, etc.

1.1.1 Photovoltaic Industry Challenges

The drive for cost-effective, environmentally friendly energy production has been fuelled by an increasing societal focus on environment, climate and sustainable energy. Hence, the strongest factors driving the overall PV market are [1,2]:

1. Rising demand and increasing costs for fossil fuels;
2. Increasing need for energy diversification;
3. Government subsidies and economic incentives;

4. Increasing environmental concerns over conventional energy.

These market drivers are likely to become stronger in future years. PVs have been identified as potential game changers in the energy economy and their importance is therefore expected to increase. Due to these influential drivers there is a strong market pull for improved solar technology. However, for improved adoption by society, several challenges have to be resolved. Conventional solar projects require large capital investments and therefore have long payback periods. Governments are supporting solar projects through subsidies which can lead to a financial dependence of the conventional PV industry.

To be successful and to overcome these major challenges, PV products need to achieve a lower cost/power output and shorter energy balance and financial payback times, respectively. Although, further efforts are being made to improve public policy and integration in the electric grid, a major technological breakthrough can more likely address those challenges. Plastic solar panels could become a disruptive innovation due to potentially lower manufacturing costs.

1.1.2 Objectives and Outline of This Work

Organic photovoltaic (OPV) devices are promising candidates for low-cost solar cells [6–19]. This work analyzes the effect of morphology on the power conversion efficiency of OPVs in order to investigate possible routes for the improvement of their performance. State of the art architectures are solution-processed polymer blends or so-called bulk heterojunctions [7–9,11–13,15,18, 20,21].

It becomes obvious that there can be various perspectives on OPV re-

search as it involves topics from organic chemistry, optics, electronics, materials science, and nanotechnology in particular. Hence, the solution space in order to improve OPV technology is vast and broad. For this reason, this work will focus on the research and characterization of morphology engineering of OPV photoactive layers in particular. OPVs are limited by the exciton diffusion length in the active layer materials, and in order to improve performance morphology control is critical. The photoactive layer in bulk heterojunctions is typically disordered exhibiting pocket domains and dead-ends which can limit charge transport and thus overall device performance [11, 22–24]. In contrast, the fabrication process in this work utilizes glancing angle deposition (GLAD) which employs substrate rotation at oblique flux incidence in order to fabricate porous films [25, 26]. Due to this substrate motion a vertically oriented network of interpenetrating donor and acceptor columns can be deposited which promises to maximize charge transport and minimize trap states resulting from dead-ends [11, 27, 28].

The primary objectives for this thesis are:

- Fabrication and characterization of GLAD structured organic acceptor films;
- Infiltration of GLAD fabricated base layers with donor films and the analysis of these multilayers;
- Investigation of preparation routes for GLAD based inverted OPVs;
- Materials research of suitable acceptor layers for OPV fabrication.

After describing the theoretical background for the materials and methods used in this work and a description of experimental details, this thesis is structured in four main results and discussion chapters.

Chapter 4 - Morphologies for Inverted Organic Photovoltaic Cells presents various approaches for GLAD C_{60} film fabrication. Since C_{60} and its derivatives are the most fundamental acceptor materials for OPV devices, the morphology engineering possibilities of C_{60} films will be investigated.

Chapter 5 - Polymer Filled Organic Photovoltaic Cells discusses the fabrication of inverted architecture OPV devices with the use of a conjugated polymer poly[3-(4-carboxybutyl)thiophene-2,5-diyl] as the donor. Major challenges for GLAD structured inverted OPVs will be presented and discussed. Finding ways to address those challenges is the basis for the following two results chapters.

Chapter 6 - Small Molecule Filled Organic Photovoltaic Cells attempts to improve upon the previous devices fabricated by employing the star molecule donor 3-Q instead of using a conjugated polymer. In particular, the results in this chapter focus on improving the filling of a donor material into the GLAD fabricated nanostructured C_{60} films.

Chapter 7 - PTCDA:C_{60} Acceptor Blends for Organic Photovoltaic Cells investigates the blending of our GLAD C_{60} films with perylene-3,4,9,10-tetracarboxylic dianhydride (PTCDA) in order to improve the acceptor material itself for the use in inverted OPVs. Many of the significant shortcomings of C_{60} can be eliminated by using PTCDA.

Portions of this thesis were published or presented in references [29–32]:

- Michael Thomas, Brian J. Worfolk, David A. Rider, Michael T. Taschuk, Jillian M. Buriak, and Michael J. Brett. "C_{60} fullerene nanocolumns – polythiophene heterojunctions for inverted organic photovoltaic cells". *ACS Applied Materials & Interfaces*,3(6):1887 - 1894, 2011. Reference [29], doi: 10.1021/am200076m [Chapters 3, 4 & 5]

- Michael Thomas, Weiwei Li, Zhi-Shan Bo, and Michael J. Brett. "Inverted photovoltaic cells of nanocolumnar C_{60} filled with solution processed small molecule 3-Q". *Organic Electronics*, 13:2647 - 2652, 2012. Reference [30] doi: 10.1016/j.orgel.2012.07.039 [Chapter 3 & 6]

- Michael Thomas, Brian J. Worfolk, David A. Rider, Michael T. Taschuk, Jillian M. Buriak, and Michael J. Brett. "Controlling C_{60} Fullerene Nanocolumn Morphology For Organic Photovoltaic Applications". In *37th IEEE PVSC Proceedings*, pages 744 - 747, Seattle, 2011. IEEE, 345 E 47th St., New York, NY 10017 USA. Reference [31] doi: 10.1109/PVSC.2011.6186060 [Chapter 3 & 4]

- Brian J. Worfolk, David A. Rider, Anastasia L. Elias, Michael Thomas, Kenneth D. Harris, and Jillian M. Buriak. Bulk Heterojunction Organic Photovoltaics Based on Carboxylated Polythiophenes and PCBM on Glass and Plastic Substrates. *Advanced Functional Materials*, 21(10):1816 - 1826, 2011. Reference [32] doi: 10.1002/adfm.201100049 [Chapter 5]

- *"lightPower - Flexible Plastic Solar Cells Made in Alberta"*, Michael Thomas, Jaron G. Van Dijken, Brian J. Worfolk, business plan submitted to the Venture Prize, organized by TEC Edmonton, Edmonton, Canada, 2011. [Chapter 1]

- Michael Thomas, Ph.D. Candidacy Report, University of Alberta, Edmonton, Canada, 2010. [Chapter 1 & 2]

CHAPTER 2

GLANCING ANGLE DEPOSITION AND ORGANIC PHOTOVOLTAICS

2.1 Thin Film Deposition

Central for sample fabrication in this work is the thin film deposition of organic materials, metals, and oxides. Although a variety of materials from those three classes can be deposited, thin film deposition follows the same major laws for all three. The process can be separated in three steps. First, a source material is evaporated. Next, the resulting particles are transported to the substrate. Finally, the particles condense on the substrate and where they can form a solid film [33, 34]. Particles can be atoms, molecules, or ions. By controlling the film growth during condensation, film properties such as crystal structure, microstructure, electronic and optical properties can be determined.

For most processes in this work, thermal evaporation is used where the source material is vaporized in a resistance heated crucible. The evaporation rate for this thermal evaporation can be described by the Hertz-Knudsen

equation [35,36]:

$$\frac{dN}{Adt} = \frac{\alpha}{\sqrt{2\pi m k_B T}}(p^* - p) \tag{2.1}$$

The rate of evaporation or particle flux is described by dN/Adt which is the number of particles evaporated per source area and per time. α is the evaporation coefficient, k_B is the Boltzmann constant, T is the source temperature, m is the particle mass, and p is the process chamber pressure. The evaporation coefficient α is process dependent and influenced by e.g. source contamination. Most essential in the equation however is the material dependent vapor pressure p^*. This vapor pressure is a function of temperature. In order to generate a particle flux from thermal evaporation, the crucible with the source material is heated sufficiently high so that the vapor pressure exceeds the pressure in the process chamber. Typical process chamber pressures for organics evaporation in this work are about 1×10^{-7} *Torr*. Not only does this ultra high vacuum allow for sufficiently high evaporation rates, but in addition, this vacuum is required to avoid contamination of the deposited film and for the particle transport to the substrate.

In a gas state, particle transport can be defined by its mean free path, the distance of a particle travelled before it interacts with its surrounding particles. If the process chamber is under ultra high vacuum, this mean free path becomes larger than the characteristic dimensions of the chamber, allowing particles to travel in a trajectory without collision until they reach the substrate. This transport regime is also called molecular flow regime [34].

When the particles reach the substrate they can be reflected or adsorbed where through inter-particle interactions they can reach an energy minimum state which will trap them on the substrate surface. This energy minimum

can occur by physisorption or chemisorption. The former describes adsorption by van-der-Waals interaction while stronger bonding such as covalent bonding can occur if an activation energy is overcome for the latter. In both cases, the process is dynamic, i.e. particles can also be desorbed if they have sufficiently high energy to overcome the adsorption potential. The controlling parameter is substrate temperature, wherein a cold enough substrate will provide an adsorption potential so that an equilibrium is reached where the adsorption rate is higher than the desorption rate.

2.2 Nucleation and Film Growth

Adsorbed particles can lead to film growth which can be described as a multi-step process [33, 34]. During the island stage, physisorbed particles may be mobile on the substrate surface and surface diffusion can occur when the particle energy is high enough for it to move on the substrate but too low to desorb. These surface diffusing particles can interact in an ensemble and form a cluster or nuclei. A nuclei's surface area-to-volume ratio determines its probability of evaporation. A nuclei volume needs to be large enough to achieve a sufficiently low surface-area-to-volume ratio. When this critical nucleus size is reached, the nucleus is stable, i.e. the rate of desorbed surface particles is less than the rate of surface-diffusing particles which lead to an increasing island or nucleus size. In the coalescence stage, islands grow further and can coalesce with other. In channel stage a sufficient number of islands is connected leaving only channels and holes of the substrate exposed. Finally, a continuous film is formed when all of the substrate area is covered. This island formation is dependent on various factors, in particular substrate temperature, process chamber pressure, particle bonding with the

substrate, and substrate cleanliness.

The surface tension of a film on a substrate can lead to different growth modes [37, 38]. When the film surface tension exceeds the surface tension of the substrate, then the contact angle of the nuclei on the substrate is high enough to lead to island growth or Volmer-Weber growth. In the opposite case a low film surface tension allows the nuclei to wet the substrate and layer-by-layer growth or Frank-van der Merwe growth is preferred. In an intermediate mode, Stranki-Krastanov growth occurs where several monolayers of the film are grown before the nuclei start islanding.

2.2.1 The Structure Zone Model

One predominant parameter for thin film growth is substrate temperature. Movchan and Demchishin therefore proposed a structure-zone model that introduces three regimes for thin film growth morphology dependent on the ratio between substrate temperature T and the melting temperature of the deposited film material T_m, shown in Figure 2.1. In Zone 1 ($T/T_m < 0.3$), substrate temperature is sufficiently low that surface diffusion of adsorbed particles is low. During deposition, particle shadowing creates column- or dome-like structures and due to the low surface diffusion of the adsorbed particles, this columnar structure cannot be overcome leading to a high number of voids in the film. When the substrate temperature is sufficiently high ($0.3 \leq T/T_m < 0.5$), particle surface diffusion can overcome the columnar morphology from shadowing leading to a continuous film with columnar grains. For very high substrate temperatures ($T/T_m \geq 0.5$), not only surface diffusion but also diffusion in the bulk of the film and recrystallization can occur leading to a continuous, fully annealed film with little defects.

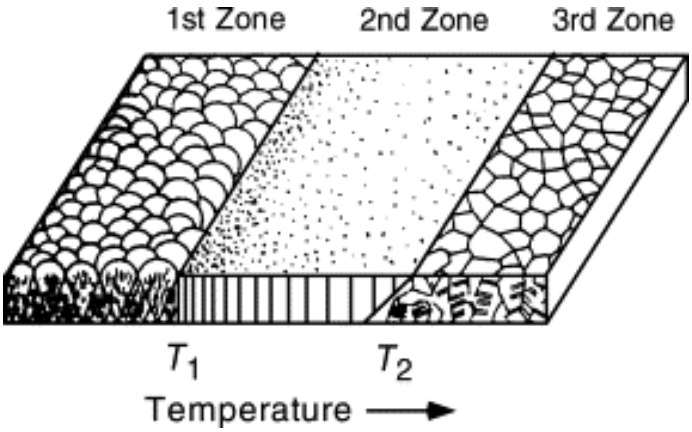

Figure 2.1. *Structure Zone Model, adapted from [39]. Three zones are defined depending on the melting temperature of the deposited material. The first zone is the most beneficial for glancing angle deposition.*

2.3 Glancing Angle Deposition

For growing columnar thin films, central to this work, glancing angle deposition (GLAD) is utilized. GLAD involves the deposition of thin films at oblique angles α [40–44] while in addition applying a substrate motion algorithm in order to build a variety of morphologies [45].

For GLAD, ballistic shadowing of the incoming particle flux is used to provide columnar growth as described in zone 1 of the structure zone model (as shown in section 2.2.1). In order to maximize the shadowing effect a collimated particle flux is necessary. This can be achieved by either setting up a large distance between source and substrate or by collimating the particle flux by using a physical cover or aperture. In addition, the ultra high vacuum in the chamber allows for a large mean free path of the particles which additionally improves collimation.

The general principle for GLAD is described in Figure 2.2. At the beginning of the deposition, islands of particles can be randomly formed on the substrate which will increase its roughness. As those islands grow into

columns, shadows will develop intensifying this columnar growth. Since the process of forming islands on the substrate and the amount of incoming particle flux are random, these shadows not only prevent new island formation but also larger columns can shadow their smaller neighbours during growth. Through this process a column can entirely overshadow its neighbours and suppress their growth while intensifying its own growth. This column extinction leads to a column height distribution as well as a column broadening of the larger columns. The overall degree of shadowing is controlled by adjusting the substrate tilt angle or deposition angle α where shadowing increases with larger α. When no substrate motion is applied, columns will be tilted by an angle β. This column tilt angle is normally observed to be lower than the deposition angle α [46–50].

When additionally applying a substrate motion algorithm, various morphologies as shown in Figure 2.3 can be achieved. This work focuses on vertical columns which can be generated by applying a constant substrate rotation during deposition [51].

2.3.1 An Advanced Motion Algorithm: ϕ-Sweep

Ballistic shadowing behaves anisotropically and when no substrate rotation is applied columns will grow wider in the direction perpendicular to the direction of the incoming particle flux. For some applications thinner columns might be preferred for which shadowing needs to be reduced. In order to reduce column broadening and suppress column extinction effects, the ϕ-sweep method can be applied [53].

Figure 2.4 shows the geometry during ϕ-sweep. A substrate motion is employed where the substrate is rotated with the angular amplitude γ to $(\alpha, \phi + \gamma)$ and held in that position for a defined film thickness. When that

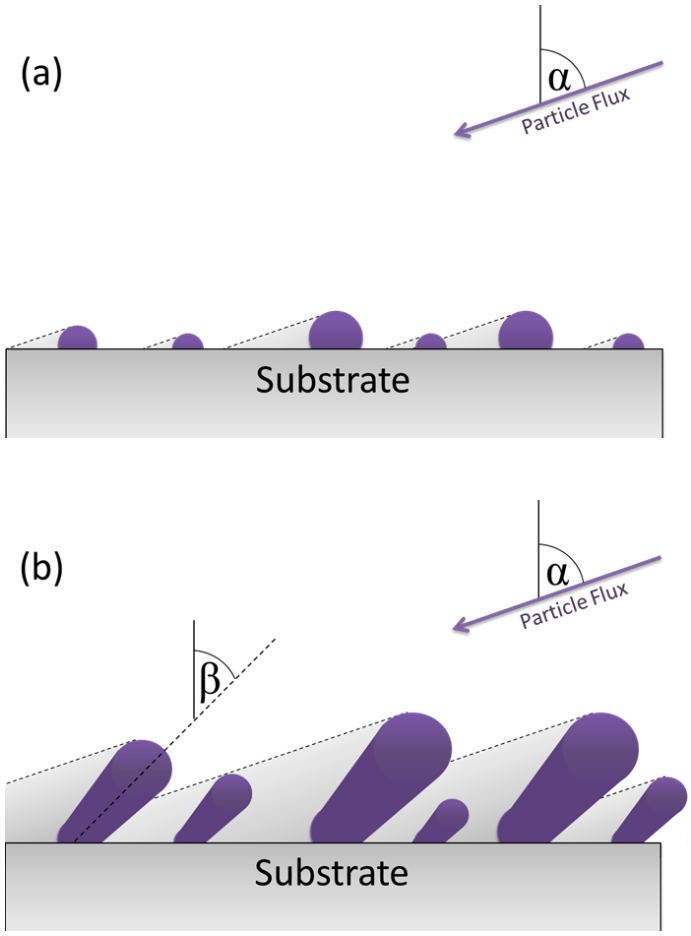

Figure 2.2. *The effect of ballistic shadowing when depositing at a high substrate angle of α and no substrate rotation. (a) Individual islands are formed with random size distribution and random distance from each other. (b) Due to ballistic shadowing, particle flux cannot deposit in-between islands, therefore voids develop and columnar growth occurs. Column extinction is illustrated, where smaller columns are overshadowed by their larger neighbours and seize to grow. The column angle β is the average tilt angle of all columns relative to the substrate normal.*

thickness or pitch is reached, the substrate is rotated by the same angular amplitude in the opposite direction and held at $(\alpha, \phi - \gamma)$. Because of this rotation algorithm a column symmetry is achieved where the column growth follows a central axis (α, ϕ).

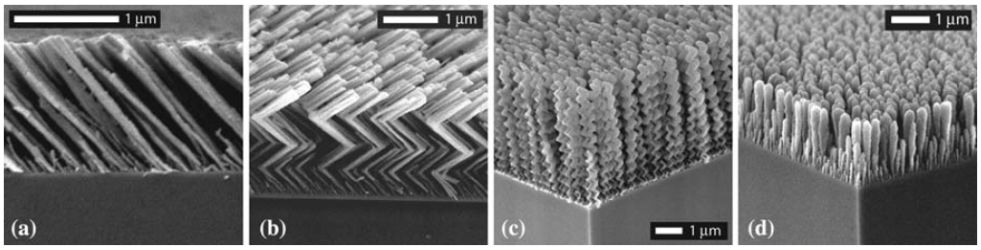

Figure 2.3. *GLAD structured silicon films grown on silicon substrates at a given deposition angle α (a) Slanted columns, no rotation. (b) Chevrons – discrete rotation of ϕ in 180° steps. (c) Helices – low substrate rotation speed. (d) Vertical columns – high substrate rotation speed. Springer, Journal of Materials Science: Materials in Electronics 18(4) 2006, Nanostructure engineering in porous columnar thin films: recent advances, J. J. Steele and M. J. Brett, Fig 3, with kind permission from Springer Science and Business Media. [52]*

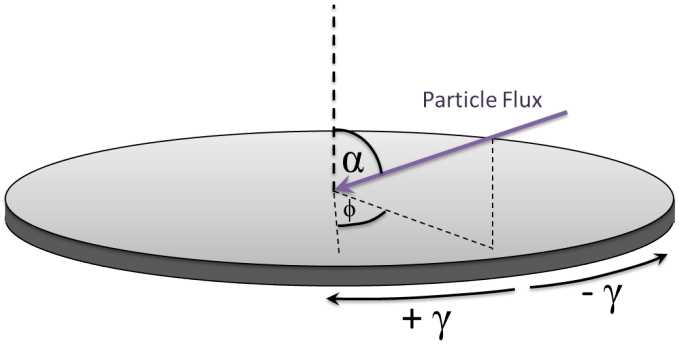

Figure 2.4. *Deposition geometry during phi-sweep. Particle flux reaches the substrate at the substrate angle α. Before deposition the substrate is rotated to the azimuthal idle state described by ϕ. During deposition, the substrate is oscillated around that idle state with the angular amplitude γ.*

2.4 Photovoltaic Cells

Photovoltaic cells (PV cell) convert light such as sunlight to electrical power. In the simplest case a PV cell is made of a p-n junction, as shown in Figure 2.5. Upon light absorption an electron is elevated into the conduction band and an exciton is created. Depending on the material in which the exciton is generated, it has a lifetime after which it will recombine while either emitting radiation or thermal energy [54]. In conventional PV cells this Mott-Wannier

exciton has a small binding energy. Therefore, free charges are generated when the exciton is generated [54]. The free charge carriers are then transported to the electrodes of the device and harvested at the electrodes.

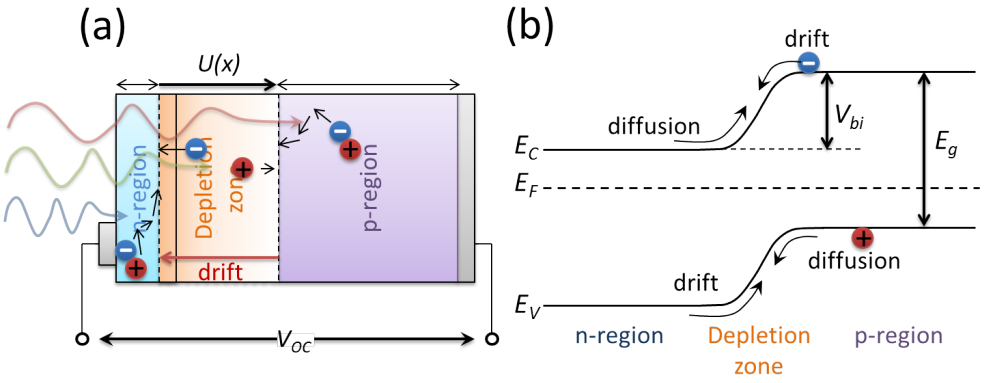

Figure 2.5. *Conventional Silicon (Si) PV cell operation (one-dimensional illustration). (a) The n-doped region and p-doped region of the Si PV cell is shown with a depletion zone separating them which has the electrical potential $U(x)$. Depending on the wavelength of the incident light, excitons are created in the bulk of the cell which can diffuse to the depletion zone where they will be separated into free charge carriers by the built-in potential. As a result the open-circuit voltage V_{OC} is generated. (b) Corresponding Band Diagram. E_C is the conduction band while E_V represents the valence band. E_F is the Fermi level and E_g the electronic band gap. V_{bi} represents the built-in potential.*

2.4.1 Solar Simulation and Equations for Exciton Generation

Since the primary application of PV cells is to convert sunlight to electricity, PV cells have to be optimized to the solar spectrum [54]. Generally, the raw solar spectrum is nearly equivalent to black body radiation at 5800 K. However, when testing PV cells the solar spectrum which is simulated, is the so-called air mass or AMx spectrum, where x is the normalized thickness of air the sunlight has to pass to reach the Earth's surface [54]. When sunlight reaches the Earth's atmosphere it is defined as AM0, as shown in Figure 2.6. When sunlight passes through the atmosphere vertically, it could be denoted

as AM1. As the sunlight travels through the atmosphere it is diffused by scattering with particles in the atmosphere. Therefore, the AM1 spectrum has an overall lower irradiance. However, since it is more practical to take latitude into account where sunlight would pass through the atmosphere on a tilted trajectory, the AM1.5 spectrum is used for simulation. The AM1.5 is the irradiance of sunlight at a latitude of 48.2° and has a total irradiance of 100 $mWcm^{-2}$ [55]. This is also the spectrum simulated when testing PV cells in a laboratory environment [56].

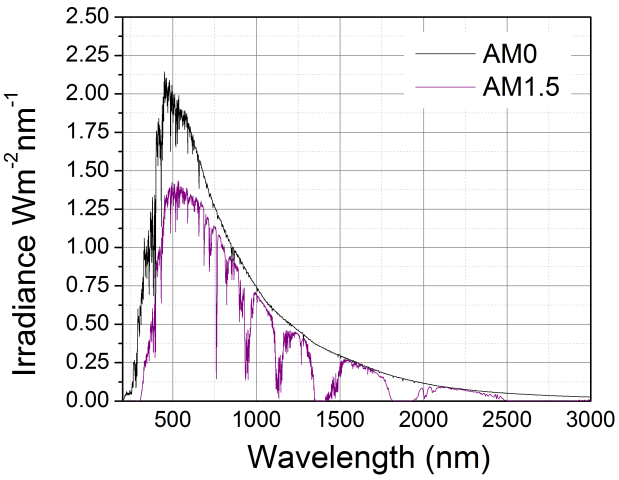

Figure 2.6. *AM0 and AM1.5 spectrum. Raw data provided by [55].*

2.4.2 Photovoltaic Cell Operation

Since the principle of the PV cell is based on a p-n junction, it can be modeled as a closed circuit of a diode and a load resistance in the simplest case. However, since a PV cell can operate under light conditions where it would generate free charges, an additional element for the generated photocurrent J_{ph} is to be added in parallel to the circuit. Also, resistance plays a major role in PV

cell operation. A series resistance R_S in the circuit represents inefficiencies from processes such as injection or contact resistance at the electrodes [54]. In addition, a parallel resistance R_P accounts for losses from leakage currents. The resulting model circuit is shown in Figure 2.7.

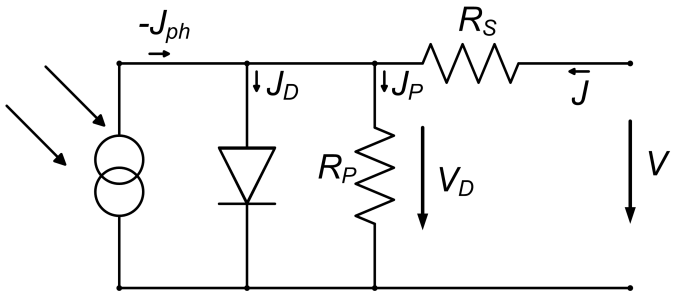

Figure 2.7. *Circuit Model for a PV Cell. Series resistance is represented by R_S while parallel resistance is R_P. The p-n junction is accounted for by the diode element and diode current J_D and diode voltage V_D. J_{ph} represents the generated photo-current which is directed in the opposite direction of J_D.*

An equation for this circuit model would be a diode equation [54] as described in Equation 2.2:

$$J = J_0 \left[\exp\left(\frac{q(V - JR_S)}{nk_BT} \right) - 1 \right] + \frac{V - JR_S}{R_P} - J_{ph} \tag{2.2}$$

where k_B is the Boltzmann constant, T is the temperature, q is the charge, and n accounts for the ideality of the diode. Note the sign of J_{ph}; compared with the diode current, the generated photo current J_{ph} flows in the opposite direction. Figure 2.8 shows a schematic for the resulting $J - V$ characteristics of a PV cell. From this measurement several key performance parameters can be determined.

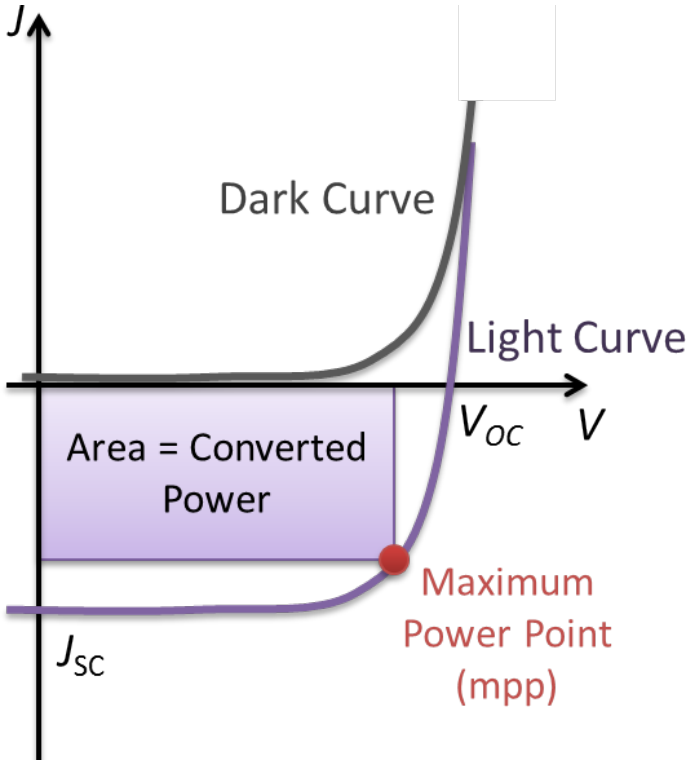

Figure 2.8. *The $J-V$ Characteristics of a PV Cell. Short-circuit current is shown as J_{SC} and open circuit voltage is represented by V_{OC}. The maximum power point mpp is where the area in the converted power rectangle is at maximum. The dark curve is measured when the PV cell operates at no external light, while the light curve is ideally the same curve shifted by the photo-generated short-circuit current.*

2.4.3 Performance Parameters of Photovoltaic Cells and their Physical Origins

In the following we will discuss performance parameters for PVs more in detail and describe their physical origin.

Short-Circuit Current. The short-circuit current J_{SC} is the maximum photo current density J_{ph} which can be obtained from the PV cell under illumination. J_{SC} represents the total amount of free charge carriers generated from exciton dissociation and thus is proportional to light absorption, the number of harvested excitons, and their dissociation efficiency. Therefore, the

short-circuit current is highly dependent on the morphology of the device and charge transport through it. In order to improve J_{SC}, light absorption, exciton harvesting, or charge transport should be increased [54].

Open-Circuit Voltage. Another performance indicator is the open-circuit voltage V_{OC}. The physical origin of V_{OC} in organic PVs is still debated. Most commonly, the V_{OC} is described as being mainly controlled by the energy offset at the donor-acceptor interface and less significantly by the difference in work function at the electrodes. For ohmic or quasi-ohmic contacts, the maximum open circuit voltage is limited by the difference of the highest occupied molecular orbital (HOMO) of the donor and the lowest unoccupied molecular orbital (LUMO) of the acceptor [54, 57, 58]. However, V_{OC} can be less than this difference due to exciton recombination or energetic losses at the junctions [59]. In particular, the metal-semiconductor interfaces play an important role for V_{OC} due to the formation of interface dipoles which can change the effective work function of the metal [60]. In order to increase V_{OC} the donor-acceptor combination and electronic structure can be changed, in addition charge recombination at interfaces and shunt losses should be minimized.

Fill Factor. The fill factor FF measures the ratio of the actual power obtained from the PV cell divided by the theoretically maximum obtainable power:

$$FF = \frac{Maximum\ Power\ Measured}{Theoretical\ Limit\ to\ Maximum\ Power} \tag{2.3}$$

$$= \frac{J_{mpp} \times V_{mpp}}{J_{SC} \times V_{OC}} \tag{2.4}$$

The maximum power measured of the PV cell is obtained by multiplying J_{mpp} and V_{mpp}, i. e. the current and voltage at the maximum power point

of the $J - V$ light curve [54]. When compared with the diode equation for PV operation, Equation 2.2, it becomes obvious that FF is equivalent to the ideality factor n of the PV cell. Reduction of FF can be due to a high serial resistance at the OPV contacts and low shunt resistance. A very low shunt resistance leads to a decrease of V_{OC} whereas a high serial resistance leads to lower J_{SC} [54]. In order to improve FF, resistance needs to be minimized. A detailed discussion of resistance and their physical origin is described in the following section.

Power Conversion Efficiency. All of these parameters together determine the power conversion efficiency of a photovoltaic cell. Power conversion efficiency (PCE) is calculated by

$$PCE = \frac{P_{out}}{P_{in}} \tag{2.5}$$

where P_{in} is the intensity of the incident light and P_{out} is the generated electrical power. Together with the parameters defined above this equation can be resolved to [61]:

$$PCE = \frac{J_{SC} \times V_{OC} \times FF}{P_{in}} \tag{2.6}$$

The intensity of the incident light is determined by the AM1.5 spectrum. Therefore, in order to maximize PCE, short-circuit current, open-circuit voltage, and fill factor need to be maximized.

2.4.4 Physical Origin and Influence of Resistance on Photoconversion Efficiency

During operation of a PV cell at a given architecture, the fill factor can be used to determine how close a particular PV cell sample operates to its optimum

which is determined by that architecture. A loss in the FF can be understood by the influence of parallel and series resistance on PV cell operation. Figure 2.9 illustrates a two main cases where resistance is not ideal [54]. Figure 2.9(a) describes the ideal operation of a PV device where parallel resistance is unlimited and series resistance is zero. Figure 2.9(b) however shows the device behavior if the parallel resistance R_P is small. In this case, leakage currents lead to a reduction in V_{OC} and thus FF and PCE decrease. This behaviour can be estimated by obtaining the slope of the light curve at $(V = 0, J_{SC})$. On the other hand a non-zero series resistance R_S also decreases the FF, as shown in Figure 2.9(c). A non-zero series resistance decreases J_{SC}, i.e. lowers the photocurrent or free charges harvested. The effect of series resistance can be estimated by measuring the tangent slope of the $J - V$ curve in the fourth quadrant.

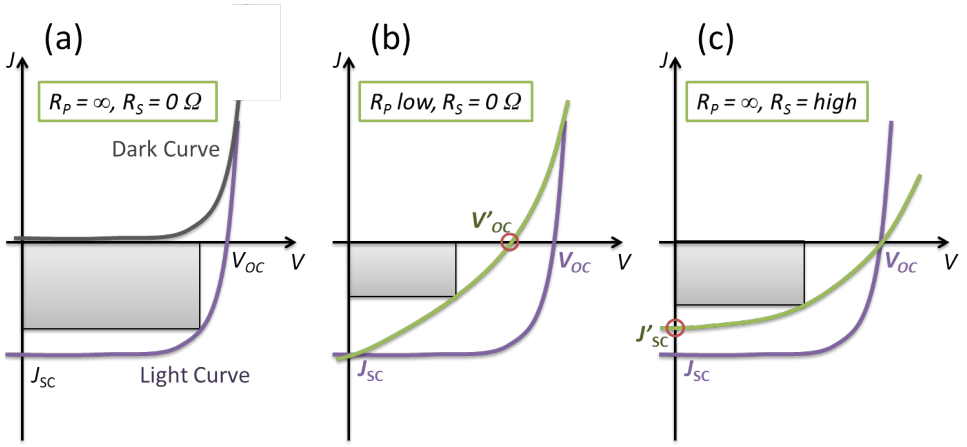

Figure 2.9. *Influence of Resistance on PV Cell Operation [54]. (a) Ideal PV operation with an unlimited parallel resistance R_P and zero series resistance R_S. (b) Low parallel resistance increases leakage current and thus decreases V_{OC}. (c) High series resistance R_S decreases the short-circuit current J_{SC}.*

The series resistance or internal resistance of the PV cell can have various origins. R_S has been described as sensitive to fabrication where improved

molecular ordering or crystallinity have increased charge mobility [62, 63]. In addition, the series resistance can depend on the device's electronic structure which controls charge injection into electrodes, hence interfacial layers are employed to decrease R_S [64]. In essence however, for optimized devices on small areas the series resistance plays only a minor role and becomes dominant when increasing device area due to the sheet resistance of the electrodes [65, 66].

Low shunt resistance or parallel resistance is present when the current can take an alternative path through the cell and does not contribute to the photocurrent. These leakage currents can occur due to defects in the photoactive layer or at the interface layers. Localized hot spots on the cell area indicate shunt losses. These spots occur due to inhomogeneous coating of the layers where direct contact exists between both electrodes or between electrode and photoactive layer, bypassing the interface layer [67]. Another aspect of leakage current can be understood as charge recombination which decreases the maximum possible photocurrent. Such recombination can occur at defects which can promote the recombination of an electron from the conduction level to the valence level. Defects can occur as localized disordered structures in the photoactive layers however also inefficient energetic offsets at electronic interfaces can lead to a fraction of electrons recombining.

2.5 Principles of Organic Electronics

2.5.1 Materials for Organic Photovoltaic Cells

In most cases, OPVs are built from small molecules [68] or on conjugated polymers [11, 59, 69]. In order to provide a short introduction to the properties of organic semiconductors, conjugated polymers will be used here as an

example. Conjugated polymers provide bonding states where carbon atoms can provide free charge carriers. In most cases, carbon atoms in conjugated polymers have four valence electrons, three of which contribute to the bonding of atoms through σ-orbitals. The left-over fourth electron is situated in the pz-orbital of the atom. It forms a π-system with adjacent carbon atoms resulting in quasi-delocalized electrons and leading to alternating single-bonds and double bonds in the polymer chain [54]. This allows for π to π^* transitions which enable the absorption of light in the visible spectrum and charge transport [54, 59]. The energy level of the π-state is called highest occupied molecular orbital (HOMO) and the energy level of the π^* state is called lowest unoccupied molecular orbital (LUMO).

Conjugated polymers can be insulators or semiconductors depending on the conjugation length, degree of ordering, or carrier density [54]. Carrier density of the electrons in the polymer backbone can be altered by doping or light-induced photocarrier generation. The conjugation length of the polymer, i.e. the length of the delocalized π electron state in the molecule, determines the conduction bandwidth within the molecule [11, 69, 70]. The bandwidth is larger along the polymer chain than perpendicular to it and thus the highest charge transport occurs along the polymer chain [71]. In well-ordered systems band transport dominates when the conduction bandwidth is much larger than the thermal excitation energy $k_B T$, where k_B is the Boltzman constant and T the temperature. However, when conjugated polymers are disordered, the overlap between wave functions of adjacent sites decreases. In this case thermally-assisted hopping transport between molecules becomes more dominant and overall charge transport decreases.

2.5.2 The Metal-Organic Semiconductor Junction

Charge injection is critical for efficient operation of organic semiconductor devices, in particular OLEDs, OFETs, and OPVs [72]. For an ideal injection, contacts are Ohmic, where the potential barrier at the contact is negligible and the current density follows the Ohm's law, i.e. is direct proportional to the applied voltage [73]. In particular, the contact resistance at an Ohmic contact is significantly lower than the resistance in the bulk. For organic electronics, a nominally high contact resistance can still be considered "Ohmic" if the resistance through the bulk of the organic semiconductor is significantly larger [74]. Most importantly, conductance through an organic semiconductor device is not injection limited if all contacts are Ohmic.

Figure 2.10 illustrates a simple organic diode with electron and hole injection into the organic semiconductor. In this simple case, electrons can be injected from the Fermi level of the cathode onto the lowest unoccupied molecular orbital (LUMO). For hole injection, a high work function metal anode can inject holes into the highest occupied molecular orbital (HOMO) of the organic semiconductor.

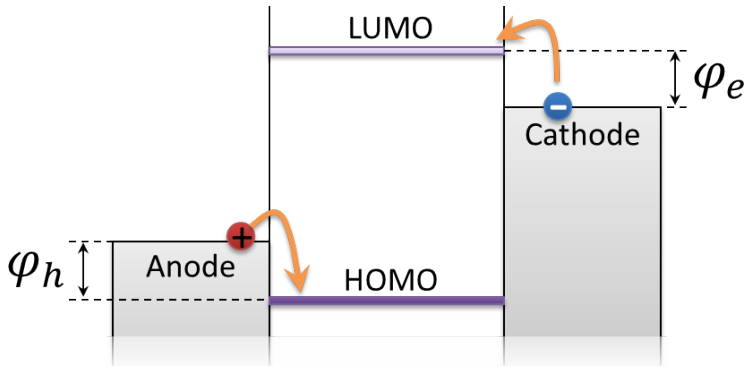

Figure 2.10. *Simple organic diode operation where electrons are injected into the LUMO and holes are injected into the HOMO of the organic semiconductor. Potential barriers are shown by ϕ_e for the electron injection and ϕ_h for hole injection.*

The potential barrier ϕ at the contact interface can sometimes be determined by the Mott-Schottky rule where the vacuum level of the metal is aligned with the vacuum level of the semiconductor [74], as shown in Figure 2.11 a. In this case a valid approximation for the potential barrier for electron injection at the interface is the difference between the LUMO level and the work function of the metal. Often however, an interface dipole is present at the contact interface and can result in an offset between the vacuum levels of the metal and semiconductor, as shown in Figure 2.11 b. This offset can lead to various complex phenomena. In particular, for metal-conjugated polymer junctions, interfacial electron transfer can result in an interface dipole. Additionally, the energy levels of the organic film can get pinned to the Fermi level of the metal by means of charge transfer between the metal and organic film, effectively resulting in an Ohmic contact [75–77].

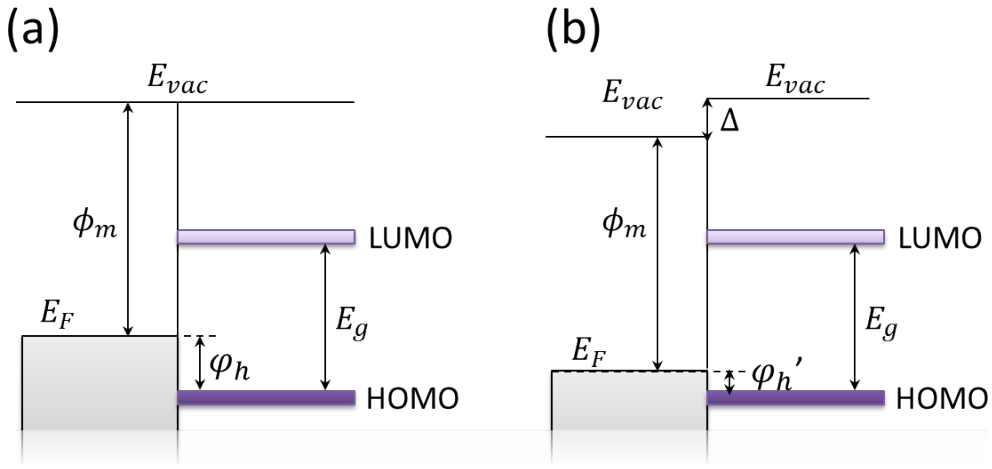

Figure 2.11. *(a) A metal-organic semiconductor interface where the Mott-Schottky rule holds, thus the vacuum level E_{vac} is constant. (b) A metal-organic semiconductor interface with an additional surface dipole Δ which can lead to an offset in the vacuum level E_{vac}. Adapted from [74].*

Overcoming the injection barrier can occur by either thermionic emission or tunneling [73], as shown in Figure 2.12 a,b. When an external electrical

field is applied, charges can tunnel through a potential barrier in the latter case while for thermionic emission, thermally excited electrons can pass over that barrier. If conductance in the semiconductor is high, this injection can be a limitation and lead to an increase in series resistance for an OPV.

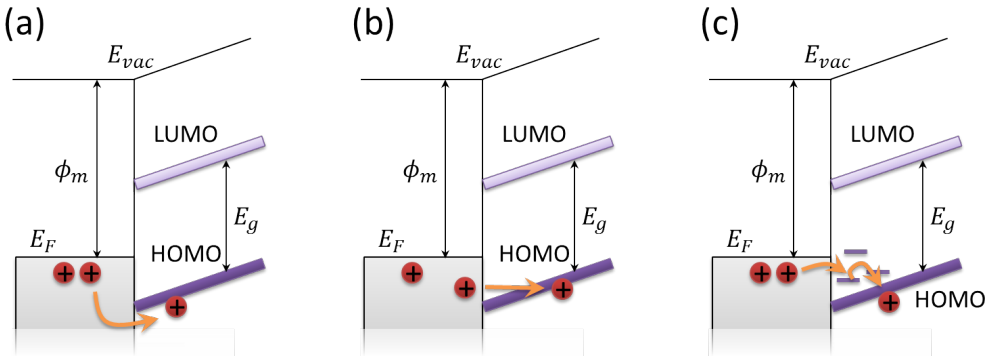

Figure 2.12. *Illustration of different injection modes at a metal-organic semiconductor junction with an applied external voltage. (Adapted from [74]) (a) Thermionic emission of holes from the Fermi level E_F of a metal into the HOMO of an organic semiconductor. (b) Tunneling of a hole directly onto a HOMO level. (c) Defect-assisted injection where charges can use intermediate defect-generated energy states which effectively lower the barrier between the Fermi level and the HOMO.*

Often however, organic semiconductors are disordered and therefore a variety of random electronic states can exist at the metal-organic semiconductor interface [74] and defect-assisted injection can occur, as shown in Figure 2.12 c. The existence of additional electronic states facilitates an easier charge carrier injection, however is detrimental for charge transport in the bulk [74].

Throughout this section, junctions have been described as flat band diagrams. In conventional metal-semiconductor interfaces, i.e. a Schottky contact, Fermi level alignment occurs when metal and semiconductor are in contact [73]. This Fermi level alignment can lead to band bending resulting in a Schottky barrier when the work function of the metal is not equal to the work function of the semiconductor. The depletion width of this band bending

decreases with increasing doping concentration in the semiconductor [73]. Organic semiconductors, however, have often an instrinsically low charge carrier concentration. As a result, the depletion zone could be several meters long and can therefore be neglected in this case [78–80], i.e. commonly little to no bend bending occurs at a metal-organic semiconductor (undoped) interface.

2.5.3 Charge Transport in Organic Materials

Charge carriers in organic semiconductors are highly localized [11, 81], since the bonding between molecules is weak and usually by van-der-Waals forces. Since there is little molecular orbital overlap between adjacent molecules, hopping needs to occur for intermolecular charge transport [82, 83]. Various modelling approaches were used for this hopping process with H. Bässler's model being the most commonly applied [84, 85].

As a macroscopic model and for simplicity however, the Mott-Gurney law [86] for space-charge-limited current J is used:

$$J = \frac{9}{8}\varepsilon_0\varepsilon_r\mu\frac{V^2}{t^3} \tag{2.7}$$

where ε_0 is the electric constant, ε_r is the dielectric constant, μ is the charge carrier mobility, V is the voltage, and t is the length measured such as e.g. device thickness. Commonly, at low voltage injection dominates current, however, at higher voltages space charge is the main limitation for current in organic semiconductors [54].

Champion mobilities are shown in Table 2.1 [87] and it becomes obvious that mobilities in organic semiconductors are commonly lower then in their crystalline inorganic counterparts.

Table 2.1. *Champion mobilities of a selection of organic donor and acceptor materials [87].*

Material	Mobility ($cm^2V^{-1}s^{-1}$)	Type	Reference
C_{60}	8×10^{-2} to 3×10^{-1}	*n*-type	[88]
$C_{60}(0.9)/C_{70}(0.1)$	10^{-4}	*n*-type	[89]
PTCDA	10^{-5} to 10^{-4}	*n*-type	[83]
F_{16}CuPc	3×10^{-2}	*n*-type	[90]
Polythiophene	10^{-5}	*p*-type	[91]
P3HT	10^{-1}	*p*-type	[92]
Pentacene	1.5	*p*-type	[93]

2.6 Organic Photovoltaic Cells

Compared with most PV technologies, organic photovoltaic cells yield the lowest efficiency [94], as shown in Figure 2.13. A high number of research publications in the organic photovoltaic cell (OPV) community focus on offsetting this efficiency loss by researching OPV fabrication techniques which are readily scalable and thus cheaper than from comparative technologies [95]. This work however is not aiming at investigating cheaper manufacturing techniques for OPVs but provides insight into the optimal structuring and architecture of an OPV.

Probably the key difference between OPVs and conventional PV cells is in the exciton generated. In OPVs, the exciton generated from light absorption has a stronger binding energy than conventional PV cells. Therefore, in order to dissociated this exciton and to generate free charge carriers, the binding energy of this exciton has to be overcome [57, 61, 96, 97]. Brian A. Gregg has coined the term *excitonic solar cells* in order to describe this exciton dominated nature of OPVs [98, 99].

Generally, the dielectric constant in an organic photoactive layer is significantly lower than in inorganic photoactive layers [98, 99]. The distance

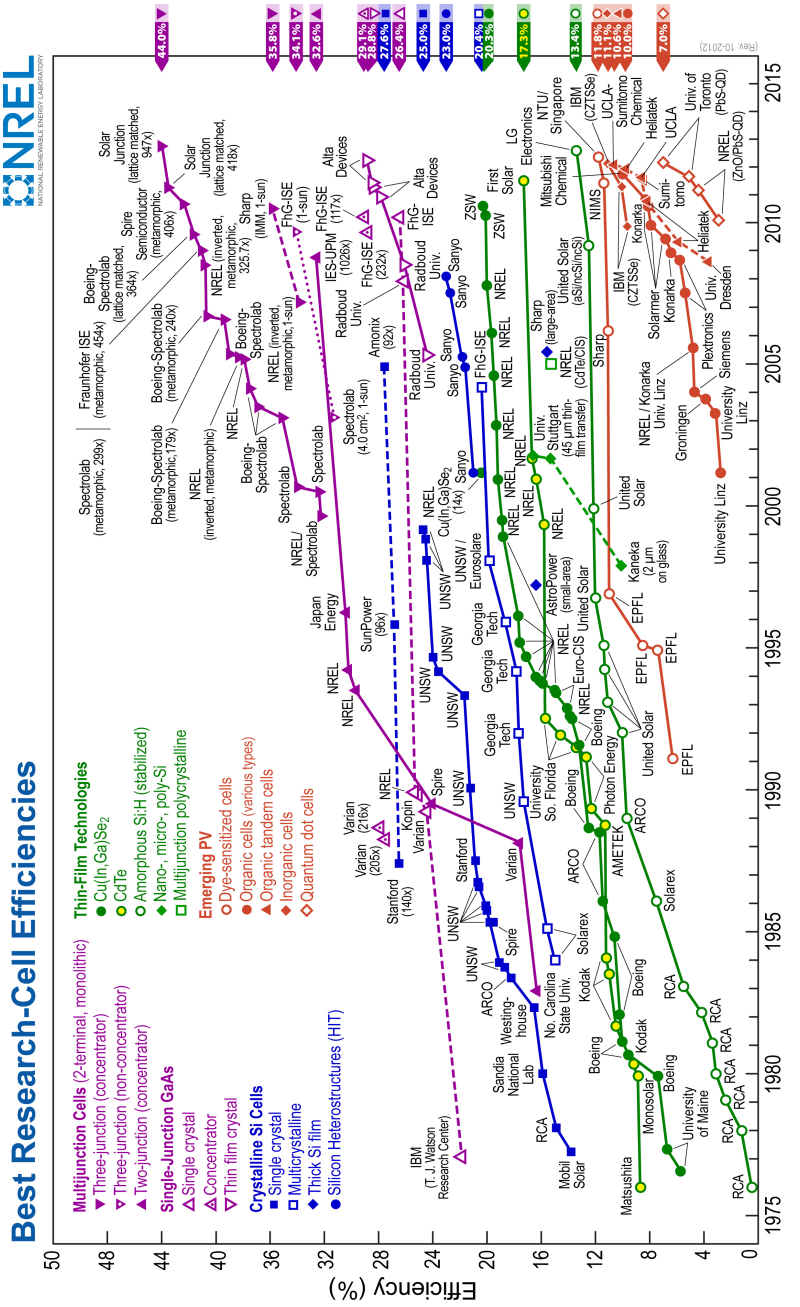

Figure 2.13. *Current Best Research PV Cell Performance, adapted from [94]. OPV research is comparably young and best multi-junction OPVs can reach up to 11.8 % PCE.*

between an electron and a hole decreases when this exciton is generated in a lattice with lower polarization or dielectric constant. This exciton is described as Frenckel exciton and has a strong binding energy [61, 97–99]. In order to dissociate this electron-hole pair, an energy overcoming the binding energy of the exciton needs to be applied. An interface with a change in potential such as a built-in voltage can separate the electron-hole pair if the potential difference is larger than the binding energy of the exciton.

Figure 2.14 shows a comparison between the process of exciton generation in a conventional PV cell compared with an OPV [14]. First it becomes obvious that while there is a depletion zone in conventional PVs where the Fermi levels of the p-n junction align and cause band bending, this does generally not occur in OPVs. In OPVs bands are generally not formed but molecular orbitals carry charge carriers. For OPV operation only two main molecular orbitals are relevant, the highest occupied molecular orbital (HOMO) and the lowest unoccupied molecular orbital (LUMO).

More importantly however is charge concentration at the interface and the resulting chemical gradients. The one-dimensional current density J_n in a PV cell can be described by Equation 2.8 [57, 100]:

$$J_n(x) = n(x)\mu_n[\nabla U(x) + \mu_e(x)] \tag{2.8}$$

where n is the charge carrier density, μ_n is the charge carrier mobility, $U(x)$ is the electric potential, and μ_e is the chemical potential of the charge carrier. In essence, this equation describes the two contributing potentials for the resulting drift current and diffusion current.

Figure 2.14(b) shows how in conventional photoactive layers, the carrier generation rate of free electrons and holes decreases the deeper the light has

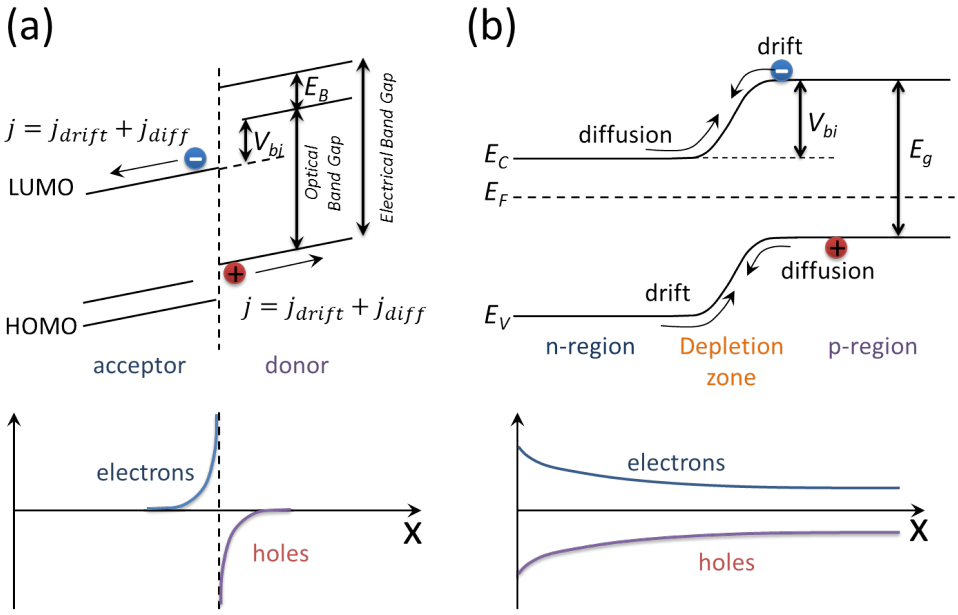

Figure 2.14. *Comparison of conventional Si PV Cell Operation to OPV Operation, adapted from [14]. (a) OPV Operation. Excitons can only be dissociated at interface between acceptor and donor. As a result, concentration gradients for holes and electrons are highest at this interface. (b) Conventional PV Cell Operation. Concentration gradients depend on light absorption and are monotonously decreasing with increasing distance into the bulk of the PV Cell.*

to penetrate the conventional p-n junction [101] and the chemical gradients of both generated charges are oriented in the same direction. Therefore, in conventional PVs, drift current is opposed to diffusion current and both reach an equilibrium for the operation of the conventional PV cell. On the other hand, in OPVs, charge carriers can only be created at the built-in potential at the heterointerface where carrier generation rates are at a maximum, as shown in Figure 2.14(a). In addition, free holes are created only in the donor layer and free electrons are only created in the acceptor layer. Due to this behaviour, chemical gradients are oriented in opposite directions. Therefore, drift and diffusion current contribute to the total current density in a OPV.

The key purpose of an OPV, i.e. its energy harvesting, can be described

by observing the exciton dissociation process more in detail. This exciton dissociation is not yet fully understood. Nevertheless, commonly a two-step model for this process is used as follows [102–105]. When considering an exciton in the donor, this exciton can either recombine to its ground state or a charge transfer reaction can occur through which free charges are generated [22]:

$$D^* + A \rightarrow D^+ + A^- \tag{2.9}$$

where D^* is the excited donor state, A is the acceptor ground state, and D^+ and A^- are hole and electron polarons in the donor and acceptor, respectively. Hence, an estimate for the maximum possible energy harvested from the OPV operation can be found [106]:

$$E_{max} \leq IP_{Donor} + EA_{acceptor} \tag{2.10}$$

where E_{max} is the maximum possible energy harvested from the OPV, IP_{Donor} is the ionization potential of a donor molecule, EA is the electron affinity of an acceptor molecule. Thus, E_{max} describes the upper limit for the open-circuit voltage of the OPV and is equivalent with the description for the built-in voltage V_{bi} in section 2.4.2. One way to optimize power generation from OPVs is to increase E_{max}, however, due to the excitonic nature of OPVs morphologies might even play a more significant role.

2.7 The Importance of Morphology Engineering

Since in OPVs free charges can only be generated at the heterointerface, then the number of excitons reaching the heterointerface should be maximized.

This however is challenging in OPVs since the exciton diffusion length is material dependent and generally about 5 to 20 nm [24, 107]. Therefore, in order to build an efficient OPV, interface engineering is required to increase the amount of free charges.

When light reaches the surface of the OPV one part of the incident light is reflected while the other part can be used for internal photocurrent generation. The external quantum efficiency (EQE) accounts for reflectivity losses [22, 54, 61]:

$$\eta_{EQE} = (1 - R)\eta_{IQE} \tag{2.11}$$

where η_{EQE} is the external quantum efficiency, R is the reflectivity, and η_{IQE} is the internal quantum efficiency which describes the efficiency for the internal photocurrent generation. This internal photocurrent generation can be defined in four subsequent steps similar to conventional PV cells, as shown in Figure 2.15: 1. light absorption (A), 2. exciton diffusion (ED), 3. exciton dissociation (E diss), and 4. charge collection (CC) [22, 61].

The internal quantum efficiency (IQE) in an OPV can be described as [22, 61]:

$$IQE = \eta_A \eta_{ED} \eta_{Ediss} \eta_{CC} \tag{2.12}$$

where η is the efficiency for the particular step in the described photocurrent generation process. Absorption and exciton diffusion in particular are limiting to OPV performance. Absorption efficiency η_A can be described as [22, 61]:

$$\eta_A = 1 - \exp(-\alpha t) \tag{2.13}$$

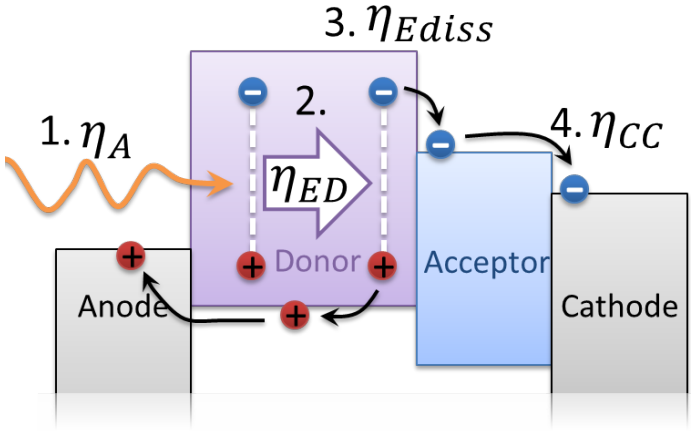

Figure 2.15. *Internal photocurrent generation in OPVs, adapted from [22]. This process can be described in 4 consecutive steps: 1. Light absorption, 2. exciton diffusion to a built-in potential such as a donor-acceptor interface 3. exciton dissociation 4. charge collection.*

where α is the absorption coefficient and t the organic film thickness. The exciton diffusion efficiency η_{ED} on the other hand, i.e. the probability for the exciton to reach a heterointerface, is [61]:

$$\eta_{ED} = \exp\left(-\frac{t}{L_D}\right) \tag{2.14}$$

where L_D is the exciton diffusion length. It becomes obvious that in a planar device efficiency would increase with higher device thickness, as in Equation 2.13. However, due to a higher photoactive layer thickness, less excitons will diffuse to the heterointerface and thus less free charges can be harvested, as shown in Equation 2.14. In planar devices therefore an optimum has to be found between both effects which limits the overall photo conversion efficiency of the planar device [108,109]. In order to overcome this device thickness limitation, morphology engineering is introduced [28,82,110–115].

Figure 2.16 shows a comparison between different OPV morphologies. In

the simplest case an OPV can be a single layer of a conjugated polymer between a transparent electrode such as indium-tin-oxide (ITO) and a reflective metal electrode such as aluminum [116], as shown in Figure 2.16(a). For this single conjugated polymer layer device, a built-in potential can be formed by a Schottky barrier at the cathode [11]. Compared to single layers, improved exciton dissociation efficiencies have been reported for donor-acceptor bilayer architectures, as shown in Figure 2.16(b), since the exciton dissociation at the heterointerface (donor-acceptor interface) is more likely to occur [54]. While significant progress has been made in optimizing this class of solar cells, the short exciton diffusion lengths limit the thickness of the photoactive layer and consequently restrict light absorption [57,61].

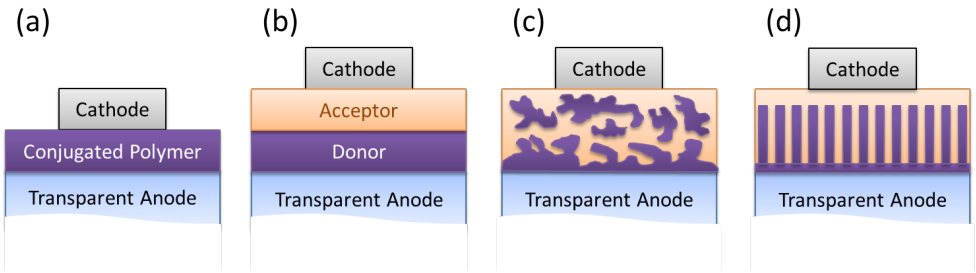

Figure 2.16. *Different OPV architectures, adapted from [11]. (a) Single conjugated polymer layer device. (b) Bilayer device in forward architecture. (c) Bulk Heterojunction with a random blend of acceptor and donor molecules in forward architecture. (d) Ordered Bulk Heterojunction in forward architecture with donor at the anode and acceptor at the cathode.*

State of the art morphology engineering uses bulk heterojunctions which can be disordered in most cases, such as in Figure 2.16(c). However, the optimal architecture is described as an ordered bulk heterojunction such as illustrated in Figure 2.16(d) [11,24,61].

2.7.1 Bulk Heterojunctions

Today, the bulk heterojunction (BHJ) is the widest researched system to achieve a high heterointerface area [7, 8, 117]. The development of bulk heterojunctions (BHJs) increased the heterointerfacial area and reduced feature sizes to approach that of exciton diffusion lengths, which has allowed for casting thicker photoactive films [117]. In contrast to a bilayer structure, BHJs are a blend or network of donor and acceptor materials. A commonly used BHJ is assembled from a two-component photoactive layer of the electron-donating, regioregular 2,5-diyl-poly(3-hexylthiophene) (P3HT) polymer and the electron-accepting [6,6]-phenyl-C_{61}-butyric acid methyl ester (PCBM) fullerene [14, 62, 118–120].

Typical BHJs exhibit a disordered morphology in the photoactive layer, resulting in pocket domains and dead ends, and thereby limit charge carrier transport [24, 108]. Therefore, achieving ordered morphologies by manipulating the network of donor and acceptor molecules on the nanoscale [28] or using self-assembly techniques [109, 121] can greatly improve device performance. An ordered architecture, as shown in Figure 2.16 based on an interpenetrating network of vertical nanocolumnar donor and acceptor materials is postulated to maximize charge transport and minimize dead-ends [11]. Several routes to fabricating those ordered bulk heterojunctions have been tried, such as: thermal gradient sublimation [122], and templated growth [27, 123].

This work focuses on building ordered bulk heterjunctions using GLAD. In terms of prior PV devices based upon GLAD, this synthetic approach has been used to fabricate vertical or slanted nanocolumns for indium tin oxide electrodes [124], dye-sensitized solar cells with titanium dioxide [125], for

hybrid TiO_2/polythiophene devices [126], and for OPV with small molecule donor materials such as copper phthalocyanine or zinc phthalocyanine [127–130].

2.7.2 Interface Layers for Better Performance

To allow for better control and consistency of injection, interfacial layers are implemented in organic electronic devices and OPVs in particular. These interfacial layers are employed between the electrodes and the photoactive layer in OPVs and are crucial for an efficient OPV operation [72, 131–136]. In this work hole transparent layer V_2O_5 and electron transparent layer Cs_2CO_3 is used [137–139].

Those interfacial layers decrease series resistance in the device leading to a higher open-circuit voltage. In addition, interfacial layers improve charge selectivity at the electrodes. When the selectivity of electrons is increased at the cathode and the selectivity of holes is higher at the anode, built-in voltage increases [21, 58, 72, 140]. This again results in a potentially higher V_{OC} and can therefore improve device performance.

2.7.3 Inverted Architecture OPVs

The architectures investigated in this work are inverted or reverse OPVs. Compared with the forward architecture, inverted OPVs use their transparent electrode as a cathode which receives photogenerated electrons. This architecture has a variety of benefits [141, 142]. Inverted OPVs can use anodes with a high work function such as gold or silver, which allows for less anode oxidation and thus lifetime, which is a major challenge in OPV design, can be increased. In addition, inverted architecture OPVs can be used for tandem

cells where a combination of a forward and inverted cell is connected in series [10,143–145]. Tandem cells have commonly the highest *PCE* out of every investigated OPV architecture.

Inverted architecture OPVs however also face major challenges. Commonly they have less PCE than their forward counterpart since electrons are injected into the ITO layer which is normally used for hole injection. In addition, acceptor design is paramount. C_{60} or $PC_{61}BM$ are so far the most commonly used acceptors since they have comparably high mobilities of up to $10^{-2} cm^2 V^{-1} s^{-1}$ [54, 88]. However, this narrow materials choice is very limiting since C_{60} and its derivatives are prone to oxidation in air which can decrease device lifetimes [146, 147]. This behaviour causes major fabrication challenges in this work, since GLAD fabricated C_{60} films can hardly be protected from air when being transported to the next fabrication step.

C_{60} is a molecule with very high symmetry which results in low polarization and therefore a low dielectric constant of 4.1 to 4.4 [148]. For the use in inverted GLAD OPVs in this work this is an additional major limiting factor. When being treated with commonly used solvents such as dichlorobenzene (DCB), chlorobenzene (CB), or chloroform, the GLAD C_{60} morphologies will immediately dissolve [29–31]. Therefore, new solvents have to be found which are compatible with processing on C_{60}.

2.8 Organic Field Effect Transistors

The research of organic field-effect transistors (OFETs) is not in direct focus of this work, however, OFETs are useful devices to determine charge mobilities in organic films [74,87,88,90,92,149–158]. We will utilize n-type OFETs for the characterization of organic acceptor materials. In particular, we will attempt

to run these devices in accumulation mode where a channel is opened by applying positive gate voltage V_{gs} and closed when the gate voltage is zero. OFET operation can be described equivalent to metal-oxide-semiconductor field-effect transistors (MOSFETs) [74]. Figure 2.17 shows operation regimes of an n-type unipolar field effect transistor in accumulation mode [73].

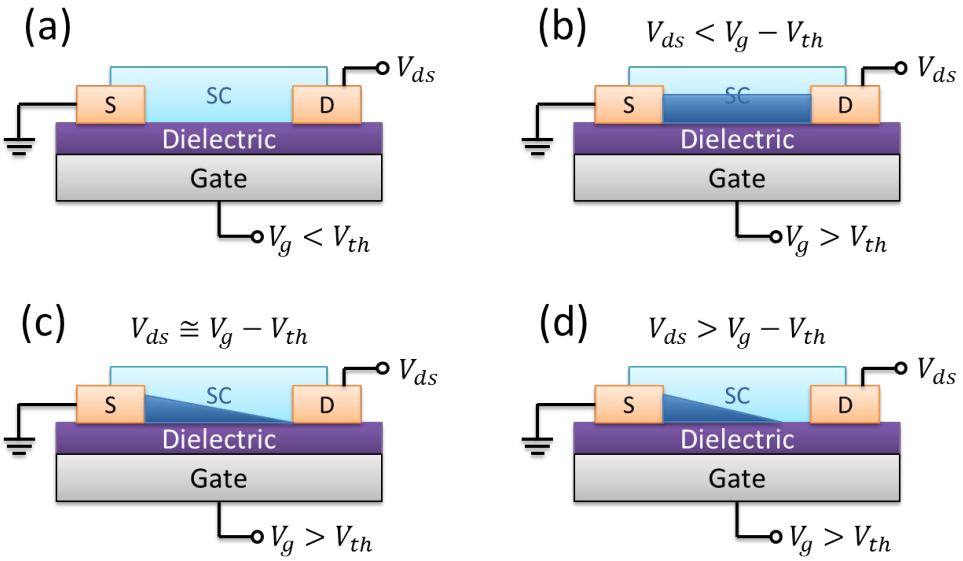

Figure 2.17. *Unipolar field-effect transistor operation. (a) Bottom-contact thin film transistor architecture with source (S), drain (D), and the semiconducting film (SC). V_{ds} is the drain voltage and V_{gs} is the gate voltage. (b) Charge accumulation at the dielectric-semiconductor interface. (c) "Pinch-off" the n-type channel. (d) Saturation regime.*

When the gate voltage V_{gs} is applied, charges accumulate at the dielectric-semiconductor interface; a positive gate voltage will attract electrons to this interface (Figure 2.17 b). The higher the capacitance of the dielectric, the more electrons will be accumulated, since

$$Q = C(V_{gs} - V_{th}) \tag{2.15}$$

where Q is the charge, C is the capacitance, V_{gs} is the gate voltage, and

V_{th} is the threshold voltage. When V_{gs} is higher than the threshold voltage V_{th}, sufficient electrons are accumulated at the interface and holes repelled in order to open a channel with electrons as majority carriers. It becomes apparent that the higher capacitance of the dielectric C the higher the charge Q. For a parallel plate geometry such as the dielectric layer described here, capacitance can be expressed as

$$C = \varepsilon_r \varepsilon_0 \frac{A}{t} \tag{2.16}$$

where ε_r is the dielectric constant, ε_0 is the electric constant, A is the surface area of a plate, and t is the dielectric thickness. Hence, more charges can be accumulated when the dielectric thickness is lowered or the dielectric constant of the dielectric increased. However, too thin a dielectric can result in leakage current through the gate electrode which can impede OFET operation.

When $V_{gs} > V_{th}$ and an additional voltage between the source and drain electrode V_{ds} is applied, a drain current I_{ds} can flow through the opened channel. Three different conductance regimes for I_{ds} can occur. Initially, with increasing V_{ds}, the drain current will increase linearly and the channel will effectively act as a resistor, as shown in Figure 2.17 c. This is the ohmic or linear regime and is drain voltage controlled. However, the increasing V_{ds} leads to a decrease of majority carriers near the drain electrode and when V_{ds} reaches $V_{gs} - V_{th}$ the channel becomes "pinched-off", i.e. the channel will be closed near the drain electrode where charges cannot accumulate anymore. For $V_{ds} > V_{gs} - V_{th}$ the drain current I_{ds} becomes saturated. In this saturation region the drain current is constant and cannot increase further, as shown in Figure 2.17 d. Figure 2.18 shows the corresponding $I_{ds} - V_{ds}$ and $I_{ds} - V_{gs}$

characteristics.

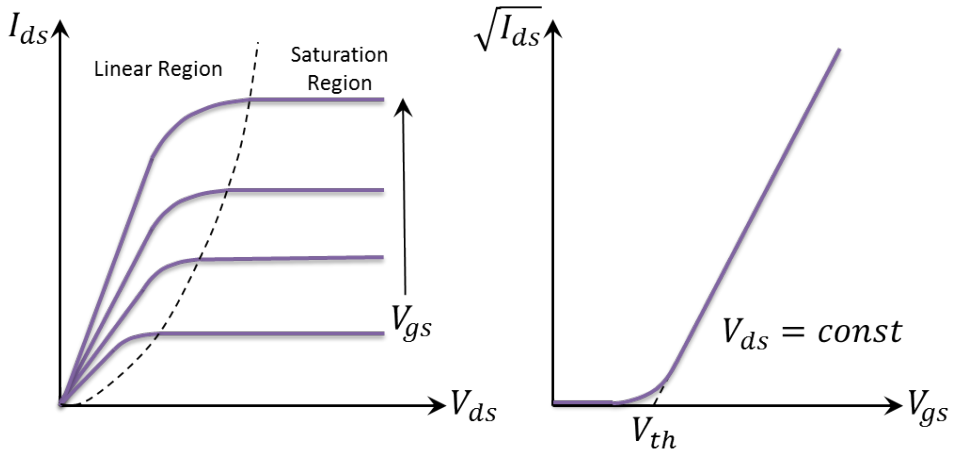

Figure 2.18. *$I - V$ characteristics for a n-type unipolar field-effect transistor. The linear or ohmic region is indicated as well as the saturation region.*

2.8.1 Modeling of OFET Operation

The purpose of OFET fabrication in this work is to determine the mobility of organic acceptors. In Figure 2.17 OFET operation is described. This operation can be modeled as follows [73]:

$$I_{ds} = \frac{W}{L}\mu C\left[(V_{gs} - V_{th})V_{ds} - \frac{V_{ds}^2}{2}\right] \tag{2.17}$$

where I_{ds} is the drain current, W is the channel width, L is the channel length, μ is the charge mobility, C is the capacitance of the dielectric, V_{gs} is the gate voltage, V_{th} is the threshold voltage and V_{ds} is the drain voltage. For the linear regime where $V_{ds} \ll (V_{gs} - V_{th})$ Equation 2.17 resolves to:

$$I_{ds-LIN} = \frac{W}{L}\mu C(V_{gs} - V_{th})V_{ds} \tag{2.18}$$

In the saturation regime however, drain bias saturates to $V_{ds-SAT} = V_{gs} -$

V_{th}, hence the drain current characteristics becomes:

$$I_{ds-SAT} = \frac{W}{2L}\mu C(V_{gs} - V_{th})^2 \tag{2.19}$$

Using these equations, the charge mobility can be estimated from a graphical solution. By drawing the drain current in its square root in the $I_{ds} - V_{gs}$ curve, such as in Figure 2.18, the curve can be fitted with a linear function. This equation can then be used to resolve to the charge mobility μ [88, 92, 159, 160].

2.8.2 Resistance in OFETs

Channel dimensions might have a strong influence on the drain current characteristics. In particular, the interplay between channel resistance and contact can be derived from channel dimensions. According to [74], the total device resistance can be described as

$$R_{tot} = R^{sheet}_{channel}\frac{L}{W} + R_{contact}\frac{1}{W} \tag{2.20}$$

where R_{tot} is the total device resistance, $R^{sheet}_{channel}$ is the sheet resistance of the channel, $R_{contact}$ is the specific contact resistance (scales with channel width) at both source and drain electrodes, L is the channel length and W is the channel width. It becomes obvious that both types of resistance are proportional to $1/W$ however only the sheet channel resistance scales with the channel length. Hence, contact resistance can play a larger role in short channel devices.

CHAPTER 3

EXPERIMENTAL METHODS[1]

The fabrication and characterization of OPVs involves methods from a broad variety of scientific disciplines. For this work a high emphasis is put on organic film deposition. In addition, the films and various architectures thereof are investigated with a variety of structural, optical and electronic methods. For some architectures, devices were fabricated and their performances analyzed and compared.

3.1 Glancing Angle Deposition Apparatus

Essential for a GLAD apparatus is the substrate movement control. The substrate holder uses two motors to manipulate the deposition angle α and substrate rotation ϕ (as shown in Figure 3.1. Since film morphology can depend on substrate rotation at specific deposition rates, i.e. the pitch [45], the rotation speed of the substrate is calibrated with the deposition rate of the material. The substrate motion can be controlled by a computer program which

[1] Parts are reproduced with permission from [29]. Copyright 2011 American Chemical Society. — ©2011 IEEE. Reprinted, with permission, from [31]. — Reprinted from Organic Electronics [30], Copyright (2012), with permission from Elsevier.

allows for programming of a motion script in order to achieve a particular growth morphology. Particle flux is generated from thermal evaporation off a crucible source. The source is positioned farther away from the substrate than usual in order to generate a quasi-collimated particle flux to the substrate. In addition, this reduces heat radiation to the substrate allowing for particle condensation as well as a lower surface diffusion which is essential to GLAD growth.

Additional components which are used for process control are generally used for thin film deposition and are not specific to GLAD. A quartz crystal microbalance (QCM) allows to monitor for the deposited film thickness. The deposition is performed in ultra-high vacuum.

3.1.1 Deposition Ratio

During deposition, the actual film thickness of the substrate is influence by various factors such as chamber pressure, substrate temperature, sticking coefficients and others. Since all of these parameters are held constant the most important parameter for actual film thickness is the substrate angle. As explained in chapter 2 film thickness decreases with a growing deposition angle α. In order to reach a specific film thickness defining a deposition ratio (R_{dep}) is useful.

$$R_{dep}(\alpha) = \frac{t_(\alpha)}{t_{QCM}(\alpha)} \tag{3.1}$$

This is a simple ratio of measured film thickness on the QCM during deposition vs. actual film thickness. This deposition ratio is shown in Equation 3.1 where t is the final film thickness as determined by scanning electron microscopy and t_{QCM} is the measured thickness during processing.

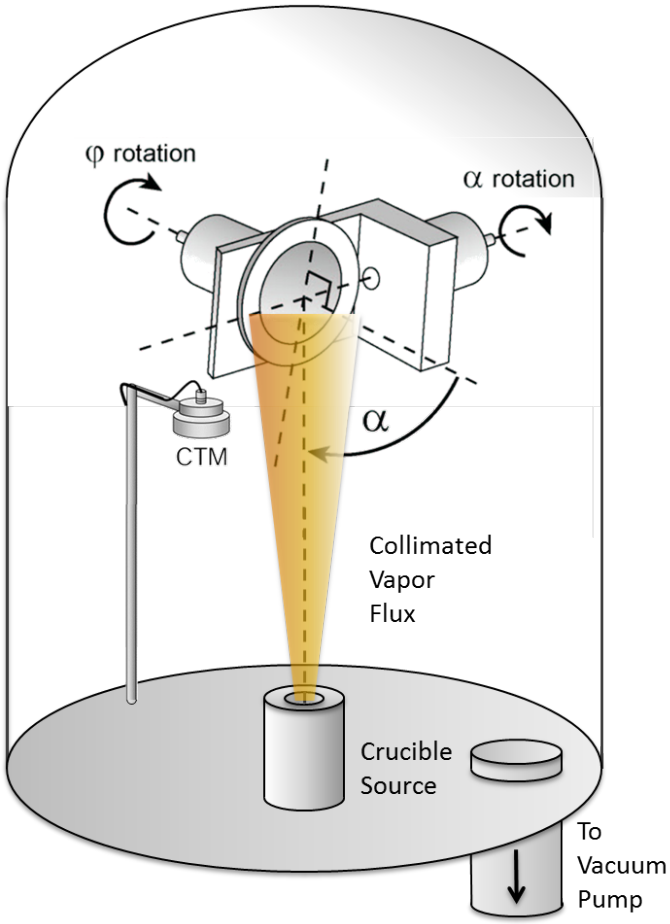

Figure 3.1. *GLAD Apparatus. Two computer-controlled motors allow for substrate movement in α and ϕ. A calibrated crystal thickness monitor (CTM) or quartz crystal micro balance measure deposited film thickness. Particle flux is generated from a Al_2O_3 crucible source through thermal evaporation. A large distance from substrate allows for a collimated vapor flux. Ultra-high vacuum is provided by a connected oil-diffusion pump.*

3.2 Evaporation of Organic Films

Compared with inorganic materials particular care needs to be taken for the deposition of organic materials. In this work C_{60} and PTCDA films are GLAD-structured. Both materials are sensitive to impurities, in particular C_{60} [147]. The most common impurities are oxygen and water. Therefore,

before fabricating devices, the material is left overnight at a temperature below evaporation, normally 250 $^{\circ}C$, at a pressure of 1×10^{-7} *Torr* in order to purify the material in the crucible.

C_{60} powder (Sigma-Aldrich, 99.9 % pure) was evaporated on various substrates depending on the application. However, if not specified differently, then C_{60} is deposited on ITO coated glass substrates (Delta Technologies, thickness $\sim$ 130 *nm*, sheet resistance $\sim$ 20 Ωsq^{-1}). Thermal evaporation was performed from an alumina crucible (Delta Glass) at an evaporation temperature of about 450 $^{\circ}C$ and a working pressure of 2×10^{-7} *Torr*. Deposition rates between 0.5 Ås^{-1} to 2 Ås^{-1} were achieved. During evaporation, substrate rotation was applied to achieve a more homogenous film thickness distribution. Rotation speeds ranging from 0.2 *rpm* to 0.6 *rpm* were used to maintain a constant pitch of 24 *nm*, i.e. a full substrate turn per 24 *nm* of film growth.

For perylene-3,4,9,10-tetracarboxylic dianhydride (PTCDA), evaporation powder purchased from Sigma-Aldrich (purity 97 %) was evaporated at about 350 $^{\circ}C$ from an alumina crucible (Delta Glass). If not explained otherwise, on glass/ITO substrates as outlined above. Before evaporation, the material was purified at 200 $^{\circ}C$ overnight in the deposition chamber at a pressure of 1×10^{-7} *Torr*. Deposition rates ranged from 0.5 Ås^{-1} to 3 Ås^{-1}.

3.3 Top Electrodes and Interface Layers

When fabricating OPVs, interface layers need to be employed. As explained in section 2.7.2, interface layers improve V_{OC} in OPVs by increasing the built-in voltage of the device through improved selection of electrons at the cathode and holes at the anode as well as improved charge injection at the elec-

trodes. As an interface modifier for the cathode we used Cs_2CO_3 which is known to significantly improve device performance [139]. For the interface layer at the anode V_2O_5 is employed [136].

For the Cs_2CO_3 layer, the ITO coated glass substrates were prepared by sequential sonication in methylene chloride, millipore water (18 $M\Omega\, cm$), and 2-propanol (isopropanol, IPA) for 10 min each. Next, the substrates were plasma cleaned for 10 min in an air plasma using a Harrick plasma (PDC 32G, 18 W) cleaner at $\sim$ 0.1 $mTorr$ working pressure. The Cs_2CO_3 layer was cast from a 0.2 $wt\%$ solution in 2-ethoxyethanol and annealed at 150 $^{\circ}C$ for 20 min [139]. The V_2O_5 interface layer ($\sim$ 5 nm) was thermally evaporated before deposition of Al as the top-electrode ($\sim$ 200 nm).

3.4 Device Fabrication

3.4.1 Polymer Device Fabrication

ITO coated glass substrates were sequentially sonicated in methylene chloride, Millipore water (18 $M\Omega cm$) and 2-propanol for 10 min each. A 10 min air plasma was then performed with a Harrick plasma (PDC 32G, 18 W) cleaner at $\sim$ 0.1 $mTorr$. Cs_2CO_3 was used as a cathodic interfacial modifier and was cast from a 0.2 $wt\%$ solution in 2-ethoxyethanol forming a $\sim$ 1 nm thick layer. The substrate was then annealed at 150 $^{\circ}C$ for 20 min as previously reported [139]. The substrates were then placed into the GLAD vacuum chamber for deposition of C_{60} films. After the C_{60} deposition, substrates were removed from the chamber under Ar flow and transferred to a desiccator purged with argon to limit the air exposure of the C_{60} films and oxidation of the surface. C_{60} films were immediately ($\sim$ 10 min) transferred to a nitrogen filled glove box. P3HT and P3CBT (30 $mg\, mL^{-1}$) in o-dichlorobenzene

and dimethyl sulfoxide (DMSO) respectively were filtered with a 0.2 μm PTFE filter and spun-on directly onto the C_{60} films at 600 rpm for 10 min. Films were then annealed at 50 $^{\circ}C$ for 20 min. V_2O_5 (20 nm) and Al (70 nm to 80 nm) were deposited by thermal evaporation at a rate of 0.01 $Å s^{-1}$ and 5 $Å s^{-1}$ respectively. Devices are fabricated in sets of 5 per substrate, with a $(0.155 \pm 0.008)\ cm^2$ device area. For each deposition angle, multiple devices were fabricated and characterized. The average and standard deviation values are measured from at least 10 separate devices fabricated in one process. V_2O_5 and Al deposition was performed by Tate Hauger.

3.4.2 Small Molecule Device Fabrication

5 $mg\, ml^{-1}$ of 3-Q were dissolved in acetone (HPLC, Sigma-Aldrich) and in order to improve dissolution the mixture was kept in an ultrasonic bath for about one hour. The resulting solution was spun directly onto the C_{60} films at 400 rpm for 1 min in air. During this process the pipettes and solution were kept at 50 $^{\circ}C$ in order to maintain solubility of the 3-Q. For anode fabrication, V_2O_5 ($\sim$ 20 nm) and Al ($\sim$ 120 nm) were thermally evaporated at a rate of 0.01 and 5 $Å\, s^{-1}$, respectively. 5 devices per substrate with a $(0.155 \pm 0.008)\ cm^2$ device area were made. For each deposition angle, multiple devices were fabricated and characterized. The average and standard deviation values are measured from at least 10 separate devices fabricated in one process. For comparison, bulk heterojunctions of 3-Q and $PC_{61}BM$ ([6,6]-phenyl-C_{61}-butyric-acid-methyl-ester) were fabricated as described in [161] with an active layer thickness of 70 nm. The spin coating of 3-Q was performed by Dr. Weiwei Li; V_2O_5 and Al deposition was performed by Tate Hauger.

3.5 Organic Field Effect Transistor Microfabrication

This work is not focused on transistors. However, transistors are useful devices in order to measure mobility of our acceptor films. Although OFETs can be fabricated in various architectures [74], bottom-contact OFETs are fabricated for this thesis [154–157].

3.5.1 Mask Design

Patterning is essential for OFET fabrication for which photolithography is employed. Contrary to inorganic thin film transistors, the organic transistors use much larger feature sizes due to the intrisically low mobility in organic semiconductors compared with inorganics . For patterning photolithography is used and the photomask design is illustrated in Figure 3.2. Each 4 *inch* wafer will carry up to 12 chips of 2×2 *mm* OFET arrays with different channel sizes. Commonly used channel widths are in the *mm* range and commonly used channel lengths are in the μm range. The bottom electrode array covers those standard channel sizes as well as some more unusual geometries with very high aspect ratios in order to allow for measuring the influence of the channel size.

As electrode material Au is chosen which has a low adhesion on the oxidized silicon wafer surface. Previous attempts to fabricate Au electrodes using a lift-off process resulted in patterning errors. Therefore, this photomask is designed for a positive photoresist in order to directly etch the metal electrodes and avoid lift-off procedures.

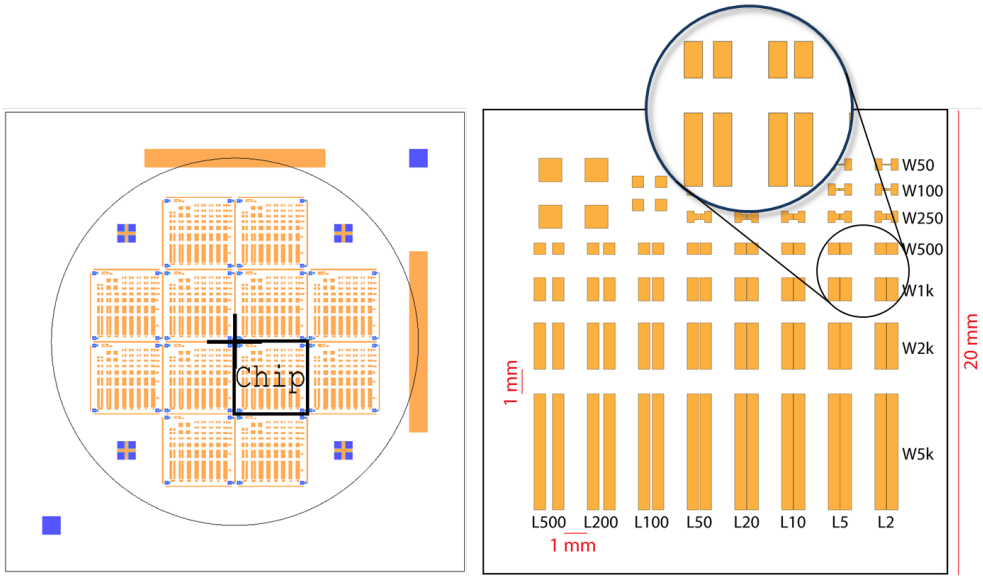

Figure 3.2. *OFET Array Mask Design. A 4-inch wafer fits 12 chips of* 20×20 *mm size. The array contains a combination of OFETs with a channel length from* 2 μm *to* 500 μm *and channel widths of* 50 μm *to* 5000 μm

3.5.2 Process Flow

A flow chart for the entire OFET fabrication process is shown in Figure 3.3. Except of the metal deposition, all of the steps are performed in a class 100 cleanroom. The process starts with a heavily n-doped silicon 4 *inch* wafer (resistivity $0.001 - 0.005\ \Omega cm$).

Before oxidation, wafers are cleaned in a hot Piranha solution for 15 *min*. Thermal oxidation is performed in a Minibrute furnace at 950 °. Oxide thickness is controlled by oxidation time. Oxidation time is calibrated by measuring oxide thickness after oxidation and comparing with time oxidized. Next, gold and chrome for the top electrodes are deposited in a Kurt Lesker sputtering system. Unless described otherwise, total metal electrode thickness is 50 *nm* and about 2 *nm* of chrome are used as an adhesion layer. The entire wafer is then patterned through photolithography with HPR 504 as photore-

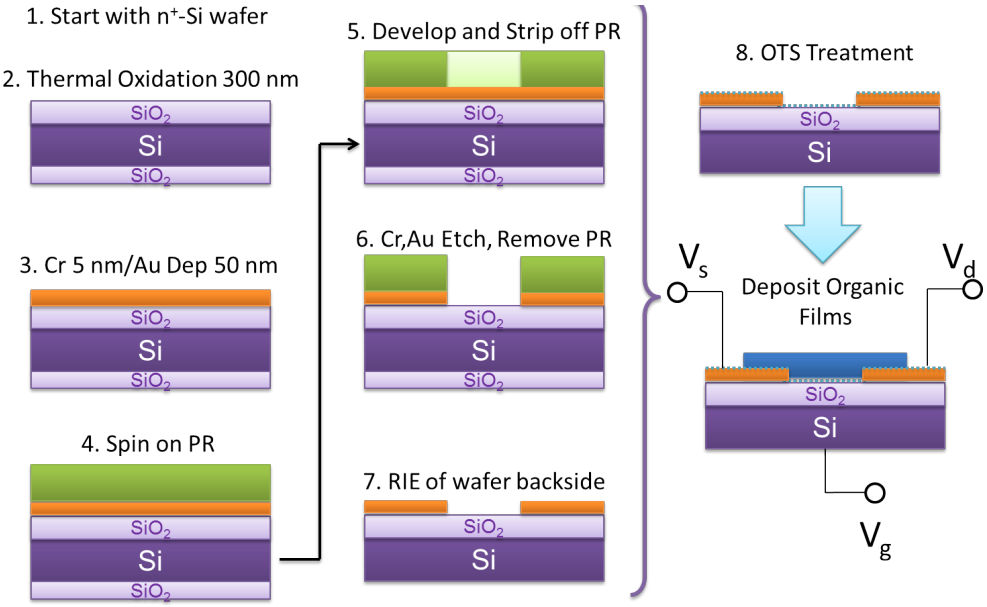

Figure 3.3. *OFET Microfabrication Unit Process Flow. The final OFET template is surface treated with n-octadecyltrichlorosilane (OTS) before depositing organic semiconducting films.*

sist and 354 developer. The electrodes are then subsequently etched with gold and chrome etch respectively. The photoresist is stripped by soaking the wafers in acetone for 15 *min* and subsequently rinsing in isopropanol. Lastly, in order to provide a better contact for the gate electrode, the bottom oxide is removed by putting the wafers upside down in a STS reactive ion etch (RIE). The lip seal of the RIE allows for the top side of the wafer to be unharmed by the etching plasma. The resulting wafer is simply cleaved; by properly aligning the wafer during patterning cleaving is possible with sufficient accuracy along the dicing lines. Each chip is a completed OFET electrode template and then used for further fabrication of various devices.

The quality of the interface between dielectric and the organic film is essential for the gate effect. Therefore, before an organic film deposition the OFET templates are coated with a self-assembled monolayer (SAM) such as

n-octadecyltrichlorosilane (OTS) [162]. For preparing an OTS SAM, the chips are cleaned in an ultrasonic bath of acetone and isopropanol for 10 *min* each followed by an 10 *min* oxygen plasma treatment in a Harrick plasma (PDC 32G, 18 W) cleaner at ~ 0.1 *mTorr*. The cleaned OFET templates were put in a vacuum oven together with an open vile of OTS (90%+ purity). The oven was pumped down to a pressure of -25 *mm* of water when the vacuum valve was closed off. The OFET templates were left in an OTS vapor atmosphere for more than 10 *h* at a temperature of $120^{\circ}C$. After this treatment the oven is vented with air and the OFET templates are taken out without waiting for the oven to cool down. After this OTS vapor treatment, multilayers of OTS may have been deposited instead of a required monolayer. In order to remove the multilayers, the OFET templates are treated with IPA in an ultrasonic bath for 10 *min* right before putting these substrates into the process chamber for the deposition of the active OFET layer.

3.6 Sample Characterization

3.6.1 Film Morphology

Throughout this work, film morphology was analyzed using scanning electron microscopy (SEM) in secondary electron mode. A Hitachi S-4800 field emission gun secondary electron microscope (SEM) and JEOL JSM-6301 FXV SEM is used. For cross-section images, films were cleaved after cooling in liquid nitrogen and during microscopy the stage was tilted by 3° in order to improve image sharpness and avoid artefacts. Unless otherwise described, organic GLAD film thicknesses are measured with the SEM and range from 80 *nm* to 120 *nm* for the GLAD C_{60} films as well as the GLAD PTCDA films. The images were analyzed using Adobe Photoshop CS 4 to determine aver-

age column spacings and diameters. Measurements on the JEOL JSM-6301 FXV SEM were performed by George Braybrook.

3.6.2 Polymer Filling Analysis

In order to investigate the polymer filling into the GLAD structure, the multilayers of C_{60}/P3CBT deposited on ITO/glass were embedded in Spurr's epoxy resin [163] and cured at $70°C$ for $8\ h$. The product was dipped sequentially in liquid nitrogen and water to crack the film from the glass. The resulting supported film was microtomed with a diamond blade. The cross-sections were floated onto carbon coated transmission electron microscope (TEM) grids and viewed with a JEOL JEM 2100 TEM with an accelerating voltage of $120\ kV$. This sample preparation and measurement was performed by Brian J. Worfolk.

3.6.3 Crystal Structure

The crystal structure of the films deposited on ITO/glass was investigated using Bragg-Brentano X-ray diffractometry (XRD) with a Bruker D8 Discover with GADDS using Cu-K_α ($\lambda = 1.541$ Å) radiation. Since films were thin, the XRD was performed at a grazing incidence angle of $\omega = 1°$. When measuring full-width-at-half-maximum, average instrumental aperture of $0.31°$ was accounted for as a systematic error.

3.6.4 Ultraviolet Photoelectron Spectroscopy

In order to measure the electron level configurations of PTCDA:C_{60} ultraviolet photoelectron spectroscopy (UPS) is applied. For this characterization, a Kratos Ultra spectrometer with He I ($h\nu = 21.2\ eV$) incident radiation is

used. During the measurement of the PTCDA:C_{60} on ITO the substrates were biased at $-10\ V$. The measurements and the analysis of the results were performed together with Brian J. Worfolk and Dr. Dimitre Karpuzov.

3.6.5 Xray Photoelectron Spectroscopy

For the content estimate of both components in PTCDA:C_{60} blends Xray photolectron spectroscopy (XPS) on the sample surfaces is used. This XPS was performed in a Kratos Ultra spectrometer with a monochromatic Al K_α ($h\nu = 1486.71\ eV$) radiation source. The spectra are referenced to the Fermi level and corrected to the C(1s) peak at 284.8 eV. In addition, the spectra are referenced to the binding energy of Au $4f7/2$ of 84.0 eV. The measurement is performed under vacuum in base pressure of less than 5×10^{10} *Torr* before radiation. In order to estimate PTCDA content, $C = O$ peaks have been analyzed in particular, since $C = O$ bonds are present in PTCDA while no $C = O$ bonds exist in C_{60}. The measurements and the analysis of the results were performed by Brian J. Worfolk and Dr. Dimitre Karpuzov.

3.6.6 Optical Measurements

Absorbance and Extinction

Absorbance measurements of C_{60} films, PTCDA only, or multilayered films were performed with a spectrophotometer (Perkin-Elmer NIR-UV Lambda 900). For all of the optical measurements the organic films were deposited on fused silica substrates. For calibration, baselines for a blocked beam and open beam through a pure silica substrate were taken before each measurement series. Absorbance measurements were performed using the "absorbance" mode of the spectrophotometer. However, since the spectrophotometer does

not account for reflection, scattering and losses from interference effects, it actually measures extinction. Those extinction measurements are in close approximation to absorbance as losses are relatively small. Therefore, for simple optical studies, extinction is often replaced with the term absorbance or absorption in the OPV literature. Hence, for qualitative studies in this thesis, such as estimations of peak positions, we will use the term absorbance as well.

For quantitative measurements, however, extinction coefficients are calculated from transmittance spectra instead of measuring with the spectrophotometer's absorbance mode. These extinction coefficients α were determined by using Equation 3.2 which is resolved to 3.3, where I_0 is the intensity of the beam going through a pure silica substrate, I is the intensity of the beam going through the sample, t the total thickness of the organic film or multilayer, and λ is the wavelength. The measurement approach and the analysis results were in parts discussed together with Dr. Michael T. Taschuk.

$$I = I_0 \exp(-\alpha(\lambda)t) \tag{3.2}$$

$$\alpha(\lambda) = \frac{1}{t}\left(\ln\frac{I_0}{I}\right) \tag{3.3}$$

Exciton Quenching

Photoluminescence was measured for the P3CBT-only, GLAD C_{60}-only and C_{60}/P3CBT multilayer films on fused silica substrates using a 442 *nm* He-Cd laser as the excitation source. Scattered 442 *nm* light was filtered with a long pass filter (475 *nm*, Thorlabs, Inc.). The remaining photoluminescence was measured with a compact CCD spectrometer (Ocean Optics USB2000, 300 *nm*

to 1050 *nm*). The spectral responsivity of the compact CCD spectrometer was corrected using a black body source (HL-2000-FHSA-LL). Integration time was 500 *ms* for all measurements, and a dark spectrum was subtracted in each case. To account for differences in film thickness and absorbance, the P3CBT-only absorbance spectrum was normalized to the spectrum of the P3CBT in the multilayered samples. The PL measurement was performed together with Brian J. Worfolk.

3.7 Electronic Measurements

3.7.1 Solar Simulator Measurement Setup

$J - V$ characteristics were measured using an Oriel 91191 1000 W solar simulator together with a Keithley 2400 source meter. Light intensity was calibrated using a Si solar cell standard (NREL certified) together using a KG-5 filter (PV Measurements Inc., PVM624). The solar simulator measurement setup has initially been a collective effort by our group, however, I would like to give credit to Tate Hauger in particular for the realization of the designs and the maintenance of the measurement setup as well as for performing the $J - V$ measurements.

3.7.2 Results Statistics of Standard Architecture

Since this work is focusing of the effects of morphology on the change in device performance, a consistent set of results is essential. In the field of organic photovoltaics results can vary due to the short lifetime of the organic films. While most publications on organic photovoltaic cells seem to neglect variance in measurement statistics, an example of performance value distributions is given here for illustration, as shown in Figure 3.4.

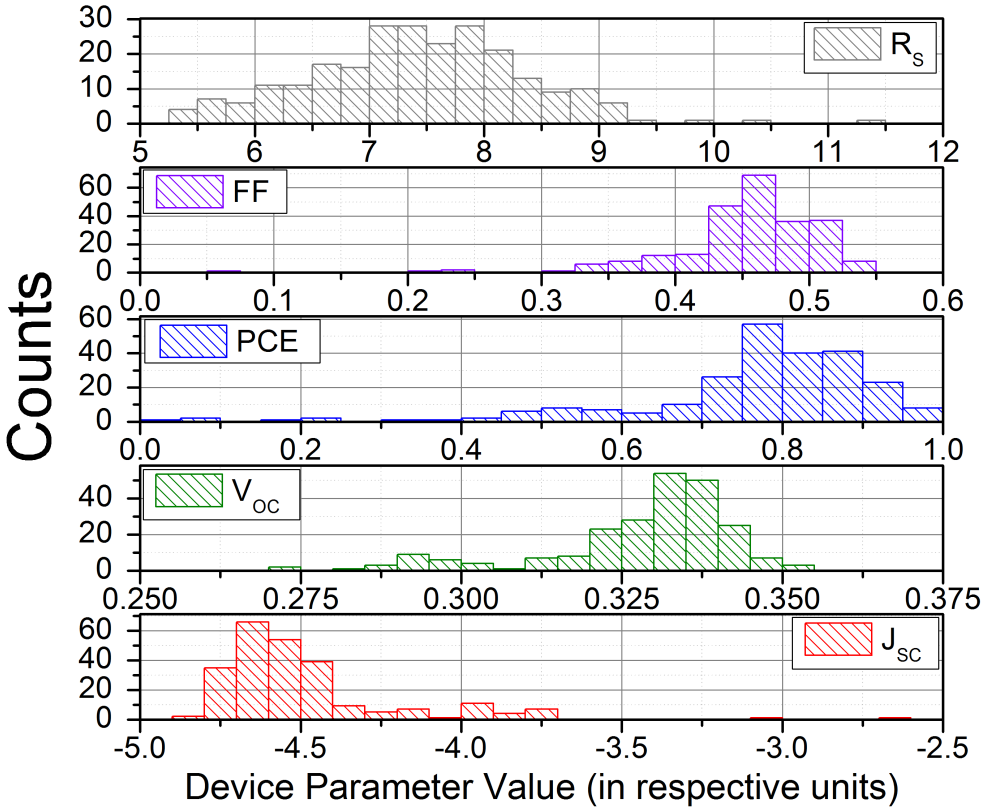

Figure 3.4. *Commonly measured device performance distributions for a GLAD-structured OPV of C_{60}/P3CBT made at $\alpha = 75\ ^{\circ}$. The x-axis describes the performance values for each parameter in respective units, i.e. Ω for the series resistance R_S, % for the power conversion efficiency PCE, V for the open-circuit voltage V_{OC}, $mA\ cm^{-2}$ for the short-circuit current J_{SC}, and fill factor FF are shown.*

It becomes obvious that variance can be quite large with the fabrication process used to fabricate our devices. In particular, the unavoidable exposure of the GLAD structured C_{60} surface to air can be a major cause for performance fluctuations. Nevertheless, strong care was taken to collect a large enough number of measurements to allow for statistically significant results.

3.7.3 Transistor Measurements

Characteristic curves such as $I_{ds} - V_{ds}$ or $I_{ds} - V_{gs}$ were measured in a Keithley 4200 probe station and the measurement setup is illustrated in Figure 3.5.

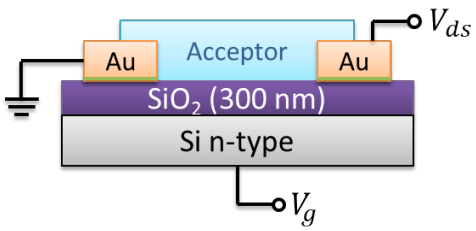

Figure 3.5. *The fabricated OFET architecture with* 50 *nm thick polycrystalline Au electrodes deposited on a* 300 *nm thick* SiO_2 *layer which acts as dielectric. For adhesion,* 2 *nm of Cr were used between the* SiO_2 *and the Au electrodes. For the characterization of the acceptors planar films are used. Gate voltage was applied from the bottom of the Si wafer. Drain voltage was applied at the source electrode. The drain electrode was connected to the ground and acts as common electrode for gate and drain voltage.*

The bottom gate electrode was connected through a copper coated glass slide. The top electrodes were connected with the probes punching through the organic film directly onto the source and drain electrodes. Wiping with isopropanol of the top electrodes was tried before connecting with the probes, however, performance did not improve. For an ideal device fabrication a shadow mask should be used to properly align the transistor film with the top electrodes. All drain current characteristics were measured in the dark. I would like to thank Ben Bathgate and Kyle Bothe for troubleshooting and discussion of the measurements.

CHAPTER 4

MORPHOLOGIES FOR INVERTED ORGANIC PHOTOVOLTAIC CELLS[1]

Before building OPVs, this chapter describes the fabrication and characterization of GLAD structured C_{60} films. Polycrystalline and epitaxial C_{60} films have been deposited on single crystalline substrates such as sodium chloride, gallium arsenide, or mica [164–167]. In this chapter we investigate a stronger degree of morphology control using advanced motion algorithms.

4.1 Control of Column Spacing

A central hypothesis to this work is that OPV performance can be improved by employing an ordered bulk heterojunction architecture. In particular, the inverted architecture OPV would require control of the column spacing of the acceptor material, as shown in Figure 4.1. As described in chapter 2.7, the domain size features of an organic photovoltaic cell would ideally be in the order of the exciton diffusion length of the absorbing material [11,24,54].

[1]Parts are reproduced with permission from [29]. Copyright 2011 American Chemical Society. and ©2011 IEEE. Reprinted, with permission, from [31].

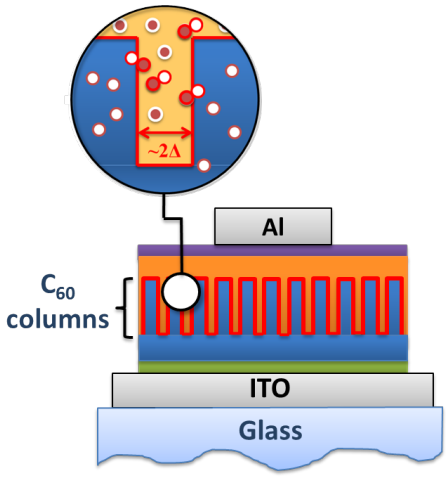

Figure 4.1. *An inverted OPV architecture based on GLAD structured C_{60} films. The magnifying circle illustrates the distribution of excitons in-between C_{60} columns. Δ symbolizes the exciton diffusion length in the donor material filled into the C_{60} columns.*

To investigate the scope of C_{60} film morphology obtainable via GLAD, tilted and vertical C_{60} nanocolumns were fabricated on ITO-coated glass at deposition angles (α) of 75, 80, and 85°, with and without sample rotation. Figure 4.2 shows SEM images with top and side views of the nanostructured films. Films deposited at an angle α of 80° (Figure 4.2a) have a thickness of (210 ± 30) nm and an average column tilt angle (β, measured from substrate normal) of $(60 \pm 5)°$. This value agrees with the prediction from Tait's ballistic model [50] of $\beta = 56°$. The average midheight column diameter is (60 ± 10) nm and the average column length is (350 ± 50) nm.

During the GLAD deposition process, substrate rotation concurrent with deposition creates an isotropic distribution of flux over initial nuclei that form on the surface, resulting in vertically oriented columns. The SEM images of C_{60} films, shown in Figure 4.2 b,d, show vertical C_{60} nanocolumns that were deposited with rotation, at angles of 75, 80, and 85°. Average column diameter and intercolumn spacing are given in Table 4.1.

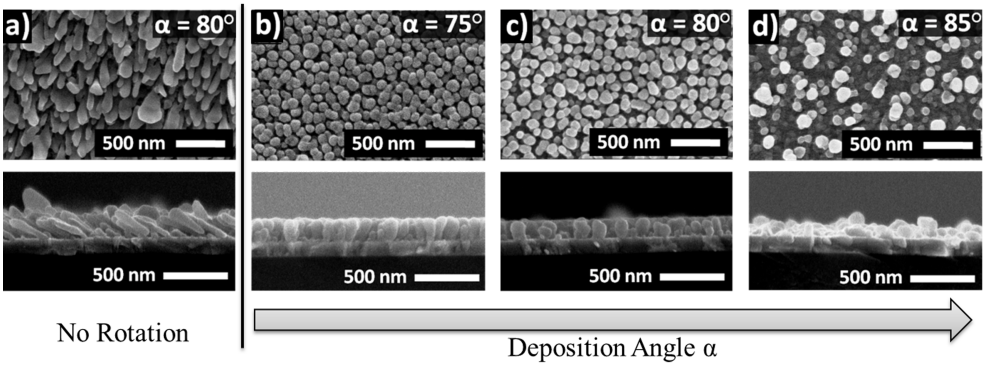

Figure 4.2. *(a) Top and side views of a C_{60} film deposited by GLAD at α = 80° with no substrate rotation. The growth results in slanted columns tilted by $\beta = (60 \pm 5)^\circ$ from the normal vector of the substrate. (b to d) Vertical columnar C_{60} GLAD films deposited with continuous rotation at α = 75, 80, and 85°, respectively. SEM images were taken by George Braybrook. Reproduced with permission from [29]. Copyright 2011 American Chemical Society.*

Table 4.1. *Column spacing and column diameters of GLAD C_{60} thin film morphologies as measured with the SEM. Reproduced with permission from [29]. Copyright 2011 American Chemical Society.*

Morphology	Deposition Angle (deg)	Col. Spacing (nm)	Col. Diameter (nm)
tilted columns	80	50 ± 10	60 ± 10
vertical columns	75	40 ± 20	90 ± 10
vertical columns	80	65 ± 20	90 ± 10
vertical columns	85	180 ± 90	100 ± 20

For C_{60} vertical posts deposited between 75 and 85°, column diameter does not depend strongly on deposition angle, however the average intercolumn spacing is (40 ± 20) *nm* and $65 \pm 20)$ *nm* for films deposited at angles of 75 and 80°, respectively. Intercolumn spacing increases nonlinearly, however, to (180 ± 90) *nm* at a deposition angle of 85°, in agreement with ballistic simulations [50]. At higher deposition angles (α = 85°) of C_{60}, GLAD post heights become less uniform, increasing the relative thickness of the nanocolumn/air interface, an effect previously observed for inorganic GLAD films [45, 168]. As is well known for GLAD films, the C_{60} film density is inversely proportional to deposition angle with higher densities at lower deposition angles of

α, following Tait's ballistic approximation for normalized film density [26]. Optical absorbance measurements reveal the effect of varying film density (as shown in Figure 4.3).

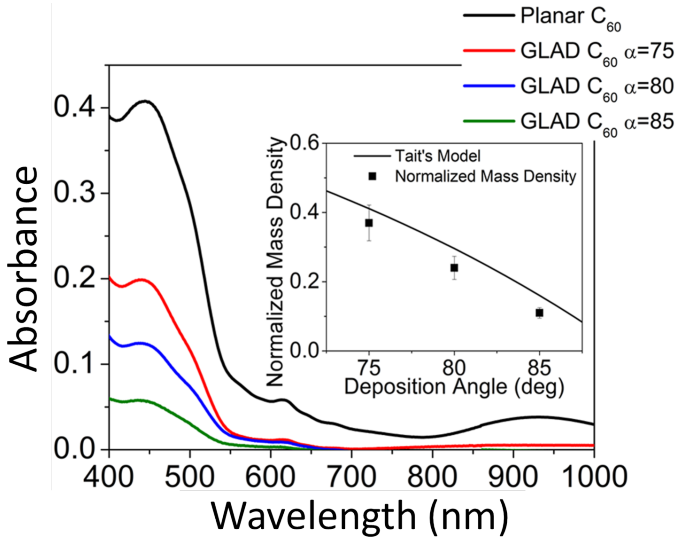

Figure 4.3. *Absorbance measurements of C_{60} films prepared by GLAD at different deposition angles (α). Spectra are normalized to film thickness. The inset shows the normalized mass density as derived from the given absorbance measurements. The dashed curve shows Tait's approximation for the normalized film density (normalized to a film deposited at normal incidence angle). Reproduced with permission from [29]. Copyright 2011 American Chemical Society.*

As deposition angle α increases, the density of deposited material and corresponding absorbance decreases. As this ensemble of results shows, through control of substrate orientation during deposition, the GLAD technique enables the deposition of C_{60} nanocolumns with tunable structures. In excitonic photovoltaic cells, the exciton diffusion length can be a limiting factor, as stated earlier [57, 99]. One optimization route for a given organic PV material system is to increase surface area while reducing exciton diffusion paths. For GLAD, this route corresponds to increasing film thickness while matching intercolumn spacing to the exciton diffusion length, by con-

trolling the deposition angle. The carboxylic acid-functionalized polythiophene polymer, P3CBT (Figure 5.1c, p. 70), has an expected exciton diffusion length of 5 to 20 *nm* [11, 15, 18, 169]. Of the deposition angles studied here, 75° provides the architecture best matched to the diffusion length. While in principle it would be possible to further reduce intercolumn spacing, this demand must be balanced by the ease of infiltration of the P3CBT into the GLAD nanostructure; these characteristics are discussed below.

4.2 Crystal Structure of GLAD C_{60} Films

Previous studies of planar C_{60} [164, 165, 170] and nanostructured C_{60} columnar films [171] have shown them to be polycrystalline. Figure 4.4 shows XRD results for the GLAD-deposited C_{60} films deposited on ITO electrodes. All three films exhibit a polycrystalline structure with crystallites predominantly oriented in {111} and {220} planes. The d-spacings of the films are observed at 8 Å and 5 Å for the {111} and {220} planes, respectively. Other C_{60} peaks have not been observed.

Together with the Miller indices selection rules, these results indicate a face-centered cubic structure with a resulting lattice constant of 14 Å. These findings are in agreement with previously reported C_{60} results which describe polycrystalline films with a lattice constant of 14.224 Å for an f.c.c. structure [172]. Crystallite sizes were determined using the Scherrer equation [173] for spherical crystallites and are given in Table 4.2. The crystallites appear to be somewhat larger in the nanostructured GLAD C_{60} films as compared to the planar films ($\alpha = 0°$). In the planar C_{60} film, both the {111} and {220} planes have comparable intensities, but it can be noted that the {111} plane has a slightly higher intensity in the planar film, whereas in the colum-

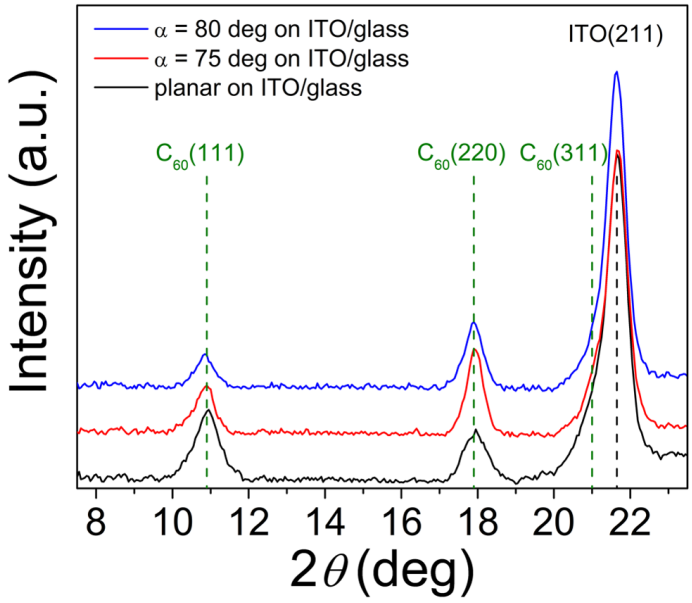

Figure 4.4. *X-ray diffraction measurement of a planar and nanostructured C_{60} film on an ITO/glass substrate with linear intensity. The top two measurements (vertical order in legend follows vertical sequence of measurements) show the diffraction pattern for a film deposited at $\alpha = 80°$ and $\alpha = 75°$, respectively. The bottom measurement (black) represents the planar C_{60} film. Dotted vertical lines mark the peak positions for the crystallographic orientations in each material. Reproduced with permission from [29]. Copyright 2011 American Chemical Society.*

nar film, the {220} orientation is stronger. These results suggest that during GLAD deposition, {220} oriented crystallites are more favorably grown than {111} oriented crystal planes. Similar preferential growth has been previously observed in nanocolumns formed by GLAD [174].

Table 4.2. *Summary of crystallite sizes measured for the {111} phase and {220} phase in the planar and GLAD-structured C_{60} films. Reproduced with permission from [29]. Copyright 2011 American Chemical Society.*

Deposition Angle(°)	**Crystallite Size (nm)**	
	{111} phase	{220} phase
0	20	22
75	30	43
80	33	34

4.3 Advanced Motion Algorithm: ϕ-Sweep

For the use in OPVs the surface area of the GLAD C_{60} films is relevant. One approach to alter the diameters of the columns in order to achieve a higher surface area is the ϕ-sweep method (as shown in section 2.3.1). For ϕ-sweep, instead of applying a constant substrate rotation speed in ϕ during deposition, the substrate is rocked with the angular amplitude γ instead. Due to this motion, anisotropic shadowing between columns is minimized and thus column diameters can be reduced [45, 53].

Three films with amplitudes of γ = 30°, 60° and 90°, respectively, were fabricated at a constant substrate angle of $\alpha = 80°$, as shown in Figure 4.5. As γ increases, column tilt angle decreases towards the substrate normal. Neighboring columns coalesce in a direction aligned with the axis of anisotropic shadowing. Anisotropic shadowing increases with higher sweep angles γ causing more coalescence at higher angles. Equivalently, the column cross-section becomes more ellipsoidal with its short half-axis aligned with the central axis. The average short half-axis is about 50 ± 5 nm thick; about half the average column diameters of the vertical columns generated with continuous rotation. For phi-sweep deposition the angular amplitude γ is an additional parameter influencing column tilt β [45, 53]. The C_{60} film behavior is consistent with that rule (as shown in Figure 4.5 d).

Table 4.3 summarizes the morphology of phi-sweep grown films. Due to anisotropic shadowing the cross-sections of columns deposited with phi-sweep are anisotropic. Thus, a value is given for the length of the axis in the deposition plane and the axis length in the shadowing plane separately.

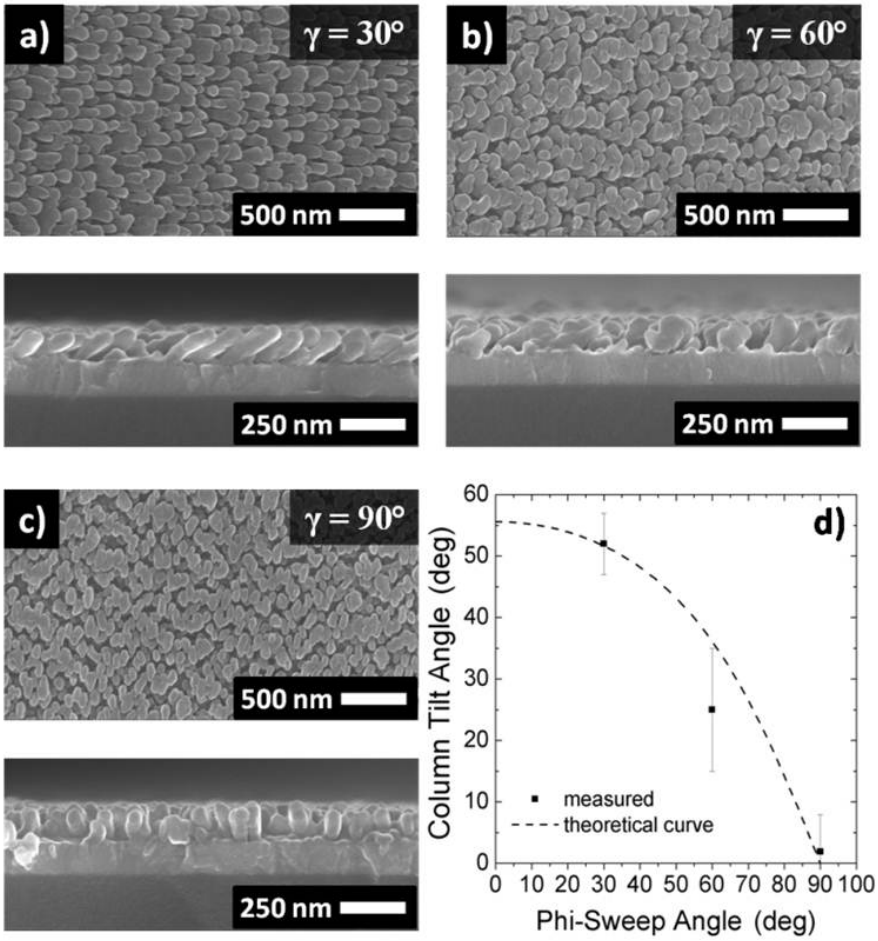

Figure 4.5. *(a),(b),(c) Films deposited using phi-sweep motion control with increasing γ = 30°, 60° and 90°, respectively. The side-views show the columns tilted toward the evaporation source (d) Tilt angle of C_{60} columns measured from the substrate normal plane. The line shows the theoretical expectation derived from a ballistic model.* ©*2011 IEEE. Reprinted, with permission, from [31].*

4.4 Summary

C_{60} films were successfully deposited and patterned using GLAD on ITO substrates. While previous work has demonstrated GLAD C_{60} columns on silicon and indium tin oxide (ITO) coated substrates, [171], this chapter has significantly broadened the possibilities for structuring GLAD C_{60}: Inter-column spacing is controlled by tilting the substrate and confirmed by ab-

Table 4.3. *Summary of column diameters in phi-sweep grown films at $\alpha = 80°$ for different ϕ-sweep amplitudes. Along the deposition plane, i.e. axis between evaporation source and center of substrate rotation, columns are thinner. Due to anisotropic shadowing columns are broader in the plane orthogonal to deposition plane, and widen with increasing phi-sweep angles.*

ϕ-sweep Amplitude (°)	**Column Diameter (nm)**	
	in deposition plane	in shadowing plane
30	50 ± 5	90 ± 10
60	50 ± 5	100 ± 10
90	50 ± 5	115 ± 15

sorbance measurements and SEM images. In addition, column diameter control was employed using the ϕ-sweep method. The C_{60} nanocolumns grow polycrystalline which is beneficial for charge transport and hence for the use in OPVs.

Precision nanostructuring forms a great foundation for investigating the possible improvement of OPVs using morphology engineering. While an ideal architecture such as a chess board pattern of C_{60} nanocolumns with equal spacing is postulated to be most optimal [11, 24], GLAD as shown in this chapter provides a strong morphology control which facilitates the study of the effect of nanostructuring on the performance of OPVs. The random distribution of C_{60} nanocolumns could be avoided by using a substrates with a periodic growth seed pattern. This approach would require substrate patterning which would work against the goal of providing a method for inexpensive morphology engineering of OPVs.

In particular, the most important parameter to optimize in order to increase exciton harvesting will be intercolumn spacing of acceptor nanocolumns. The following chapters will investigate the effect of intercolumn spacing on OPV device performance.

CHAPTER 5

POLYMER FILLED ORGANIC PHOTOVOLTAIC CELLS[1]

5.1 Introduction

In this chapter we use the previously shown results to fabricate a complete inverted solar cell incorporating GLAD C_{60} nanocolumns (Figure 5.1 a,b). Inverted architecture bulk heterojunction organic photovoltaics have been previously demonstrated, with power conversion efficiencies approaching 4.5%. [135, 139, 175] In this work, we endeavored to fabricate inverted polymer-fullerene heterojunctions, utilizing the C_{60} films prepared by GLAD as the platform on which these devices were built. However, both the planar and GLAD C_{60} films prepared in this study were soluble in common solvents normally used to solubilize the standard BHJ polymer (P3HT) including chloroform, dichlorobenzene, chlorobenzene, and dichloromethane. Immersion of the GLAD C_{60} films in all of these solvents resulted in their destruction and dissolution.

[1] Parts are reproduced with permission from [29]. Copyright 2011 American Chemical Society.

Therefore, in the first part of this chapter, we investigate the stability of the C_{60} nanostructures to solvents in an effort to develop a procedure for introducing a complementary donor polymer phase to complete the photoactive layer. Once a suitable donor-solvent combination is found, the effective nanostructure control possible with GLAD and its effect on device performance is investigated.

5.2 Device Architecture and Electronic Structure

In order to investigate the effect of GLAD structuring, or more precisely, intercolumn spacing on device performance, OPVs as shown in Figure 5.1 were fabricated and analyzed. While different donor filling procedures were attempted, e.g. donor evaporation into the GLAD structured films, the most successful approach seemed to be the spin-coating of a donor material into the GLAD structured C_{60} films. Incorporating interfacial layers, the overall electronic structure is illustrated in Figure 5.1(c) as an open-circuit model. As an interfacial layer Cs_2CO_3 is used [139]. Despite its slightly higher energy level compared with the LUMO of C_{60}, the use of Cs_2CO_3 significantly improved yield and device performance. As described later in this chapter, poly[3-(4-carboxybutyl)thiophene-2,5-diyl] or P3CBT, will be found as a suitable donor polymer for this study.

5.2.1 Films Used in This Study

Table 5.1 outlines the different vertical columnar GLAD structures used in this study. For all of the GLAD films a 10 *nm* planar C_{60} layer was deposited before depositing the described morphology on top. Of each morphology 2 chips with 5 devices each were fabricated using different spin speeds during

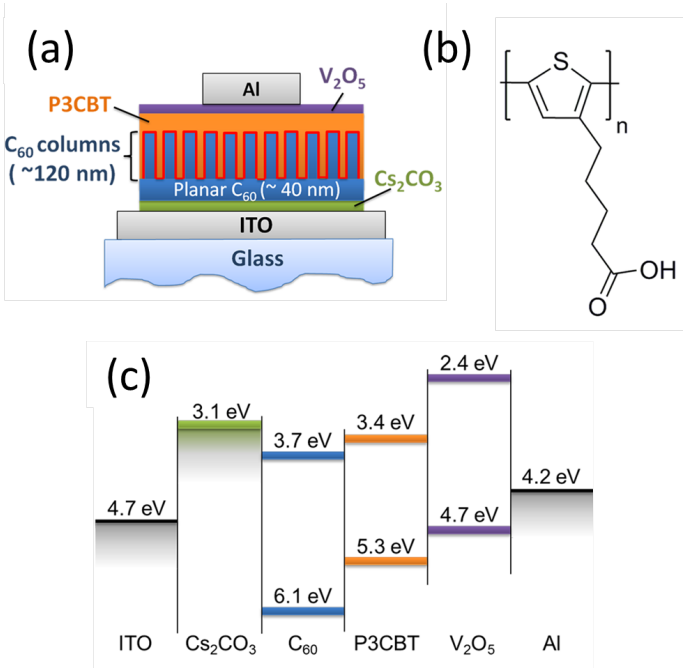

Figure 5.1. *(a) Architecture for an inverted OPV device based on nanostructured C_{60}/P3CBT multilayers. (b) P3CBT monomer, the in this study used donor material. (c) Corresponding electronic structure for the proposed device architecture. Reproduced with permission from [29]. Copyright 2011 American Chemical Society.*

donor coating to find the optimal device.

5.3 Polymer Filling of GLAD Structured C_{60}

In order to fill the fabricated GLAD C_{60} columns with a donor polymer a suitable process solvent has to be found. When testing the GLAD C_{60} films with chlorobenzene, dichlorobenzene or chloroform, i.e. non-polar solvents, the films immediately dissolved and when measuring the result in the SEM only the substrates were visible. Therefore, a series of alternative process solvents was tried. Due to the spherical symmetry of a C_{60} molecule its polarization is low ($\varepsilon_r \simeq 4.1$ to 4.4 [148]). One can assume that the GLAD C_{60} columns

Table 5.1. *GLAD C_{60} thin film morphologies used for this study.*

Morphology	Thickness (nm)	Column Spacing (nm)	Column Diameter (nm)
C_{60} planar	20 ± 10		
C_{60} ($\alpha = 70°$)	120 ± 10	15 ± 5	80 ± 20
C_{60} ($\alpha = 75°$)	120 ± 10	40 ± 20	90 ± 10
C_{60} ($\alpha = 80°$)	120 ± 10	65 ± 20	90 ± 10
C_{60} ($\alpha = 85°$)	120 ± 10	180 ± 90	100 ± 20

will be more stable when a solvent with a high polarity is used. Table 5.2 shows a variety of possible solvents for OPV fabrication. As a measure for the solvent's polarity its dielectric constant ε_r is presented.

Table 5.2. *A choice of organic solvents and their dielectric constants for OPV fabrication on GLAD C_{60} films. Dielectric constants are taken from [176].*

Solvent	ε_r	Solubility of C_{60}
Pyridine	13.26	dissolution
Acetonitrile	36.64	redeposition
Tetrahydrofuran	7.52	dissolution
Dimethyl sulfoxide	47.24	stable
Dimethylformamide	38.25	-
Acetone	21.01	stable
Water	80.10	-

Before deciding on dimethyl-sulfoxide as the solvent, several other solvents with higher polarity than the commonly used solvents were tested. For all solvents, GLAD C_{60} films deposited at $\alpha = 80°$ were rinsed in the solvent for about 1 *min* and then left to dry.

Figure 5.2 shows the different solvents tried. Redeposition was observed for acetonitrile (ACN) which would increase when using 1:1 and 9:1 solutions of acetonitrile and tetrahydrofuran (THF). The higher the solvent polarity the more delamination of the GLAD C_{60} was observed, especially when using methylene-chloride or applying a 1:1 solution of acetonitrile and pyridine. Entire dissolution occured in a 1:1 solution of dimethylformamide and water.

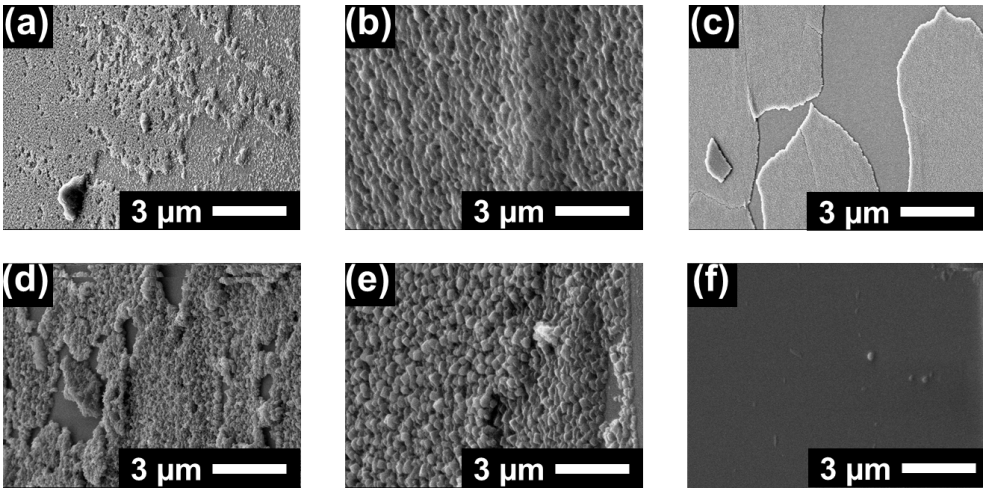

Figure 5.2. *Solubility Study of C_{60} deposited on silicon. (a) 1:1 of tetrahydrofuran and acetonitrile. (b) Acetonitrile. (c) 1:1 of acetonitrile and pyridine (d) Methylene-chloride. (e) 9:1 of acetonitrile and tetrahydrofuran. (f) 1:1 Dimethylformamide and water.*

5.3.1 GLAD C_{60} Film Stability in DMSO

Better results were achieved using dimethyl-sulfoxide (DMSO). Figure 5.3 shows a cross-section SEM image of an $\alpha = 80^\circ$ GLAD C_{60} film before DMSO testing and an SEM image taken at an oblique angle of 30° after rinsing for 1 *min*. The GLAD morphology is preserved and redeposition does not occur.

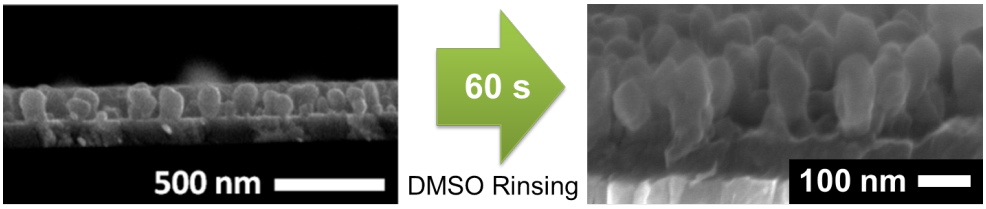

Figure 5.3. *SEM images of GLAD C_{60} deposited at $\alpha = 80^\circ$ on ITO/glass. After rinsing in DMSO for 60 s the GLAD morphology remains stable. Reproduced with permission from [29]. Copyright 2011 American Chemical Society.*

In order to investigate whether the mass volume of the film is conserved after the DMSO rinsing, absorbance measurements were taken (see Figure

5.4). The measurement compares a GLAD C_{60} film before rinsing, after the DMSO treatment and after rinsing in chloroform. The absorbance curves of the sample before and after DMSO rinsing are nearly identical while half the rinsing time in chloroform is enough to dissolve and rinse most of the C_{60} film off the substrate.

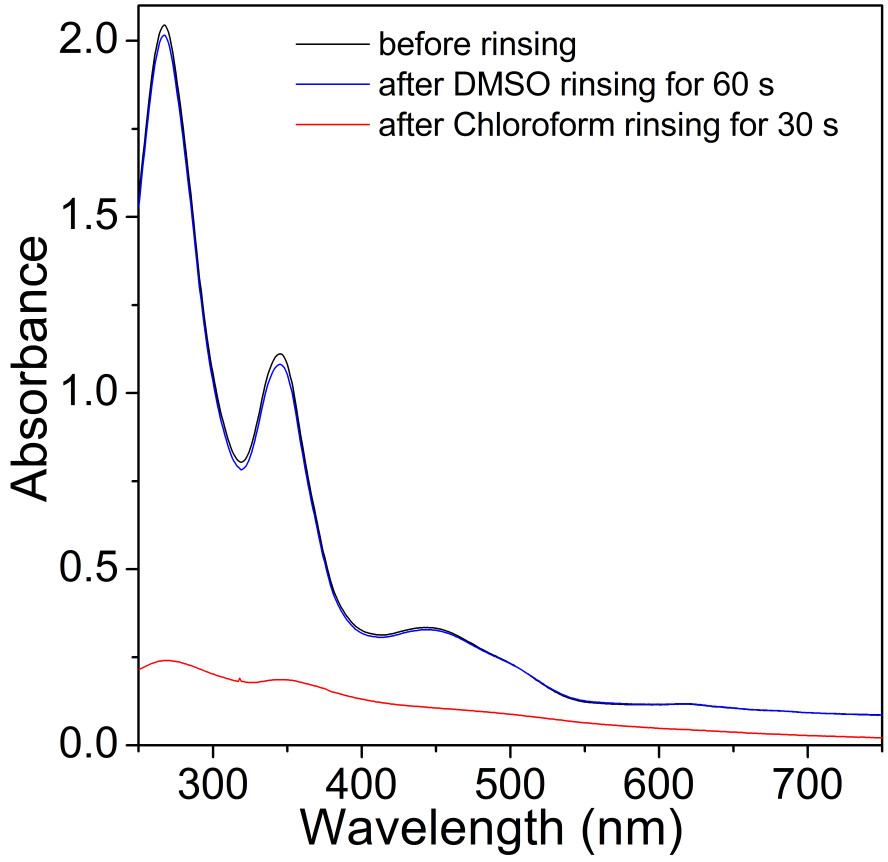

Figure 5.4. *Absorbance spectroscopy of GLAD C_{60} deposited at $\alpha = 80°$ on fused silica. After DMSO rinsing for 60 s the absorbance spectrum remains nearly congruent with the pristine film. Rinsing for half the time in chloroform leads to an absorbance spectrum with much lower intensity. Reproduced with permission from [29]. Copyright 2011 American Chemical Society.*

5.3.2 Filling Calibration

Members of the P3CBT family of polymers (Figure 5.1c) have been previously reported to be soluble in DMSO, and thus this group of polymers seemed to have properties complementary to the GLAD-prepared C_{60} nanocolumns. P3CBT has similar optoelectronic properties as P3HT [177, 178] and previously published P3CBT:PCBM bulk heterojunctions were shown to have power conversion efficiencies of 0.9 % [32]. Therefore, P3CBT was chosen to fabricate polymer filled inverted OPVs.

Our processing is based on the spin-coating process described in [179]. In order to find an optimum polymer layer filling process, a thickness calibration was performed. Figure 5.5 shows SEM cross-section images of GLAD C_{60} deposited on ITO/glass at $\alpha = 80°$. P3CBT dissolved in DMSO was spin-coated on top. The spin coating parameters were kept constant with a spin speed 600 rpm and a spin time of 5 min.

The P3CBT concentration in the DMSO was varied. As expected, the donor film thickness increases with growing concentration. A minimum concentration of 20 $mg\,ml^{-1}$ is necessary to cover the GLAD C_{60} columns entirely, however polymer surface roughness is still high. 30 $mg\,ml^{-1}$ seems to be the ideal concentration for device manufacturing and is applied throughout this chapter.

5.4 Limitations to Polymer Filling into C_{60}

Cross-sectional SEM images show what is apparently good infiltration of the donor polymer into the C_{60} nanostructure fabricated at $\alpha = 75°$ (see Figure 5.6a), but closer analysis of a microtomed sample by TEM (Figure 5.6b) shows voids between the C_{60} nanocolumns where the polymer does not make full

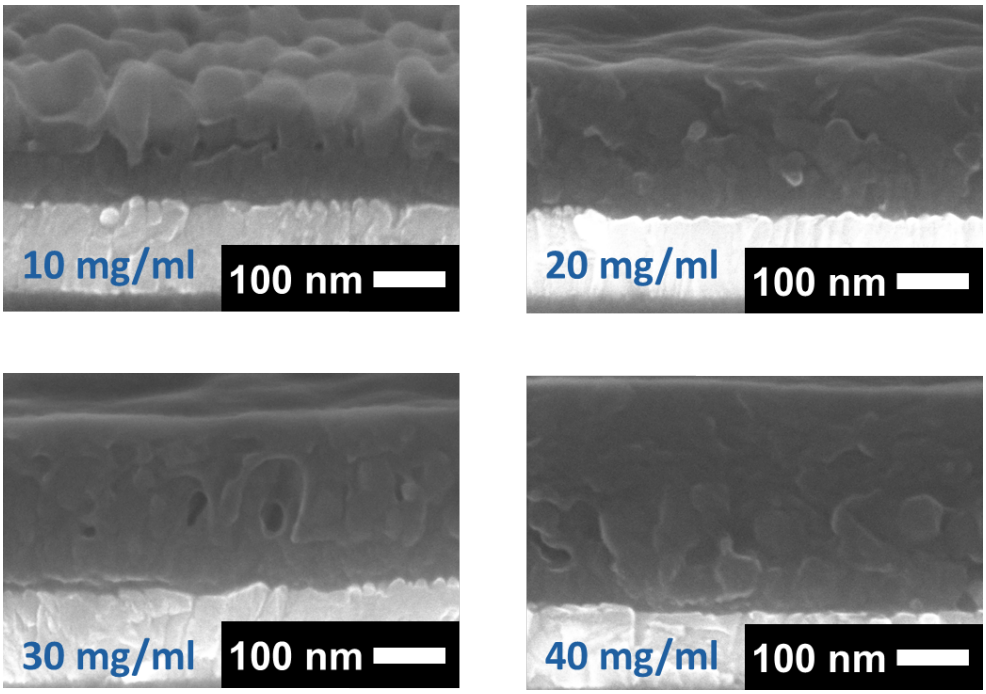

Figure 5.5. *Thickness calibration of P3CBT dissolved in DMSO spin-coated onto a GLAD C_{60} film deposited at $\alpha = 80°$ on ITO/glass. Spin speed (600 rpm) and time (5 min) were kept constant while P3CBT concentration was varied.*

contact with the C_{60}. This result may be due to a high viscosity of the DMSO-P3CBT solution. Filling into GLAD structures was investigated previously and similar effects observed [180]. It can be speculated that when the surface tension of the process solvent is high, such as in the case of DMSO, infiltration into GLAD structure with its intercolumn spacing at the range of about 100 nm might cause a capillarity effect where the process solution of solvent and polymer is prevented from filling the pores.

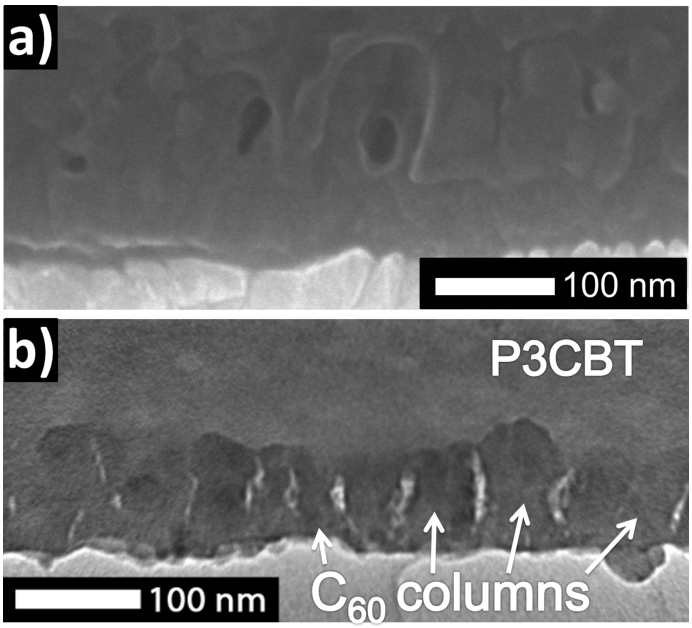

Figure 5.6. *Cross-sectional electron microscopy images of C_{60} nanostructures, fabricated at $\alpha = 75\ ^\circ$, with spun-on P3CBT. (a) SEM image (secondary-electron mode) image. To increase the contrast of the C_{60} columns, the measurement stage was tilted by $10\ ^\circ$ towards the detector. (b) TEM image (bright-field). Reproduced with permission from [29]. Copyright 2011 American Chemical Society.*

5.5 Absorbance and Exciton Quenching in C_{60}/P3CBT Multilayers

Absorbance spectra of GLAD C_{60}/P3CBT films are shown in Figure 5.7. The multilayer structures are comprised of the following layers: fused silica/planar C_{60} (50 nm)/GLAD C_{60} (120 nm)/P3CBT for the GLAD structures, and fused silica/C_{60}(170 nm)/P3CBT for the planar film. C_{60} absorption peaks are observed at 266 and 346 nm, and the broad feature at $\lambda = 550$ nm is due to the C_{60} peak at $\lambda = 455$ nm (compare with Figure 4.3) convolved with another from the P3CBT. As the processing for the P3CBT layer was identical for all films and the fact that this overlapping C_{60}/P3CBT feature varies with deposition angle, it is apparent the absorption results primarily from the C_{60} constituent of the heterojunction. The P3CBT peak onset appears at 650 nm, indicating an optical band gap of ~ 1.9 eV. The P3CBT peak at 553 nm is caused by the π stacking of thiophene rings, which leads to increased absorption in the bulk polymer, and increases with a higher degree of ordering. [32]

In order to qualitatively estimate exciton quenching for different morphologies, photoluminescence (PL) spectra of GLAD-based C_{60}/P3CBT heterojunctions on silica were taken and compared with planar films. These samples were fabricated simultaneously with the OPV devices described below and thus should have comparable architectures. In addition, a single P3CBT film, and planar C_{60} film were fabricated on silica as references. To account for differences in film thickness and absorbance, the P3CBT-only absorbance spectrum was normalized to the spectrum of the P3CBT in the multilayered samples. As can be seen in Figure 5.8, significantly more excitons were quenched in the GLAD C_{60}/P3CBT film as compared to the planar

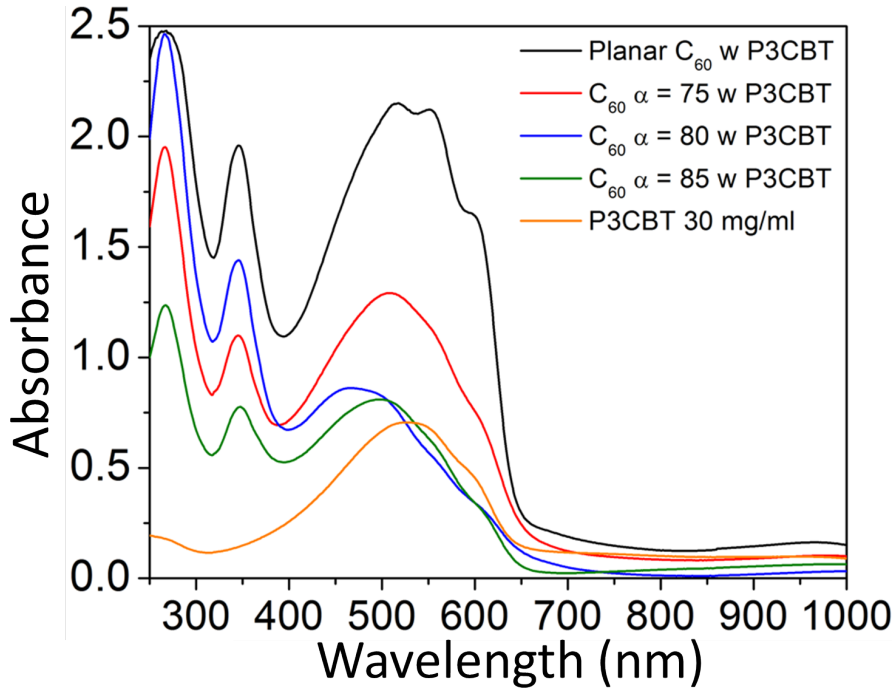

Figure 5.7. *Absorption spectra of nanostructured C_{60} films with spun-on P3CBT (30 $mg\ mL^{-1}$), as well as the spectrum for a single P3CBT layer (red curve). Reproduced with permission from [29]. Copyright 2011 American Chemical Society.*

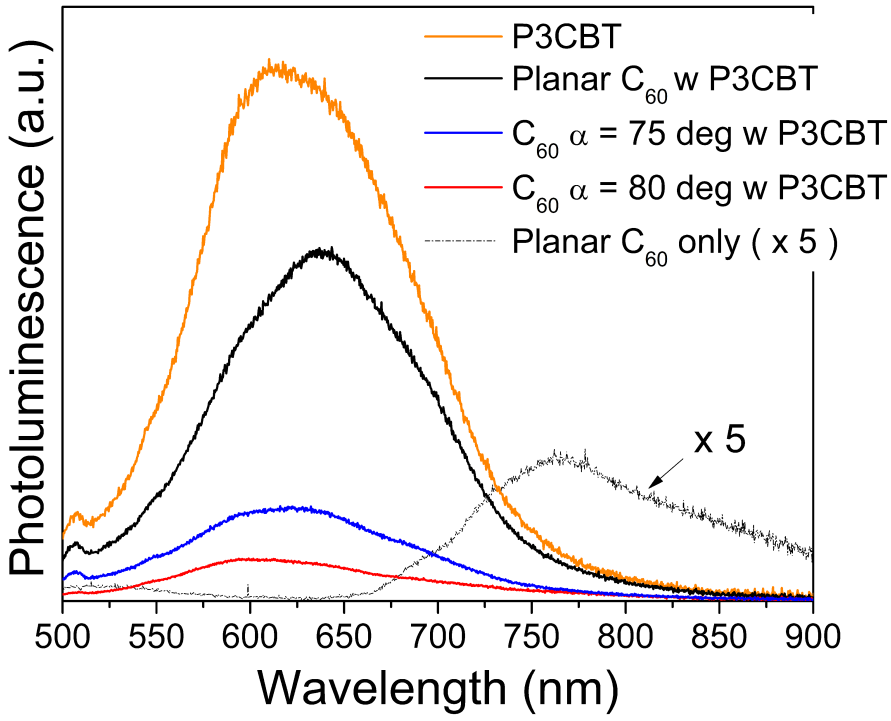

Figure 5.8. *Photoluminescence spectra of samples on silica substrates. A single P3CBT film is shown together with C_{60}/P3CBT double layers, as well as the magnified spectrum of a planar C_{60} GLAD film. Reproduced with permission from [29]. Copyright 2011 American Chemical Society.*

films. Interestingly, the exciton quenching for the multilayer made at $\alpha = 75°$ was slightly less than for $\alpha = 80°$, although the $\alpha = 75°$ device performed better (see following section). The J_{SC} might be larger for $\alpha = 75°$ because of a higher mass density of the polycrystalline C_{60} film providing an enhanced conductive path, but the reasons for this behavior are not yet fully understood.

In the investigated multi-layers, the number of excitons can decrease due to thermal recombination, radiative recombination, or exciton dissociation at the heterointerface [54]. The number of excitons which radiatively recombine are estimated in the PL spectrum. A decrease in PL when comparing

GLAD structured double layers compared to planar double layers suggests that more excitons are quenched due to exciton dissociation at the heterointerface.

5.6 Morphology Effect on Device Performance

In order to investigate the morphology effect on device performance, $J-V$ curves were measured under dark and light (1 sun, AM 1.5) conditions (see Figure 5.9).

Comparing light curves, OPVs based on the C_{60}/P3CBT heterointerface have similar open-circuit voltages (V_{OC}), but the short-circuit current density (J_{SC}) depends on C_{60} film morphology. The device made at $\alpha = 75^{\circ}$ exhibits the highest short-circuit current at $(4.60 \pm 0.20)\ mA\ cm^{-2}$. As a comparison, the characteristic curve of a BHJ based on P3CBT:PCBM is shown - while the J_{SC} is lower than in both GLAD C_{60} cells, the V_{OC} is slightly higher. Although P3CBT has similar optoelectronic properties as P3HT, the hole mobility has been reported to be $1.5 \times 10^{-4}\ cm^2V^{-1}s^{-1}$, which is significantly lower than commonly reported values for P3HT ($5 \times 10^{-3}\ cm^2V^{-1}s^{-1}$), which reduces charge transport in the devices [181]. The dark curves of the GLAD C_{60} cells and the BHJ have comparable slopes above the turn-on voltage, indicating that the series resistance is comparable. Series resistance seems to be higher for the planar C_{60}/P3CBT device than in all previously mentioned OPVs; the interfacial layers and electrodes were fabricated using the same process for these devices, and thus an increase in series resistance can be attributed to less efficient charge extraction from the double layer. To illustrate the dissolution of the C_{60} layer during the spin-coating of P3HT in chloroform, we have added the $J-V$ curve of a planar C_{60}/P3HT device. The very low slope

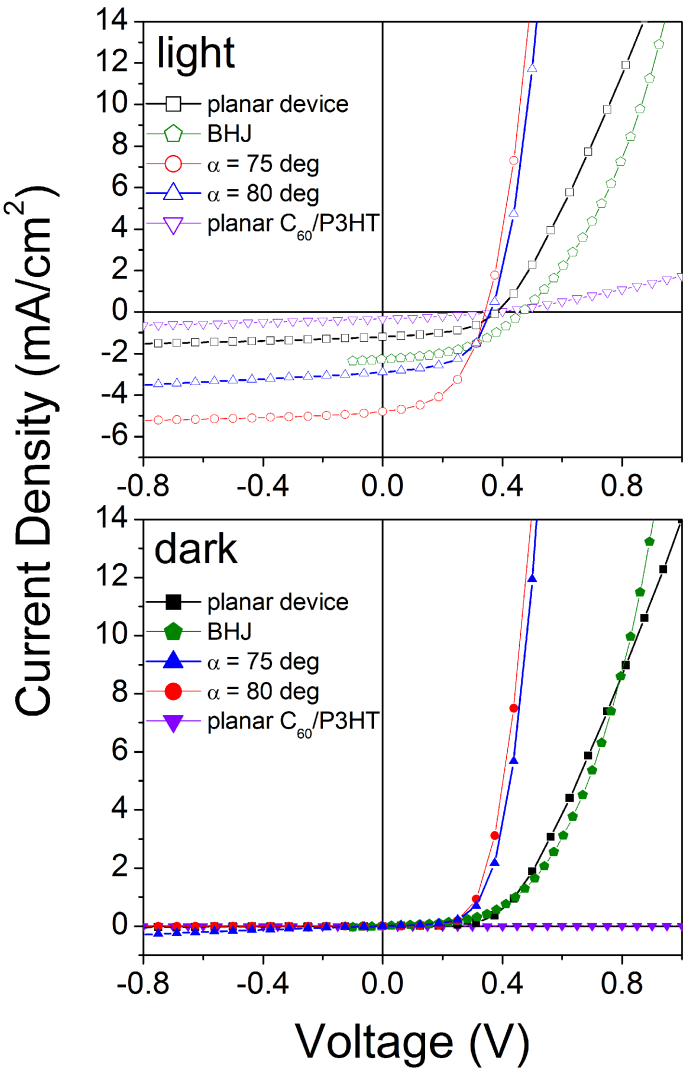

Figure 5.9. *$J - V$ characteristics of OPVs. Devices based on planar C_{60} (glass/ITO/Cs_2CO_3/C_{60}(planar)/P3CBT/V_2O_5/Al) and C_{60} GLAD films fabricated at $\alpha = 80°$, $\alpha = 75°$, and $\alpha = 70°$ are shown. For comparison, a BHJ [32] and a planar C_{60} device with P3HT as donor polymer are included. Reproduced with permission from [29]. Copyright 2011 American Chemical Society.*

of the dark curve suggests a high resistivity of the architecture, and the corresponding light curve has very low photoactivity. These effects result from dissolution of C_{60} because few C_{60} molecules remain to form a heterointerface with the P3HT.

Table 5.3. *Comparison of performance values for the inverted OPVs based on planar and nanostructured C_{60} films. For each deposition angle, multiple devices were fabricated and characterized. The average and standard deviation values are measured from at least 10 separate devices fabricated in one process.*

Active Layer	$J_{SC}(mA\,cm^{-2})$	$V_{OC}(V)$	FF
C_{60} planar,P3CBT	0.92 ± 0.05	0.37 ± 0.01	0.55 ± 0.05
C_{60} ($\alpha = 70°$),P3CBT	3.20 ± 0.25	0.34 ± 0.02	0.42 ± 0.04
C_{60} ($\alpha = 75°$),P3CBT	4.60 ± 0.20	0.33 ± 0.01	0.45 ± 0.01
C_{60} ($\alpha = 80°$),P3CBT	3.02 ± 0.12	0.35 ± 0.02	0.47 ± 0.06
P3CBT:PC_{61}BM	2.25 ± 0.05	0.45 ± 0.02	0.44 ± 0.01
C_{60} planar,P3HT	0.30 ± 0.10	0.30 ± 0.17	0.33 ± 0.14

Table 5.4. *Comparison of power conversion efficiencies for the inverted OPVs based on planar and nanostructured C_{60} films. For each deposition angle, multiple devices were fabricated and characterized. The average and standard deviation values are measured from at least 10 separate devices fabricated in one process.*

Active Layer	$PCE(\%)$	best $PCE(\%)$
C_{60} planar,P3CBT	0.20 ± 0.03	0.23
C_{60} ($\alpha = 70°$),P3CBT	0.47 ± 0.08	0.66
C_{60} ($\alpha = 75°$),P3CBT	0.80 ± 0.20	1.00
C_{60} ($\alpha = 80°$),P3CBT	0.56 ± 0.06	0.62
P3CBT:PC_{61}BM	0.49 ± 0.03	0.52
C_{60} planar,P3HT	0.03 ± 0.03	0.05

Table 5.3 and Table 5.4 summarizes the results for the prepared devices. The V_{OC} was measured to be $(0.37 \pm 0.01)\ V$ in the planar device which is slightly higher than in all three GLAD devices. Because V_{OC} is highly dependent on device processing [182] these values indicate a consistent process quality. The V_{OC} in all of our inverted GLAD devices are, however, lower than the value measured in a BHJ based on P3CBT:PCBM $(0.45 \pm 0.02)\ V$, with the same interfacial layers and electrodes. Although a slight decrease in V_{OC} for the BHJ would be expected due to the different LUMO level in PCBM,

which is located at about 4 eV instead of 3.7eV for the C_{60} films [183,184], the major difference in V_{OC} is attributed to the atmospheric exposure during the processing of our multilayered devices that might affect the C_{60}/P3CBT interface.

In the BHJ device, the OPV is fabricated from a mixed solution including PCBM and P3CBT, and during the spin coating deposition of the BHJ the PCBM:P3CBT interface forms in solution during solvent evaporation, thus reducing the interface's atmospheric exposure. In the GLAD device process, a vacuum break occurs after finishing the C_{60} deposition by GLAD and before the P3CBT spin coating step. Although particular care was used in handling the samples and keeping samples under inert atmosphere during vacuum breaks, some amount of oxygen and moisture contamination of the C_{60} surface is expected [146], leading to a lower V_{OC} than in the fully solution processed BHJ. In addition, the V_{OC} of the BHJ inverted devices (0.45 V) is lower than previously reported forward-mode BHJ devices (0.60 V) [32], indicating that further tuning of the Cs_2CO_3 and V_2O_5 interfacial modifiers could improve the V_{OC}. With further process improvement and minimization of atmospheric exposure of the C_{60} films, it is expected that V_{OC} and thus PCE can be improved.

With a higher heterointerfacial area and improved matching of the column spacing to the exciton diffusion length, the number of dissociated excitons, and thus J_{SC}, is expected to increase. Table 5.3 shows a significant increase in J_{SC} for the nanostructured devices relative to the planar samples. The $\alpha = 80^\circ$ and $\alpha = 75^\circ$ GLAD devices show three- and five-fold respective increases in J_{SC} relative to the planar device.

Consequently, the power conversion efficiencies (PCE) for nanostructured devices are significantly higher. Compared with a mean PCE of $(0.20 \pm$

0.03) % in the planar samples, mean PCEs of (0.8 ± 0.2) % and (0.56 ± 0.06) % are achieved in devices fabricated at $\alpha = 75^\circ$ and $\alpha = 80^\circ$, respectively. Relative to the planar device, the BHJ device showed a two-fold increase in J_{SC}. This is less than the 5-fold increase of the best GLAD device ($\alpha = 75^\circ$) and suggests that the ordered interface provided by nanocolumnar C_{60} is an improvement over the disordered BHJ interface, maximizing surface area while maintaining a beneficial morphology for charge transport.

A further improvement would be expected when going to lower deposition angles and thus decreasing column spacing to better match the exciton diffusion length of the polymer. The devices fabricated at $\alpha = 70^\circ$, however, do not show further improvement. Their J_{SC} is at $(3.20 \pm 0.25)\ mA\ cm^{-2}$ and the achieved PCE is (0.47 ± 0.08) %, which is comparable with the device fabricated at $\alpha = 80^\circ$. This result is attributed to poor filling of the polymer into the tightly spaced column array, leading to a decreased photoactive surface area compared with the $\alpha = 75^\circ$ device. A $J - V$ curve for OPVs can be modeled using diode behavior. Because the quality of a heterointerface in a diode determines the shape of the $J - V$ curve, a change in ideality, i.e. a change in $J - V$ curvature, might occur for different heterointerface configurations. As previously mentioned, P3CBT coverage at the nanostructured C_{60} interface is only partly complete when using DMSO as the solvent (Figure 5.6b, p. 76). This may cause $J - V$ curve non-idealities which lower the fill factor (FF) for the nanostructured devices compared with the planar samples.

5.7 Summary and Conclusions

Nanocolumn C_{60} films were fabricated by glancing angle deposition. A variety of process solvents was investigated for GLAD C_{60} OPV fabrication.

Dimethyl-sulfoxide was found to allow donor processing without destroying the GLAD morphology of the C_{60} films.

Inverted organic photovoltaic cells were fabricated by filling P3CBT into the GLAD C_{60} films and by employing V_2O_5 as a hole transparent layer and Cs_2CO_3 as an electron transparent layer. The P3CBT filling resulted in voids when being filled into the GLAD structured devices.

Various device morphologies were prepared and compared: planar devices, bulk heterojunctions, and GLAD structured devices. Morphology control improves interface structuring and increases exciton harvesting. GLAD structured devices have significantly outperformed conventional architectures. A fourfold increase in PCE between a planar device and the GLAD device at $\alpha = 75^\circ$ as well as a twofold increase in PCE between an optimized bulk heterojunction and the same GLAD device architecture demonstrates the importance of interface structuring and morphological control, which allows for improved exciton harvesting.

To match the exciton diffusion length of polythiophenes, about 5 to 20 nm, the maximum C_{60} column spacing could be estimated between 10 to 40 nm. OPV devices were fabricated starting with nanostructured C_{60} films produced at $\alpha = 75^\circ$ and $= 80^\circ$, resulting in an average column spacing of about 40 and 65 nm, respectively. Nevertheless, the key result of this chapter as shown in Figure 5.10, supports the hypothesis of an increased exciton harvesting when intercolumn spacing is approaching the exciton diffusion length of the donor material.

However, compared with state of the art PCEs from other single junction materials systems, the devices investigated in this chapter cannot reach comparable efficiencies. This can have various reasons. The hole conductivity in P3CBT was found to be comparably low to state of the art donor polymers.

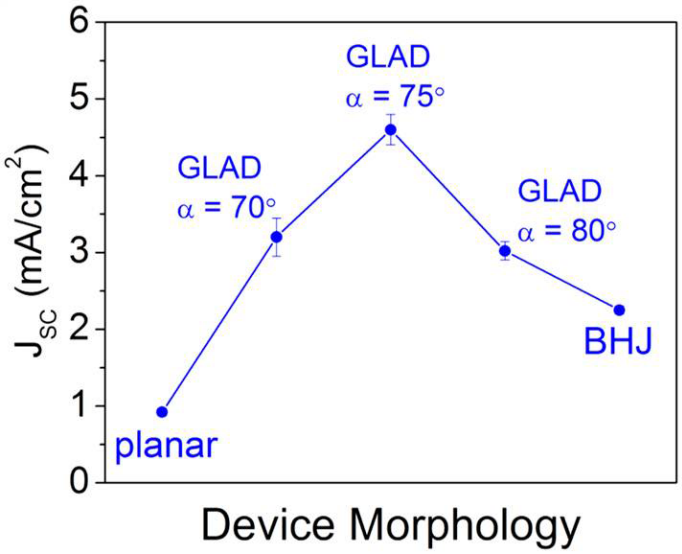

Figure 5.10. *Figure of merit for J_{SC} at different morphologies for GLAD devices, planar films and bulk heterojunctions (BHJ) of C_{60} and P3CBT.*

In addition, incomplete filling decreases the heterointerface quality and thus less excitons are harvested than potentially possible. The versatility of the glancing angle deposition process however may improve other materials systems where device architectures with nanostructural ordering are beneficial. A material system based on a small molecule donor is investigated in the next chapter.

CHAPTER 6

SMALL MOLECULE FILLED ORGANIC PHOTOVOLTAIC CELLS[1]

6.1 Introduction

In the previous chapter OPVs were built based on polymer processing. Small molecules, however, allow for better morphology control [22, 68] and several fabrication approaches can be used, such as thermal evaporation [185], organic phase vapor deposition [63, 186], solution-processed blending [187, 188], blending through co-deposition [22,23,189], and glancing angle deposition [29,127,129,130,161,190]. Since the polymer filled OPVs in the previous chapter showed a two-fold increase in short-circuit current compared with bulk heterojunctions, further suitable solvent-donor combinations are investigated in this chapter in order to fully exploit this potential. A major challenge was identified when filling the C_{60} nanocolumnar structure with the polymer solution through spin coating. The C_{60} films dissolved in most commonly used solvents such as chloroform or dichlorobenzene and we were re-

[1]Parts are reprinted from Organic Electronics [30], Copyright (2012), with permission from Elsevier.

quired to use dimethyl-sulfoxide as solvent which limited the choice of donor materials we could use and resulted in poor donor filling of our nanocolumnar C_{60} structures. This leads us to consider alternate donor materials.

6.2 Architecture for 3-Q Based OPVs

In this chapter, devices with an active layer made entirely from small molecules are fabricated and thus demonstrate a processing route which can be used together with GLAD fabricated nanocolumnar C_{60} films (as shown in Figure 6.1). The star molecule 3-Q (4,4′,4″,4‴-(5,5′,5″,5‴-([2,1,3]benzothiadiazole-4,5,6,7-tetrayl)tetrakis(3-hexylthiophene-5,2-diyl))tetrakis(N,N-diphenylaniline)) [161] (as shown in Figure 6.1 c) is soluble in acetone which is a strong advantage when working with C_{60} fullerene films since acetone does not dissolve the C_{60} and thus does not adversely affect the GLAD nanocolumnar morphology. We use spin coating of 3-Q into the GLAD C_{60} films and investigate the filling properties and effect on device performance.

6.2.1 Films Used in This Study

In the previous chapter, optimum GLAD C_{60} morphologies were investigated and in order to compare with the results in the previous chapter similar GLAD structures were used here. Table 6.1 shows the different films fabricated. In addition, results from the bulk heterojunctions of 3-Q and $PC_{61}BM$ were used for comparison [161]. For the GLAD structured films, a planar 10 nm C_{60} film was deposited first before GLAD columns were deposited on top of this base layer.

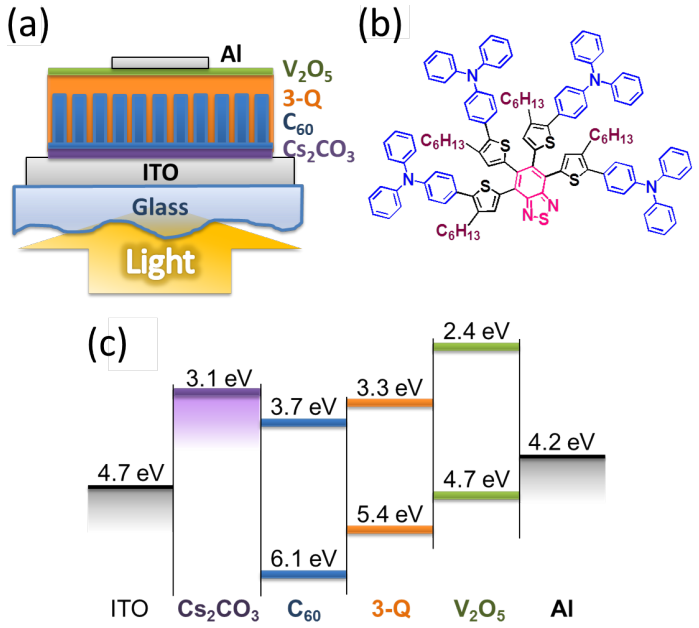

Figure 6.1. *Device concept: (a) Device architecture with a nanocolumnar C_{60} fullerene film filled with 3-Q donor molecules. (b) 3-Q star molecule. (c) Corresponding electronic structure including interfacial layer Cs_2CO_3 and hole transparent layer V_2O_5. Reprinted from [30], Copyright (2012), with permission from Elsevier.*

Table 6.1. *The deposited C_{60} morphologies for this study.*

Morphology	Thickness (nm)	Column Spacing (nm)	Column Diameter (nm)
C_{60} planar	20 ± 5		
C_{60} ($\alpha = 75°$)	130 ± 15	40 ± 10	90 ± 10 *nm*
C_{60} ($\alpha = 80°$)	120 ± 10	60 ± 10	105 ± 10 *nm*

6.2.2 Morphology of Samples

Morphology control is central to this work and follows techniques previously reported in detail for fabricating nanocolumnar films [29]. The thicknesses of both morphologies of GLAD C_{60} films are nominally 160 *nm*. C_{60} average column diameters are (90 ± 10) *nm* for the $\alpha = 75°$ and (105 ± 10) *nm* for the $\alpha = 80°$ films, as seen in Figure 6.2. Intercolumn spacing is controlled by adjusting the deposition angle α and results from ballistic shadowing of the incoming particle flux during deposition. The average spacing was mea-

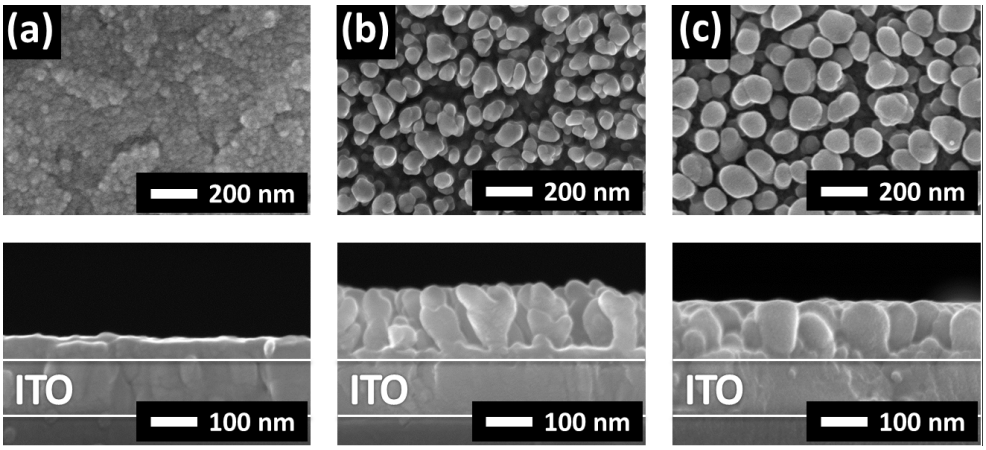

Figure 6.2. *Scanning electron microscopy images of glancing angle deposited C_{60} fullerene films with top (image above) and side views (image below). (a) Planar C_{60} film. (b) C_{60} film deposited at $\alpha = 75°$. (c) C_{60} film deposited at $\alpha = 80°$. The ITO layer is marked with lines; above is the C_{60} film and below is glass. Reprinted from [30], Copyright (2012), with permission from Elsevier.*

sured to be (40 ± 10) *nm* for films deposited at $\alpha = 75°$ and (60 ± 10) *nm* for $\alpha = 80°$. Intercolumn spacing affects both the filling properties of the spin coated donor and the heterointerface area, and in addition, exciton harvesting can improve when intercolumn spacing more closely matches the exciton diffusion length of the donor which is estimated to be about 10 to 20 *nm*. For comparison in Figure 6.2 (a), a 20 *nm* thick planar film is shown, and it is observed that there is some minor surface roughness, perhaps originating from the roughness of the underlying ITO.

6.3 3-Q Filling Advantage

6.3.1 Acetone as Process Solvent

In the previous chapter we found that the use of the donor solvent is one of the main limitations for subsequent solution processing of our GLAD structured C_{60} OPVs. The challenge is to find a solvent which does not dissolve

the nanostructured C_{60} films while at the same time provides a good filling of donor molecules into the nanocolumnar structures. Since C_{60} fullerenes are highly symmetric molecules and therefore have low polarity, C_{60} films can easily be dissolved in non-polar solvents such as chloroform or chlorobenzene which are commonly used in OPV fabrication [29]. In contrast, acetone is a polar aprotic solvent and nanocolumnar C_{60} is stable when treated with this solvent. Consequently, the choice of solvent limits the applicability of various donors to the device. The commonly used poly(3-hexylthiophene-2,5-diyl) (P3HT) dissolves in some non-polar solvents, however it does not dissolve in acetone. In contrast, 3-Q does dissolve in acetone and therefore can be used for spin coating on nanocolumnar C_{60}.

6.3.2 Improved Filling

Figure 6.3 shows the GLAD structured C_{60} films after spin coating with 3-Q dissolved in acetone. Compared with previous results [29], a good infiltration of 3-Q into the nanocolumnar structures is observed. In particular, a previously observed drawback using dimethyl-sulfoxide (DMSO) as solvent were voids and empty pockets after spin coating [29]. Contact angle measurements of DMSO and acetone on a planar C_{60} film were performed. For DMSO a contact angle of $(27 \pm 3)^\circ$ was observed. However, acetone instantly wetted the C_{60} surface and no contact angle could be measured. Hence, due to the lower polarity of acetone, filling of a donor into nanocolumnar C_{60} films is significantly improved.

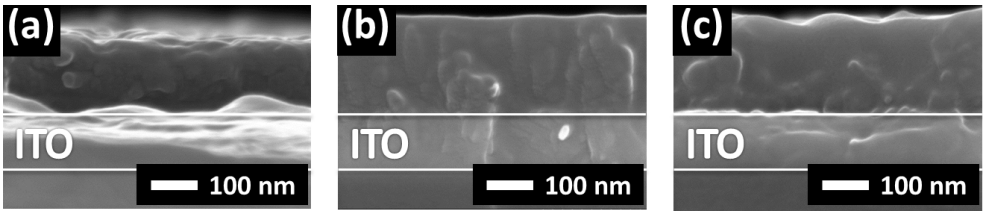

Figure 6.3. *Scanning electron microscopy images after spin coating of 3-Q onto the C_{60} films. (a) Planar C_{60} film with planar 3-Q film on top. Due to variations in cleaving the substrate the photoactive layer cleaved further back from the edge than the ITO substrate. (b) C_{60} film deposited at $\alpha = 75°$ with infiltrated 3-Q. (c) C_{60} film deposited at $\alpha = 80°$ with infiltrated 3-Q. Reprinted from [30], Copyright (2012), with permission from Elsevier.*

6.4 Absorbance of C_{60}/3-Q Multilayers

Figure 6.4 shows the absorbance of C_{60}/3-Q double layers. For comparison, spectra for a pure 3-Q film and a pure GLAD C_{60} film deposited at $\alpha = 80°$ are included. The pure C_{60} spectrum is in agreement with the previously measured spectra in chapter 4 and 5. A C_{60} peak observed at 344 nm. In addition, C_{60} causes the broad peak formation between 400 nm and 500 nm with a local maximum at 450 nm. The mass density of C_{60} films decreases with increasing deposition angles α [45], leading to the decreasing absorption of the C_{60} peaks when going from $\alpha = 75°$ to $\alpha = 80°$. The 3-Q absorbance spectrum has two broader regions, one at around 515 nm, which is comparable with the absorption in P3HT, and one at lower wavelengths of around 350 nm which provides additional sensitivity in the ultraviolet. The onset for the 3-Q spectrum appears at $\sim$ 615 nm indicating an optical band gap of 2.0 eV which is in agreement with a band gap of 2.09 eV measured in [161]. It can be observed that the C_{60}/3-Q double layer peaks are of higher absorption compared with the bulk heterojunction spectrum, due to the lower thickness of the bulk heterojunction's active layer.

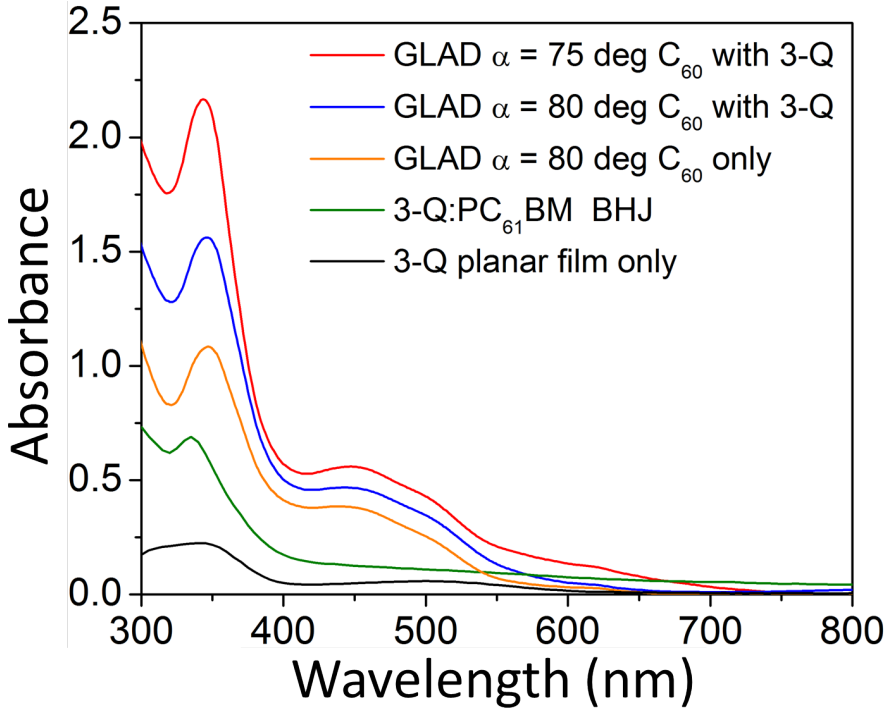

Figure 6.4. *Absorbance spectra of a GLAD C_{60} films filled with 3-Q. For comparison, a 3-Q:$PC_{61}BM$ bulk heterojunction, a pure GLAD C_{60} film deposited at $\alpha = 80°$ and a pure planar 3-Q film are shown. (Vertical order in legend follows vertical sequence of graphs) Reprinted from [30], Copyright (2012), with permission from Elsevier.*

6.5 Device Performance

$J - V$ characteristics of the fabricated devices were measured and are shown in Figure 6.5 where GLAD device performance is compared to bulk heterojunction and planar devices. Table 6.2 shows the average device parameters and Table 6.3 shows the power conversion efficiencies for each device.

The open circuit voltage is lower in GLAD devices compared with the bulk heterojunction, as also observed in the previous chapter. A decrease in V_{OC} is expected for the BHJ, since the lower LUMO level in PCBM is located at about 4 eV instead of 3.7eV for the C_{60} films [183, 184]. The lower

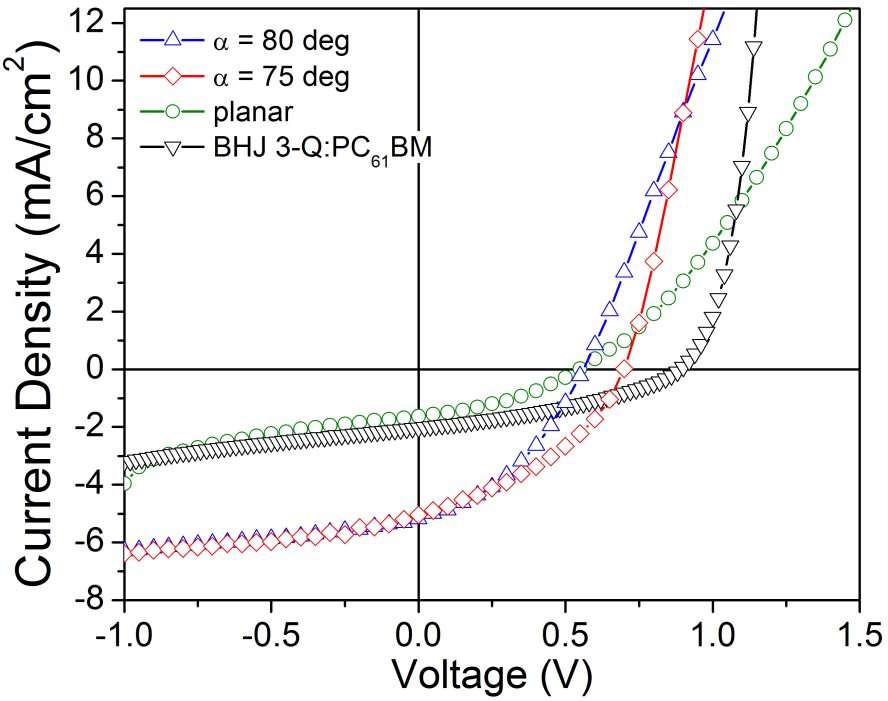

Figure 6.5. *Example $J-V$ characteristics of GLAD devices compared with a planar device and a bulk heterojunction. Reprinted from [30], Copyright (2012), with permission from Elsevier.*

Table 6.2. *Performance parameters for fabricated device series. All thermally evaporated devices have the following architecture: glass /ITO/Cs_2CO_3/active materials/V_2O_5/Al. For comparison, the values for a 3-Q:$PC_{61}BM$ heterojunction are added. For each deposition angle, multiple devices were fabricated and characterized. The average and standard deviation values are measured from at least 10 separate devices fabricated in one process. Reprinted from [30], Copyright (2012), with permission from Elsevier.*

Active Layer	$J_{SC}(mA\,cm^{-2})$	$V_{OC}(V)$	FF
C_{60} ($\alpha = 75°$),3-Q	4.1 ± 0.3	0.7 ± 0.1	0.33 ± 0.03
C_{60} ($\alpha = 80°$),3-Q	4.7 ± 0.5	0.5 ± 0.1	0.34 ± 0.05
C_{60} planar,3-Q	1.3 ± 0.3	0.6 ± 0.1	0.38 ± 0.05
3-Q:$PC_{61}BM$	2.0 ± 0.01	0.9 ± 0.01	0.38 ± 0.01

open-circuit voltage in planar and GLAD devices could be attributed due to oxygen exposure during device fabrication.

Table 6.3. *Power conversion efficiencies for fabricated device series. For comparison, the values for a 3-Q:$PC_{61}BM$ heterojunction are added. For each deposition angle, multiple devices were fabricated and characterized. The average and standard deviation values are measured from at least 10 separate devices fabricated in one process. Reprinted from [30], Copyright (2012), with permission from Elsevier.*

Active Layer	$PCE(\%)$	best $PCE(\%)$
C_{60} ($\alpha = 75°$),3-Q	1.0 ± 0.2	1.4
C_{60} ($\alpha = 80°$),3-Q	0.8 ± 0.3	1.3
C_{60} planar,3-Q	0.3 ± 0.1	0.5
3-Q:$PC_{61}BM$	0.7 ± 0.1	0.8

The short-circuit current is significantly increased in the GLAD devices and has doubled compared with the bulk heterojunction which validates our approach to GLAD structure these devices. The GLAD structuring has increased exciton harvesting which can be directly observed by the increase in J_{SC}. The highest PCE of 1.4 % is observed for the GLAD devices fabricated at $\alpha = 75°$. This PCE is a two-fold improvement over the bulk heterojunction and a three-fold improvement relative to the planar device.

In addition, series resistance seems to be lower in the GLAD device fabricated at $\alpha = 75°$ than for the planar device which in addition can improve J_{SC}. This improvement in internal resistance may be attributed to the interpenetrating columnar morphology which might be more efficient at extracting charge carriers than the planar double layer architecture.

Both GLAD devices perform similarly within error ranges. V_{OC} is slightly lower for the $\alpha = 80°$ device compared with the $\alpha = 75°$ device. This behavior could be attributed to a lower shunt resistance which also leads to a slight variation in V_{OC} between both GLAD devices. This could be due to slight variations in device quality resulting from differences in air exposure during fabrication. This variation of V_{OC} has not been observed for the GLAD C_{60}/P3CBT devices.

6.6 Summary

Organic photovoltaic devices based on glancing angle deposited C_{60} fullerene films filled with donor 3-Q small molecules have been fabricated and characterized. The use of acetone significantly improved donor filling compared with previously reported devices which used dimethyl-sulfoxide as process solvent for poly[3-(4-carboxybutyl)thiophene-2,5-diyl]. In addition, the morphology of the nanocolumnar C_{60} fullerene films was preserved when using acetone. The resulting nanocolumnar devices were compared with a bulk heterojunction and a two-fold increase in power conversion efficiency of GLAD fabricated devices was observed. The GLAD nanocolumnar morphology allows thicker devices and thus increased absorbance compared with bulk heterojunctions while enabling an effective conductive path for charge carriers.

The fabrication process using acetone and a small molecule donor 3-Q provides a route to improved performance in inverted OPVs utilizing C_{60} in a nanocolumnar architecture. Together with the work in the previous chapter and here we have shown a two-fold short-circuit current increase due to our GLAD structured morphology compared with bulk heterojunctions in two different material systems, one utilizing a conjugated polymer P3CBT, the other using a small molecule 3-Q. This is a strong indication that this architecture would be able to achieve superior performance compared with state-of-the-art bulk heterojunctions if an appropriate solvent-donor combination can be found which can complement the C_{60} nanocolumnar structure.

6.7 Comparison of P3CBT and 3-Q Devices

Figure 6.6 shows a comparison of the main device parameters of GLAD OPVs fabricated using P3CBT as well as using 3-Q.

V_{OC} is increased in BHJs. This increase for the BHJ is attributed due to oxygen exposure of the heterointerface during fabrication of the planar and GLAD devices. Among the GLAD and planar devices there is only minor variation in V_{OC} which again may be attributed to variations in fabrication conditions, in particular air exposure times. This variation is higher for 3-Q devices compared with the P3CBT devices. One can speculate that the air exposure of C_{60} introduces defects to the heterointerface which can alter the energetic offset at the heterointerface. A too high energetic barrier can lead to exciton recombination instead of dissociating the exciton, a too low barrier will not overcome the exciton binding energy. Hence, the maximum possible photocurrent in the device is decreased.

The fill factors are within error range for the GLAD and BHJ devices which indicates comparable resistance behavior for both architectures. However, FF is higher for planar devices. Planar devices have a lower optimal photoactive layer thickness which can lead to lower internal resistance as compared to the thicker nanostructured devices. In addition, variance is generally higher for FF than for the other performance parameters for all devices. Since J_{SC} and V_{OC} are more sensitive to the photoactive layer materials and morphology, this variance might be attributed to variance Al top electrode quality which can lead to changes in resistance. Different degrees of oxidation could result in series resistance variation of the Al electrodes. In addition, a variation in deposition rates of the Al top electrode can affect the layer homogeneity and possible pin holes can increase leakage currents.

GLAD structuring directly improves the short-circuit current for P3CBT and 3-Q devices. GLAD devices outperform planar morphologies and bulk heterojunctions. Despite having a presumably less efficient exciton dissociation in GLAD devices due to a lower heterointerface quality compared with BHJs, J_{SC} is significantly higher in the GLAD devices. This supports our main hypothesis that internal resistance in GLAD devices is decreased and charge extraction significantly improved due to the more ordered columnar morphology of donor and acceptor. In addition, J_{SC} is sensitive to the deposition angle α which indicates that exciton harvesting is dependent on the intercolumn spacing between C_{60} columns.

The power conversion efficiency numbers are calculated from the parameters above. The morphology dependent short-circuit current has the highest influence on PCE and dominates over the fabrication dependent V_{OC} and FF.

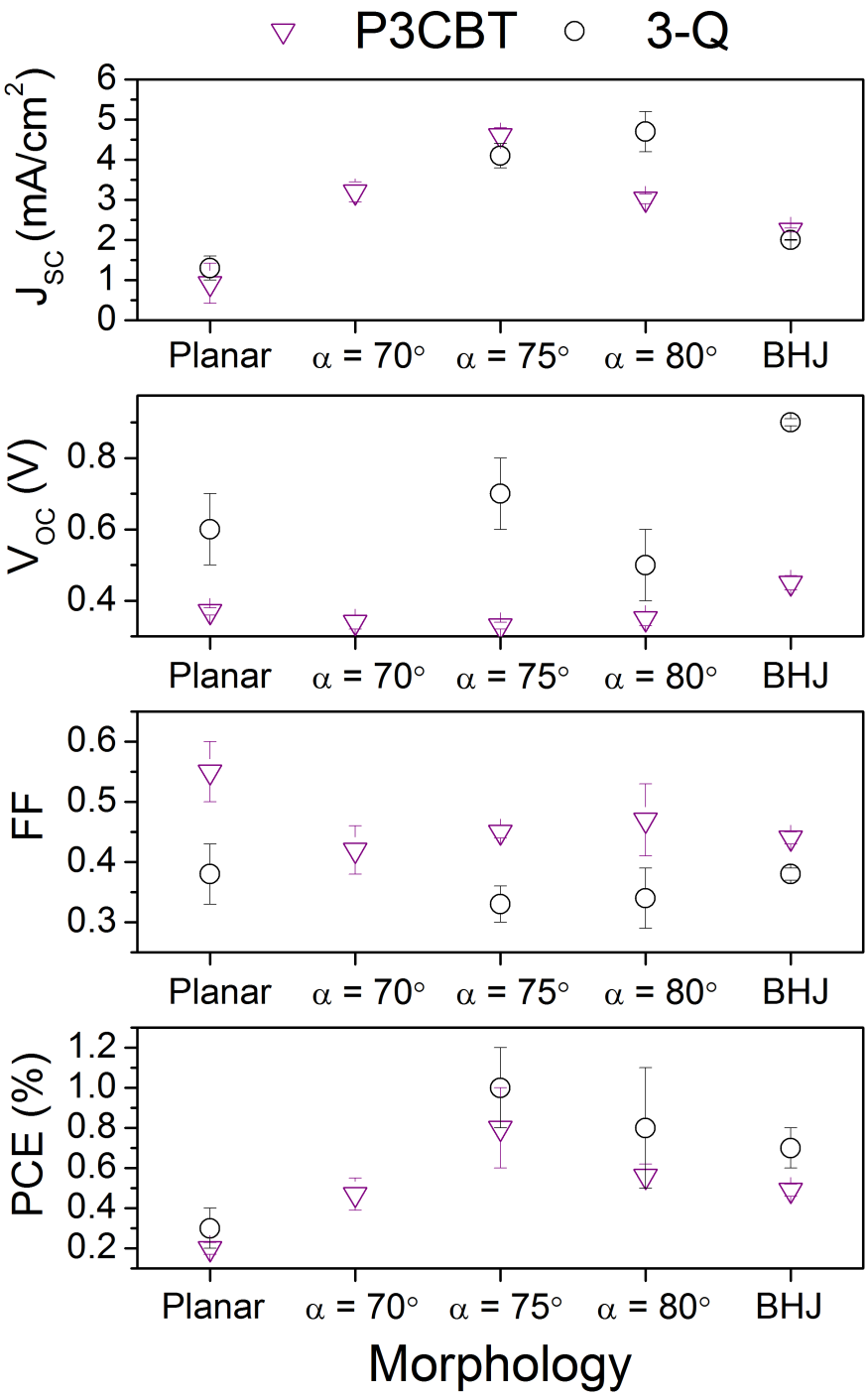

Figure 6.6. *Comparison of the main parameters of the fabricated GLAD OPVs. The graphs show short-circuit current J_{SC}, open-circuit voltage V_{OC}, fill factor FF, and power conversion efficiency PCE. The different GLAD structured devices are indicated by their deposition angles for $\alpha = 70°, 75°$, and $80°$.*

CHAPTER 7

PTCDA:C_{60} ACCEPTOR BLENDS FOR ORGANIC PHOTOVOLTAIC CELLS

From the results in the previous chapters it becomes clear that working with C_{60} alone as an acceptor for inverted GLAD structured OPVs leads to a variety of limitations such as:

- Solubility of C_{60} in DCB, CB and chloroform
- Very short lifetime of C_{60} films when exposed to ambient air
- High price of purified C_{60} powder for thermal deposition

On the other hand, C_{60} or $PC_{61}BM$ is the state of the art material for acceptors in OPVs due to its comparably high mobility of about $10^{-2}\ cm^2V^{-1}s^{-1}$ [88] and its beneficial crystallization during film growth. How could these advantages of C_{60} films be utilized while trying to avoid its limitations?

PTCDA (perylene-3,4,9,10-tetracarboxylic dianhydride) is an acceptor broadly researched as a model system for organic electronics [97]. In addition, PTCDA could be a complementary material to C_{60}, since its advantages could outweigh the described C_{60} limitations. PTCDA is stable when exposed to

air, in fact the molecule does contain oxygen atoms, and is comparably inexpensive. The drawback when using PTCDA is its low electron mobility of about 10^{-5} to 10^{-4} $cm^2V^{-1}s^{-1}$ [83].

The preliminary work in this chapter investigates whether both materials can be combined to achieve an optimum of the advantages of both while minimizing their limitations can be achieved. Similar approaches have previously been attempted. For example, co-deposition of donor and acceptor has been performed with CuPc and C_{60} [191]. In addition, F. Machui *et al.* have just recently investigated P3HT:PCBM bulk heterojunctions with a ternary low band gap donor polymer PCPDTBT [192]. Similarly, L. Chen *et al.* investigated a P3HT:PCBM bulk heterojunction with additional blending in of a PCBPy acceptor [110]. If a blend of PCTDA and C_{60} is suitable for OPVs, than this combined acceptor material could be beneficial as a photoactive layer as well as an improved interfacial layer for electron injection. This proposed approach is also very risky. The crux lies in the charge transport however, since blending might diminish the high charge transport from C_{60}. J. Kwiatkowski *et al.* proposed that disordered C_{60} films can have mobilities up to half of a single crystalline film [84]. Would PTCDA:C_{60} acceptor blends provide sufficient mobilities for OPV operation?

This is a preliminary study to test the combination of both acceptors and investigate if an optimum balance between all critical properties can be found. If the blending of both acceptors proves suitable, then these findings could provide a novel route for the fabrication of nanostructured inverted OPVs.

7.1 Experimental Details

Both materials are deposited using thermal evaporation, and blending is achieved through co-deposition as illustrated in Figure 7.1. Throughout this study a series of planar and GLAD acceptor blend films deposited at $\alpha = 80\ ^\circ$ is fabricated. Starting with pure PTCDA films the blending ratio is increased by adding C_{60} in steps of 25%at. Before depositing the blended films, deposition ratios for each pure film at $\alpha = 0\ ^\circ$ and $\alpha = 80\ ^\circ$ were measured and calibrated. Based on the deposition ratio and the measured deposition rate during deposition, each individual composition is targeted. Hence, each composition or blending ratio described is based on atomic per cent.

7.2 Morphology Engineering of Acceptor Blends

Previously, in chapter 4, we observed that C_{60} films can be GLAD structured. Attempting to structure PTCDA as well as blends of PTCDA and C_{60} was also successful. Figure 7.2 shows the series of GLAD structured PTCDA:C_{60} films.

While composition is controlled sufficiently well, overall film thickness seems to slightly increase with additional C_{60} and is at maximum for the $PTCDA_{50}$:$(C_{60})_{50}$ films before decreasing again towards the pure C_{60} film. This is likely caused by the minor differences in column microstructure and porosity. In addition, coalescence between the vertical columns seems to increase with increasing C_{60} content. While both pure films show a rather smooth surface, higher surface roughness can be observed for the blends at $PTCDA_{50}$:$(C_{60})_{50}$ and $PTCDA_{25}$:$(C_{60})_{75}$. It can be speculated that domains or even individual crystallites of single C_{60} or single PTCDA are formed within the nanocolumns.

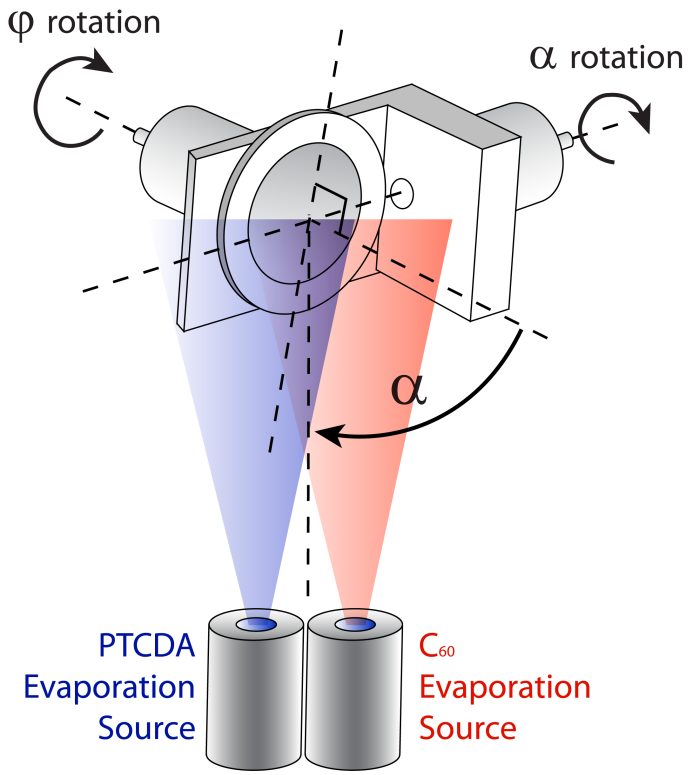

Figure 7.1. *The modified GLAD apparatus for the co-deposition of two acceptor materials. Two Al_2O_3 crucible sources are used for the thermal evaporation of C_{60} and PTCDA. Both crucibles are far enough from the substrate to allow for a collimated particle flux and homogeneous blending.*

Table 7.1 shows the by XPS estimated content of PTCDA in comparison to the targeted blending ratio by adjusting the deposition rates of both materials during the thin film evaporation. Since XPS is a surface sensitive technique, a variance of the PTCDA content of up to 10% can be expected in the deposited films. This is a reasonable result for this study, however, for future work, time-of-flight secondary ion mass spectrometry could be used in order to measure the film composition with higher accuracy. In addition, the fine tuning of both deposition rates during the acceptor co-evaporation could be improved by employing a computer control in order to balance both sources' evaporation temperatures.

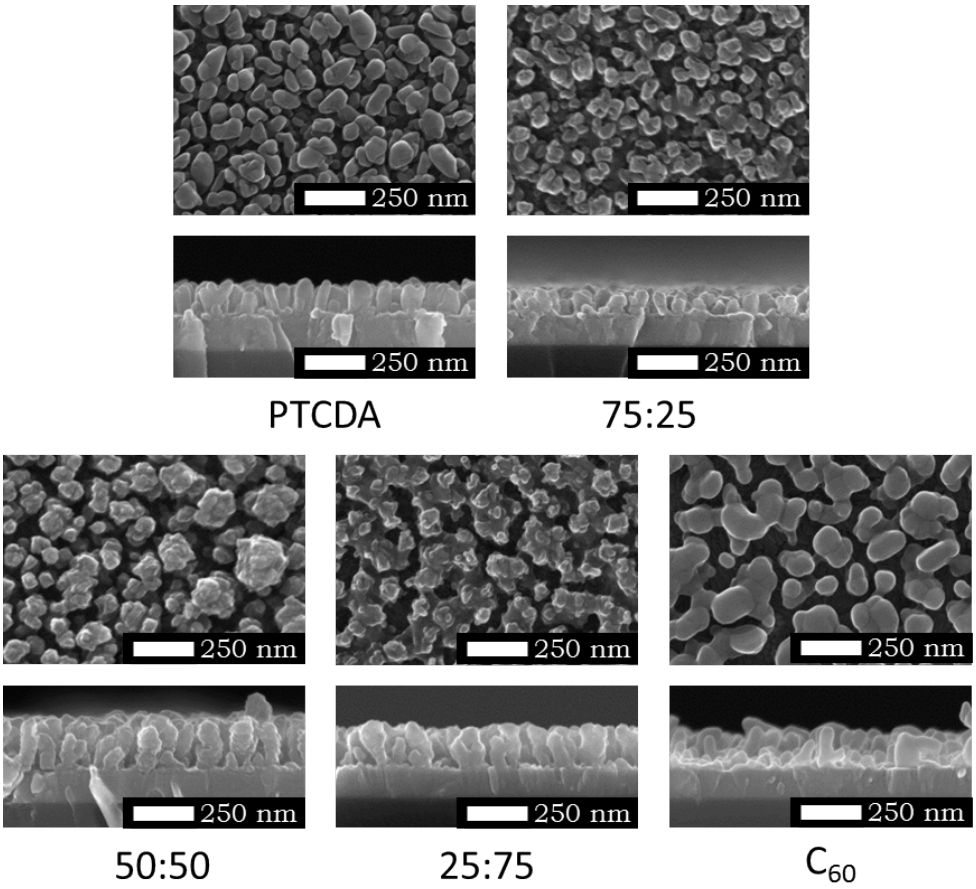

Figure 7.2. *SEM images of GLAD deposited PTCDA:C_{60} blends. As deposition angle $\alpha = 80^{\circ}$ was used. C_{60} concentration increases from 0 at.% to 100 at.% in increments of 25 at.%*

Table 7.1. *Estimated composition of PTCDA:C_{60} films determined by XPS on sample surface and as targeted by deposition rate ratio. XPS measurements and characterization were performed by Brian J. Worfolk.*

Blending Ratio PTCDA:C_{60}	**Estimated PTCDA Content**
100 : 0	100 *at.*%
75 : 25	62 *at.*%
50 : 50	58 *at.*%
25 : 75	22 *at.*%
0 : 100	0 *at.*%

7.3 Solubility of Blends and Donor Filling

In order to test the GLAD films for solubility every sample was spin coated in DCB at 600 rpm for 1 min. Afterwards the solvent test films were viewed in the SEM, as shown in Figure 7.3. PTCDA is observed to be stable after spin coating in DCB. Through addition of more C_{60} however, the solubility of the overall GLAD film increases and redeposition occurs. The GLAD structure is particularly altered for the $PTCDA_{25}$:$(C_{60})_{75}$ films. When applying DCB to the pure C_{60} film the entire film is dissolved.

This is an excellent result as it allows for polymer filling using DCB as the process solvent for some blending ratios. Therefore, P3HT spin coating was tried next. A solution of 20 $mg\,ml^{-1}$ of P3HT in DCB was prepared and spun onto the GLAD films at 600 rpm for 1 min. As shown in Figure 7.3, P3HT filling into the GLAD structure is successful and voids or open pocket domains were not observed. In addition, the filling results correlate with the solvent test results. Most distinct columns are observed for a higher content of PTCDA. When increasing the C_{60} content past the $50:50$ ratio, columns are less distinctive or dissolved entirely.

7.4 Extinction in Acceptor Blends

The extinction coefficient was measured for the entire series, as shown in Figure 7.4. The spectrum for the pure C_{60} films is in agreement with previously shown measurements in chapters 4 and 5. The pure PTCDA films show a peak formation from around 345 nm to 390 nm as well as a major convoluted peak near 478 nm followed by a peak at 555 nm. This peak formation is in agreement with previously measured absorbance spectra which exhibit a peak convolution at around 475 nm and an additional peak at about 560 nm

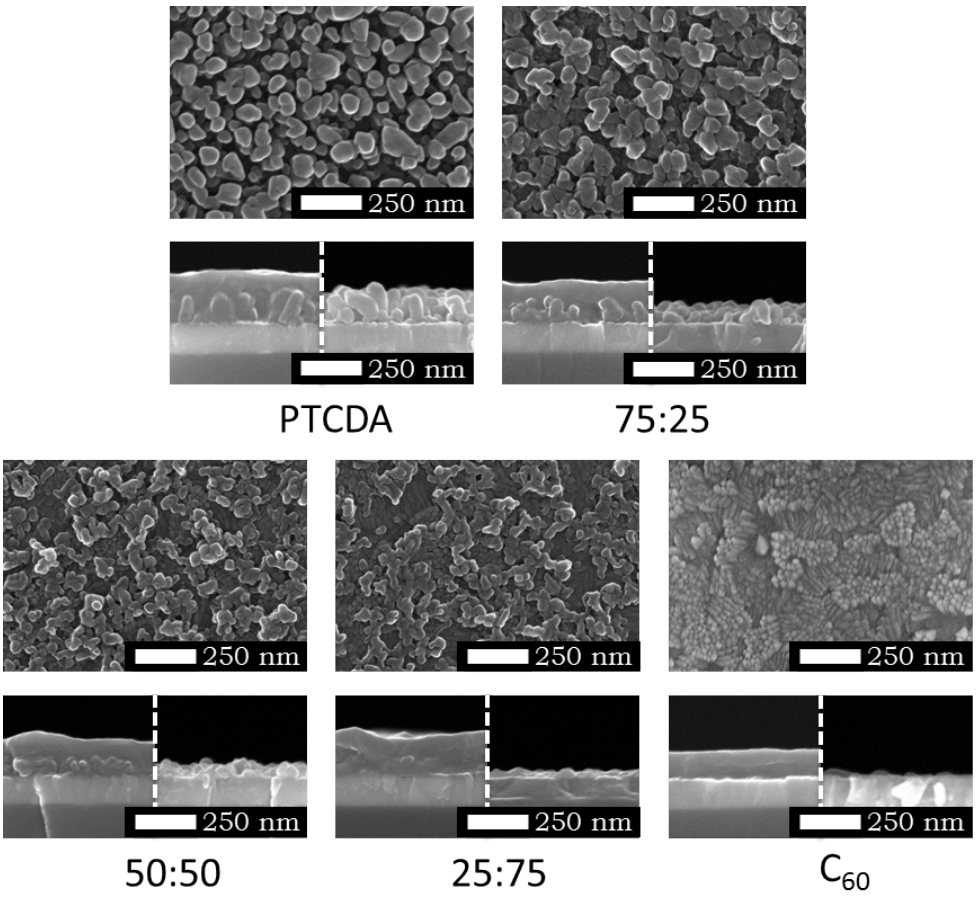

Figure 7.3. *SEM images of GLAD deposited PTCDA:C_{60} blends after spin-coating in pure o-DCB at* 600 *rpm for* 1 *min. The bottom-left cross-section images show spin-coated of* 20 *mg/ml P3HT dissolved in o-DCB onto the pristine GLAD structured PTCDA:C_{60} blends.*

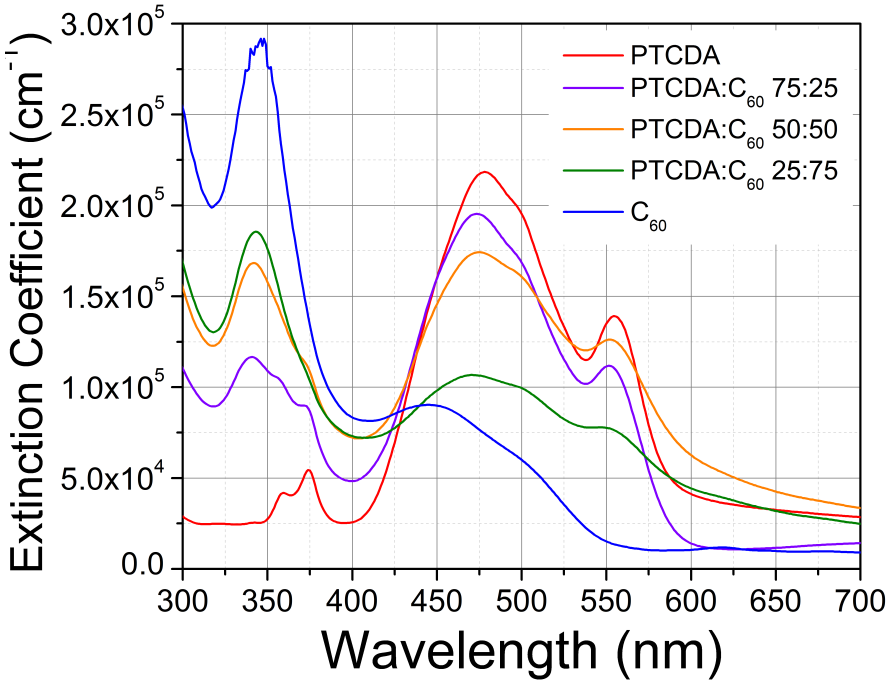

Figure 7.4. *Extinction coefficients of pure PTCDA, pure C_{60} and PTCDA:C_{60} blends.*

reported for PTCDA in [193,194].

From extrapolation of the extinction spectra onset the band gaps are determined to be 2.1 *eV* for PTCDA and 2.3 *eV* for C_{60} which is in agreement with previously reported 2.3 *eV* for C_{60} [195]. The PTCDA band gap value varies greatly in literature, I. Hill *et al.* determined 2.6 *eV* for PTCDA [196] using UPS while R. Schlaf *et al.* report 1.6 *eV* for the optical band gap and 2.22 *eV* from UPS [197]. The onset of the spectrum can only be used as an estimate for the optical band gap. Since the measured electron levels are not a line but in fact Gaussian distributed [85], reported values obtained from absorbance or UPS can shift dependent on the extrapolation method used. In addition, the band gap in PTCDA is sensitive to crystal structure [197].

When blending C_{60} together with PTCDA it becomes interesting whether

there are any interactions between the two different molecules. The acceptor blends show the same peaks at the same peak positions. Since peak positions do not change when blending occurs, it indicates that interactions between the molecules are not strong enough to change the electronic levels within each molecule. One can assume that the molecules interact through van-der-Waals forces and this interaction would not allow an overlap in molecular orbitals of both molecules, hence a change in electronic levels within the molecule is not expected.

In addition, the intensity of each peak is correlated with the overall content of each material in the blend. If the measured extinction is understood as an approximation to absorption, then by blending the two materials together absorption can be tuned and a broader absorption can be achieved. For donors, blending two materials together in order to achieve a broader absorption is favorable. The same is true for acceptors which can contribute to photocurrent as well [198], in fact C_{70} is employed, together or instead of C_{60}, in order to achieve broader absorption and therefore a higher efficiency [185, 199].

7.5 Investigation of Electronic Properties

The absorbance coefficient curves have shown that when both materials are blended together, peak positions do not shift. This is an indication that the interaction between PTCDA and C_{60} molecules is weak. In this section the electronic properties of the blends are directly examined. Using UPS the binding energy spectra of the acceptor films on ITO is obtained and shown in Figure 7.5. By extrapolating the secondary electron cut-off energy the work function of each sample is calculated through

$$\Phi = h\nu - E_{cut-off} \tag{7.1}$$

where Φ is the work function, h is the Planck constant, ν is the wavelength of the incident light, and $E_{cut-off}$ is the secondary electron cut-off energy. In addition, the interface dipole between the acceptor film and ITO is determined by measuring the shift in the secondary electron cut-off energy which corresponds to a change in the work function for each sample [200, 201]. The HOMO level is extrapolated from the onset of the valence band spectrum near the Fermi level [196, 202]. Finally, the ionization potential can be calculated as

$$IP = h\nu - E_{cut-off} + E_{HOMO} \tag{7.2}$$

where IP is the ionization potential and E_{HOMO} is the HOMO level of the sample.

The work function obtained here for ITO of 4.52 eV is in good agreement with the literature value of 4.5 eV for untreated ITO [203]. The ionization potential of the PTCDA film on ITO is determined to be 6.61 eV which is close to the value of 6.8 eV reported in [204]. For the C_{60} film on ITO an ionization potential of 6.16 eV is measured. This value is slightly lower than common ionization potentials for solid C_{60} which range anywhere from 6.3 eV to 7 eV depending on the substrate [183, 205–208]. Since UPS is a surface sensitive technique, surface contamination from air on C_{60} samples could occur during the transport to the UPS system. Such contaminations could possibly decrease the ionization potential of our C_{60} sample.

Table 7.2 summarizes the measured electronic levels in acceptor blends deposited on ITO. The table shows an increasing interface dipole with in-

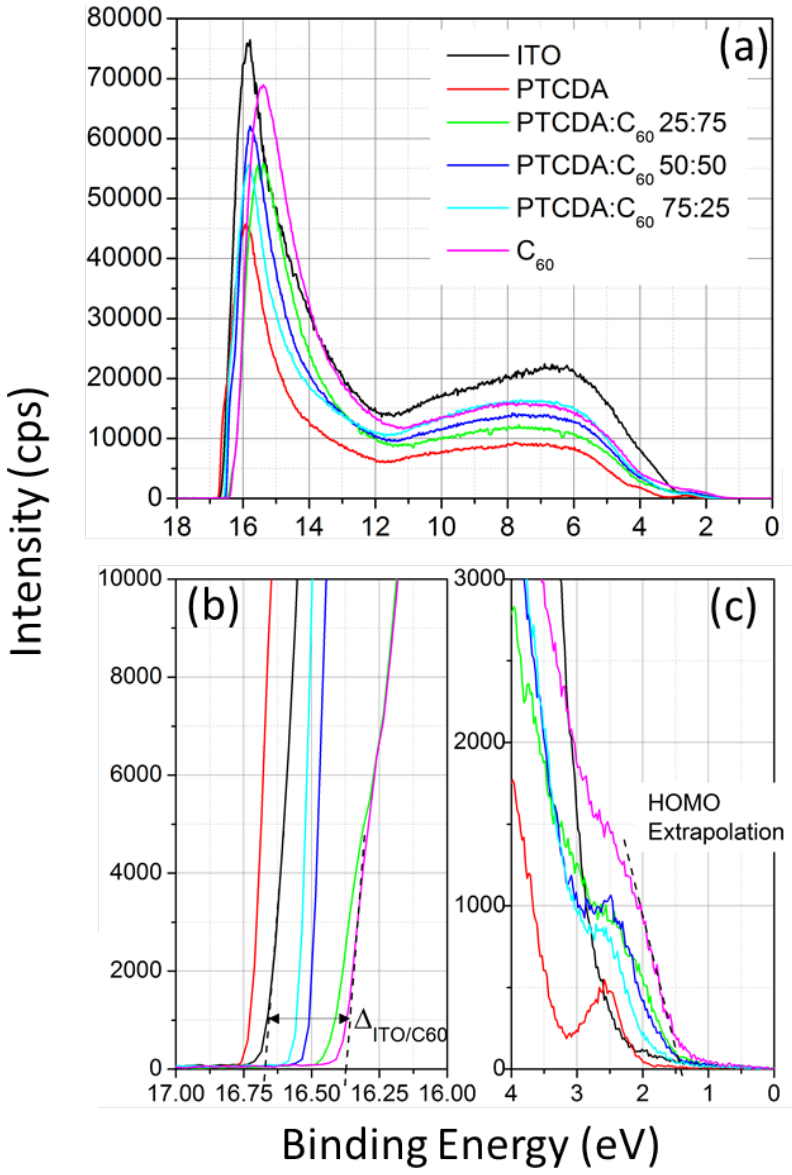

Figure 7.5. *UPS spectra of acceptor blends deposited on glass/ITO substrates. (a) The complete spectrum for each acceptor blend as well as the ITO substrate. (b) Secondary electron cut-off for each sample which is used to determine the work function and interface dipole. (c) Valence band spectra recorded near the Fermi level of ITO. The first onset represents the HOMO level in each sample. UPS spectra were collected by Brian J. Worfolk and Dr. Dimitre Karpuzov.*

Table 7.2. *Extrapolated electronic levels of PTCDA:C_{60} blends from UPS spectra. WF is the work function, Δ is the interface dipole between ITO and the acceptor film, and HOMO is the highest occupied molecular orbital level relative to the Fermi level of ITO. In addition, the optical band gap E_{gap} is shown as determined by absorbance measurements. Values were measured and extrapolated by Brian J. Worfolk.*

Blending Ratio PTCDA:C_{60}	$WF\ (eV)$	$\Delta\ (eV)$	$HOMO\ (eV)$
ITO only	4.52	0	2.54
100 : 0	4.47	-0.05	2.14
75 : 25	4.60	0.08	1.83
50 : 50	4.70	0.18	1.68
25 : 75	4.76	0.24	1.47
0 : 100	4.84	0.32	1.32

creasing C_{60} content. Based on these values and the optical band gap measurements, Figure 7.6 shows schematics for the electronic configurations for PTCDA and C_{60} on ITO. These diagrams illustrate the electronic similarity of C_{60} and PTCDA, in particular for the ionization potential and band gap.

It is obvious that the ionization potential for each single molecule does not change from blending. Nevertheless, a shift of the work function in the UPS spectra is observed, shown in Figure 7.7. This behavior is not yet understood. One possible route of explanation is that when combining the molecules in a solid film, extrinsic properties such as crystal structure can influence the electronic structure. In particular, structural defects can result in electronic traps and defect states [85]. Another explanation could be the formation of states at the ITO/acceptor interface. One indication for this hypothesis is the growing interface dipole when the C_{60} content in the blend is increased. This interfacial dipole could result from various interface effects. Acceptors have a high electron affinity by definition and therefore reaction with a contact surface is likely. For example, partial electron transfer from acceptor film to a metal has been reported [205] as well as reaction induced states between metals and PTCDA have been observed [209].

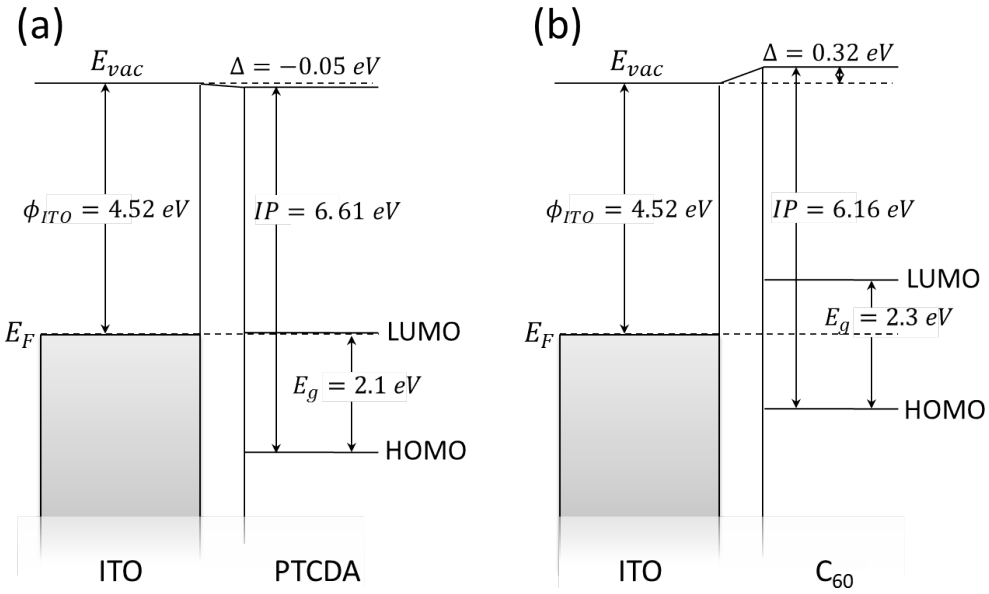

Figure 7.6. *Electronic configurations at the ITO/PTCDA and ITO/C_{60} junction as derived from UPS and extinction spectra.*

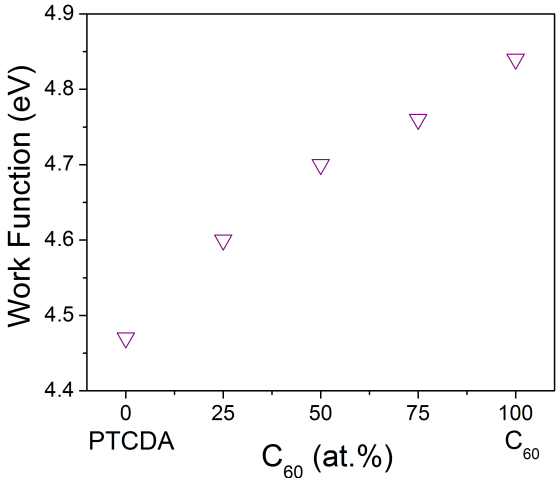

Figure 7.7. *Change in the work function in the PTCDA:C_{60} blends as extrapolated from UPS spectra. Values were measured and extrapolated by Brian J. Worfolk.*

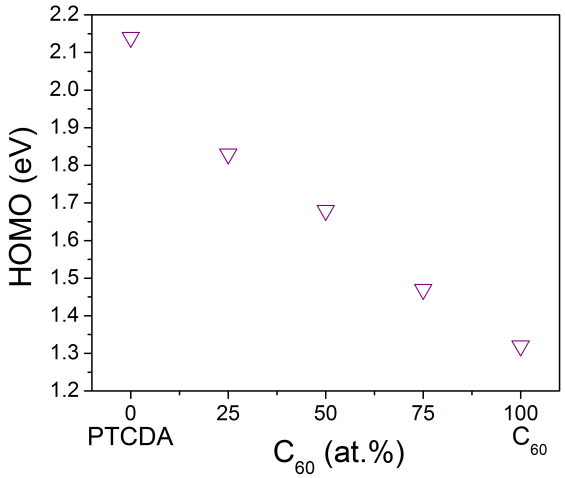

Figure 7.8. *Change in the HOMO level relative to the Fermi level of ITO in the PTCDA:C_{60} as extrapolated from UPS spectra. Values were measured and extrapolated by Brian J. Worfolk.*

A similar explanation could describe the shifting of the HOMO level as well. Figure 7.5 c shows a change for the HOMO level with increasing C_{60} content. This effect is more explicitly shown in Figure 7.8. It is unlikely for the HOMO of each individual molecule to change, since the electronic interactions between PTCDA and C_{60} are likely very weak. Similarly to the discussion for the shift in the work function, additional states states could occur near the onset of the HOMO peak from extrinsic effects such as structural defects. These additional states could seemingly shift the HOMO level as they could overlap with the actual HOMO states. Another possible explanation might be a superposition of the individual PTCDA and C_{60} HOMO levels, since the electronic states in each material are likely Gaussian distributed with individual FWHM [85].

Acceptor materials are lacking in versatility and therefore most commonly C_{60} is used. For metal-organic semiconductor interfaces in particular, these

results demonstrate improved choice for development of an efficient electronic architecture for OPVs. However, further investigation into the reasons for the shifts in work function and HOMO at the ITO/acceptor interface would be required. In particular, the measurement error has to be quantified in order to determine how much of the shift in work function and HOMO level is due to a physical effect and how much can be attributed to measurement error.

7.6 Organic Field Effect Transistors Based on PTCDA:C_{60} Acceptor Blends

OFETs were fabricated with the studied acceptor blend combinations of PTCDA and C_{60}. Figure 7.9 shows the fabricated OFET architecture and measurement setup.

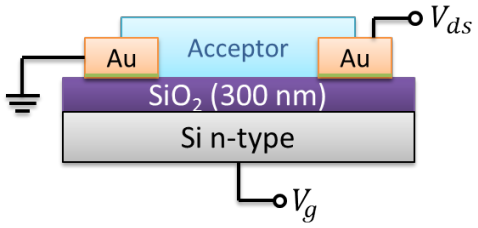

Figure 7.9. *The fabricated OFET architecture with* 50 *nm thick polycrystalline Au electrodes deposited on a* 300 *nm thick* SiO_2 *layer which acts as dielectric. For adhesion,* 2 *nm of Cr were used between the* SiO_2 *and the Au electrodes. For the characterization of the acceptors planar films are used. Gate voltage was applied from the bottom of the Si wafer. Drain voltage was applied at the source electrode. The drain electrode was connected to the ground and acts as common electrode for gate and drain voltage.*

For source and drain electrodes 50 *nm* of polycrystalline gold were used. Polycrystalline gold contacts are well understood in the literature and Figure 7.10 shows the electronic level diagrams for a Au/PTCDA junction [209–212]

and Au/C_{60} junction [183, 205, 206] based on previously measured results. Due to the high work function of Au, it has been shown that the Au/PTCDA interface [209–212] and Au/C_{60} interface [183,205,206] can form Ohmic contacts due to Fermi level pinning. This reduction in contact resistance can be useful for studying the mobility of our films using OFETs, since the contact resistance is expected to be low and negligible. Another aspect of this design, is that Au electrodes behave similarly for PTCDA as well as C_{60} which is suitable in the case when both molecules are blended together.

When comparing the literature values in Figure 7.10 for PTCDA and C_{60} on Au with the measured values in Figure 7.6 for both acceptors on ITO, slight differences become obvious. The surface dipole is expected to change when changing substrates. Ionization potential of the solid film on a different contact can slightly change also [210], however the change from 6.16 eV for C_{60} on ITO to 6.75 eV for C_{60} on Au is significant. As previously mentioned, this might be attributed to surface contamination on the C_{60} sample.

Nevertheless, the fabrication and the testing of OFETs was very challenging with our equipment. The SiO_2 surface treatment with OTS as described in the experimental chapter is crucial. Without OTS as self-assembled monolayers no working transistors could be fabricated. In addition, the probe station available could only measure in ambient air conditions. Pure C_{60} OFETs are reported to dramatically lose performance when operated in air [88]. In the device series, no working transistors could be achieved with a C_{60} content higher than 50 at.%. With increased C_{60} in the blend the device fabrication yield decreased significantly. Nevertheless, the results obtained with a majority content of PTCDA have provided us with some insights on OFET operation with these acceptor blends as well as mobility data.

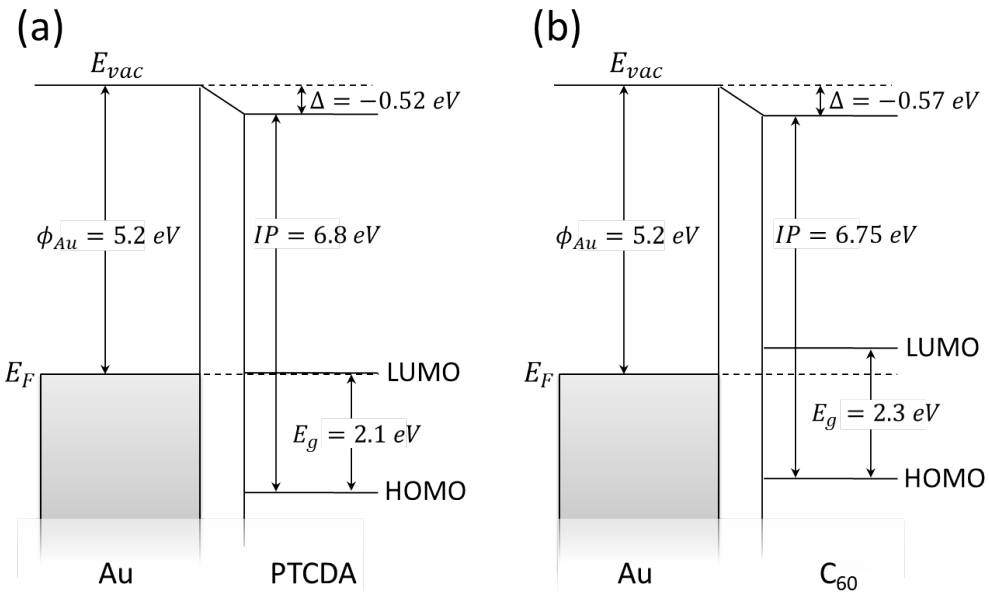

Figure 7.10. *Electronic level diagrams for the (a) Au/PTCDA and (b) Au/C_{60} junction. The ionization potential IP, the work function of the Au Φ_{Au}, the electronic band gap E_g, and interface dipole Δ are indicated. The values were extracted from [210] for the PTCDA, from [205] for C_{60}, and from [213] for the polycrystalline Au work function.*

7.6.1 OFETs Based on Pure PTCDA

Figure 7.11 shows drain current characteristics for a PTCDA only device with a channel width of 2000 μm and a channel length of 5 μm. For the $I_{ds} - V_{ds}$ graph, little to no drain current is measured for $V_{gs} = 0\ V$, however a strong current increase is observed starting from $V_{gs} = 20\ V$ and dependent on the gate voltage. Thus, a gate effect has been observed in the device. The high gate and drain voltage of up to 100 V is also reported for similar devices [214, 215]. However, in comparison to those reported results, an exponential current increase is observed for drain voltages above 50 V. This exponential increase could be an indication for approaching the breakdown voltage of the device.

Similar curves are observed when changing the channel dimensions to a

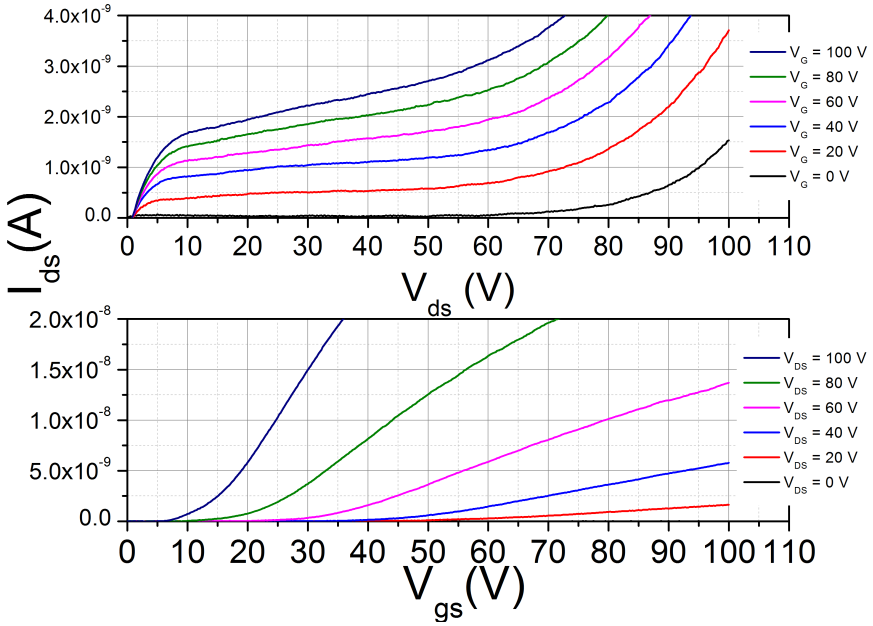

Figure 7.11. *Drain current characteristics for a Au/PTCDA/Au OFET with a channel width of* 2000 μm *and a channel length of* 5 μm*. For the* $I_{ds} - V_{ds}$ *graph the gate voltage* V_{gs} *is increased from* 0 *to* 100 V *in* 20 V *steps. Similarly, for the* $I_{ds} - V_{gs}$ *graph the drain voltage* V_{ds} *is increased from* 0 *to* 100 V *in* 20 V *steps.*

width of 1000 μm and a channel length of 10 μm, as shown in Figure 7.12. The curves have similar shape, however breakdown occurs at slightly higher voltages than in the previously shown device. For this reason, the saturation regime is more expressed. The drain current in that saturation regime is about half of the drain current for the device with the shorter channel length of 5 μm. This is a strong indication that contact resistance could play a role in these devices. For a qualitative discussion, Equation 7.3 from chapter 2 is used:

$$R_{tot} = R_{channel}^{sheet} \frac{L}{W} + R_{contact} \frac{1}{W} \tag{7.3}$$

where contact resistance is inversely proportional to the channel width.

In this device the channel width is half of the previous device, hence contact resistance could be twice as large. However, since contacts are assumed to be Ohmic, the half decrease in drain current can more likely be attributed to the sheet resistance which is proportional to the channel length.

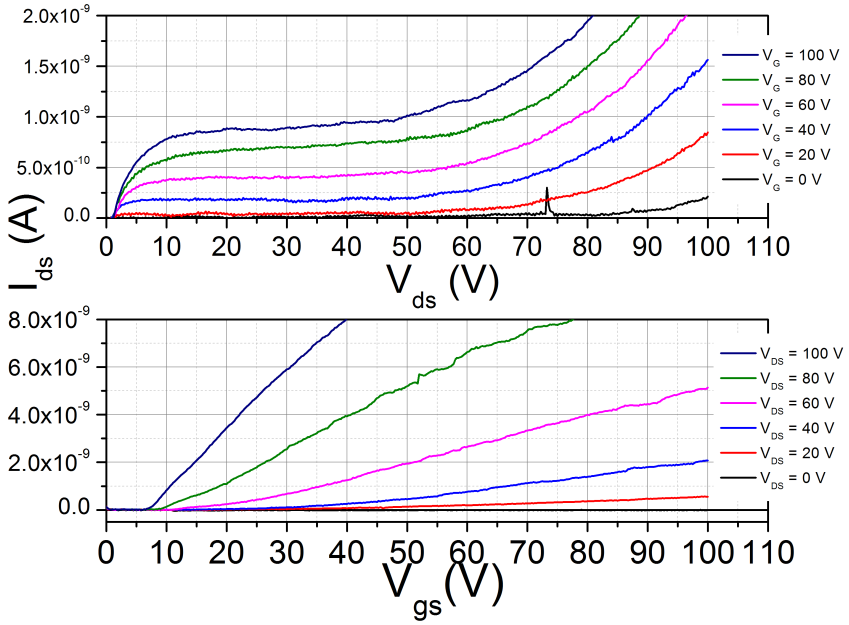

Figure 7.12. *Drain current characteristics for a Au/PTCDA/Au OFET with a channel width of* 1000 μm *and a channel length of* 10 μm*. For the* $I_{ds} - V_{ds}$ *graph the gate voltage* V_{gs} *is increased from* 0 *to* 100 V *in* 20 V *steps. Similarly, for the* $I_{ds} - V_{gs}$ *graph the drain voltage* V_{ds} *is increased from* 0 *to* 100 V *in* 20 V *steps.*

In the third case (as shown in Figure 7.13), an Au/PTCDA/Au transistor is observed with the same channel length of 10 μm and a channel width of 2000 μm. The onset for the breakdown current appears to occur at very low drain voltages close to 0 V. This early breakdown onset overlaps with the saturation regime of the $I_{ds} - V_{ds}$ curve.

When determining the electron mobility from all three channel geometries an average mobility of $6 \times 10^{-5}\ cm\, V^{-1}\, s^{-1}$ was observed for the PTCDA

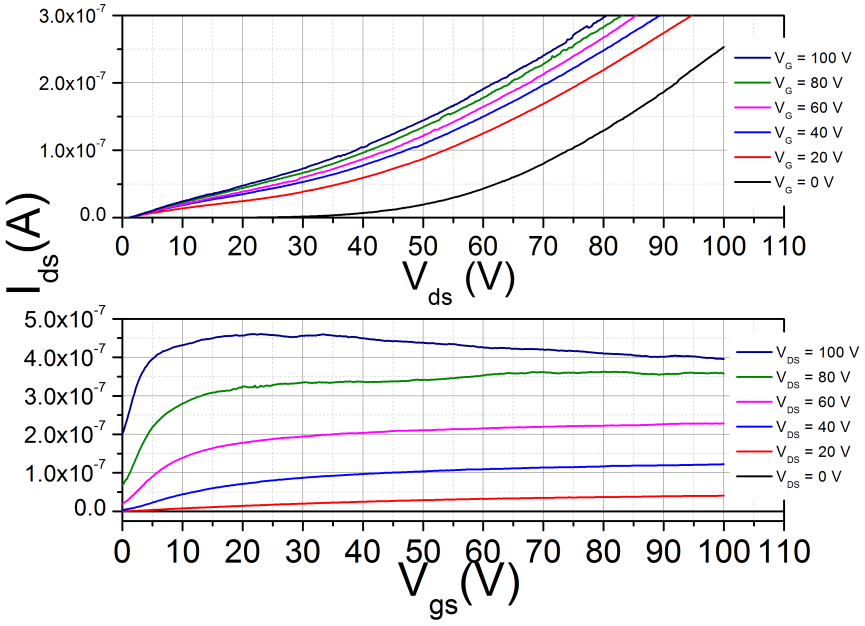

Figure 7.13. *Drain current characteristics for a Au/PTCDA/Au OFET with a channel width of* 2000 *µm and a channel length of* 10 *µm. For the* $I_{ds} - V_{ds}$ *graph the gate voltage* V_{gs} *is increased from* 0 *to* 100 *V in* 20 *V steps. Similarly, for the* $I_{ds} - V_{gs}$ *graph the drain voltage* V_{ds} *is increased from* 0 *to* 100 *V in* 20 *V steps.*

only OFETs which fits well into the previously reported range of 10^{-5} $cm\,V^{-1}\,s^{-1}$ to 10^{-4} $cm\,V^{-1}\,s^{-1}$ [54, 87, 215]. In order to achieve mobilities an order of magnitude higher, substrate heating could be employed during deposition in order to improve PTCDA crystallinity. Another approach might be to use a top-contact, top-gate OFET architecture which commonly has less extrinsic contact resistance, since voids can occur during the deposition of the organic film between the film and the contact [150, 216]. Both of those routes to improvement were not accessible to us at this point, as our organic GLAD system is not equipped with substrate heating since a low surface diffusion and thus a cold substrate is beneficial for GLAD structuring. In addition, the combination of various shadow masks with micrometer features needed to

build top-contact, top-gate devices might be an approach for future work.

7.6.2 OFETs Based on Pure C_{60}

When fabricating OFETs based on C_{60} and analyzing those devices in the probe station in ambient air, no transistor behavior could be observed. Several experiments were performed to fabricate those devices, in each experiment a minimum of two OFET chips with 6 devices each were characterized, yet no transistor results were achieved. A typical result is shown in Figure 7.14. In the $I_{ds} - V_{ds}$ graph no increase of drain current with increasing voltage was observed which is characteristic for the behavior of an insulator. Similarly, the $I_{ds} - V_{gs}$ curve does not indicated field effect behavior.

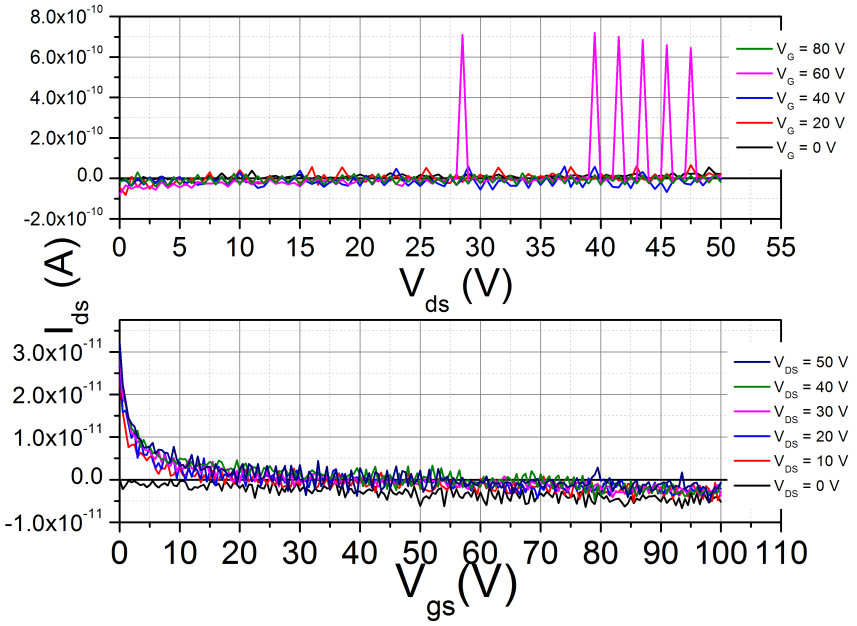

Figure 7.14. *Drain current characteristics for a Au/C_{60}/Au OFET with a channel width of* 2000 *µm and a channel length of* 5 *µm. For the $I_{ds} - V_{ds}$ graph the gate voltage V_{gs} is increased from* 0 *to* 100 *V in* 20 *V steps. Similarly, for the $I_{ds} - V_{gs}$ graph the drain voltage V_{ds} is increased from* 0 *to* 100 *V in* 20 *V steps.*

Again the shortcomings of C_{60} are observed here. Previous reports have described that oxygen molecules could act as traps for charge carriers in the C_{60} film [88, 217, 218]. Anticipating those challenges, special care was taken to keep the fabricated devices in an inert atmosphere container for transport and measuring the devices immediately after fabrication. Not withstanding this, a gate effect could not be observed.

In many other reports, substrate heating is used to deposit C_{60} films for OFETs, which could improve these devices as well [156, 158, 219]. However, since only insulating behavior was observed, the challenges lie probably with the exposure to ambient air. One way to reduce this exposure might be the use of a top-contact, top-gate architecture which could possibly help to encapsulate the C_{60} in the dielectric and thus shield it from its surrounding atmosphere.

7.6.3 OFETs Based on PTCDA:C_{60} Blends

For OFETs build with PTCDA:C_{60} blends no successful devices could be fabricated either and two examples for blended OFETs are presented in this section. Figure 7.15 shows a commonly observed result for PTCDA OFETs with an added C_{60} content of 25 $at.\%$. The device shown has a channel length of 5 μm and a channel width of 2000 μm, the same geometry as used in Figure 7.11 for the PTCDA only device.

These devices had to be run with much lower source-drain voltage, since the breakdown voltage was observed to be significantly lower than for PTCDA only. All of the $I_{ds} - V_{ds}$ curves have shown an exponential increase, similar to a metal-insulator-metal (MIM) model [19, 54, 58] which is also used to describe the diode behavior of an OPV in the dark. The drain currents are an order of magnitude higher than for the PTCDA only device. Assuming that the

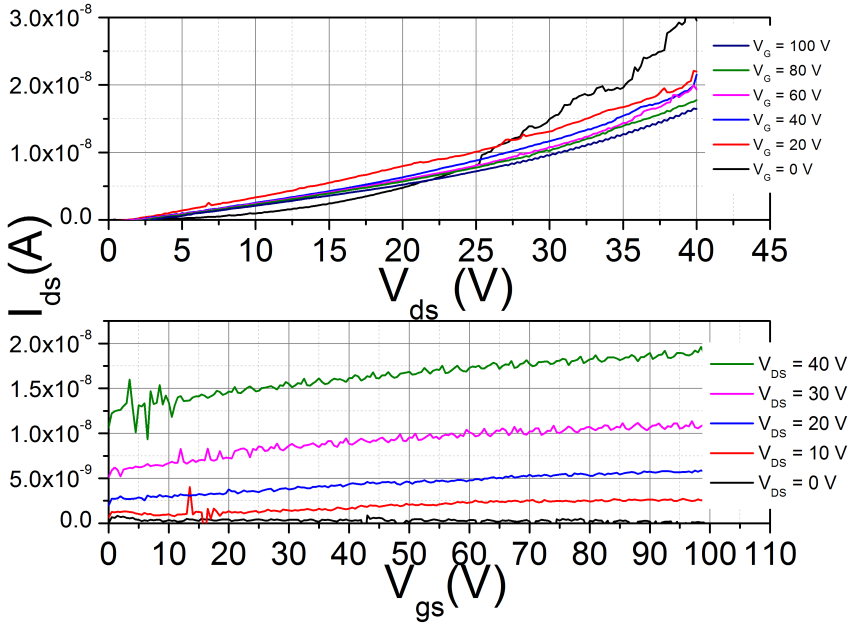

Figure 7.15. *Drain current characteristics for a Au/PTCDA(75):C_{60}(25)/Au OFET with a channel width of* 2000 *µm and a channel length of* 5 *µm. For the $I_{ds} - V_{ds}$ graph the gate voltage V_{gs} is increased from* 0 *to* 100 *V in* 20 *V steps. Similarly, for the $I_{ds} - V_{gs}$ graph the drain voltage V_{ds} is increased from* 0 *to* 50 *V in* 10 *V steps. Device breakdown however occurred at higher V_{ds} for which curves are not shown.*

device breakdown was reached too early and that there might be a transistor behavior for much lower drain voltages, fresh devices were run at much lower $V_{ds} \leq 10\ V$. However, still a similar behavior was observed. Since the $I_{ds} - V_{gs}$ curves show a very slight monotonic increase with increasing gate voltage and also some of the $I_{ds} - V_{ds}$ curves are shifted to slightly higher drain currents with higher V_{gs}, some effect of applying a gate voltage is measured. However, no clear triode and saturation regime can be derived. For that reason, one could speculate that the gate voltage has an influence on the injection of charge carriers at the contacts. While the device still behaves as a diode and no opening channel is observed, the gate voltage might help the molecular orbitals to better align with the Au contact's Fermi level and thus

slightly improve contact resistance. However, this explanation is speculative and would need further investigation, since at the beginning of the chapter it was shown that contact resistance is expected to be low and injection Ohmic.

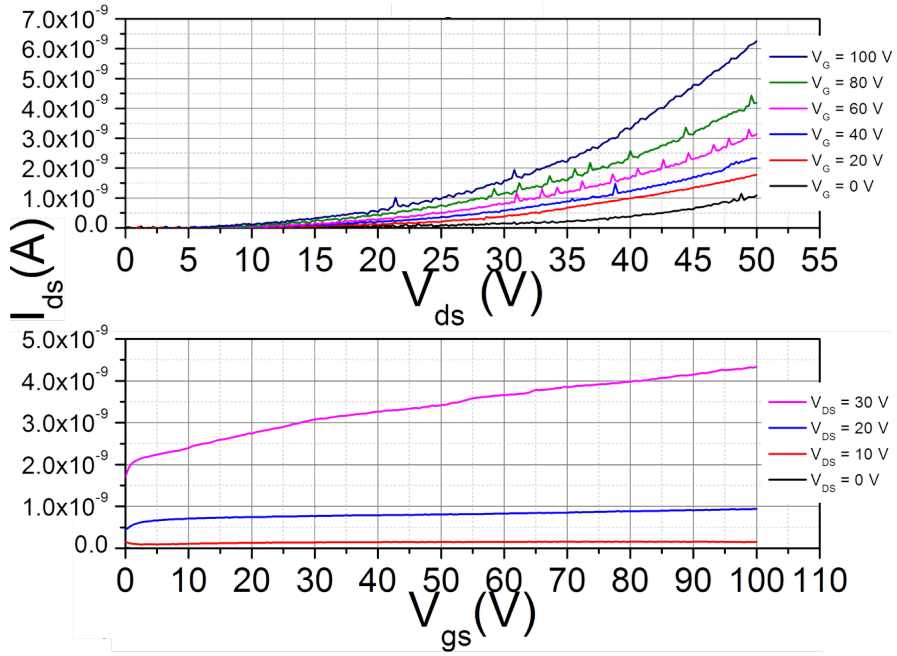

Figure 7.16. *Drain current characteristics for a Au/PTCDA(50):C_{60}(50)/Au OFET with a channel width of* 2000 μm *and a channel length of* 5 μm*. For the* $I_{ds} - V_{ds}$ *graph the gate voltage* V_{gs} *is increased from* 0 *to* 100 V *in* 20 V *steps. Similarly, for the* $I_{ds} - V_{gs}$ *graph the drain voltage* V_{ds} *is increased from* 0 *to* 50 V *in* 10 V *steps. Device breakdown however occurred at higher* V_{ds} *for which curves are not shown.*

The OFET devices based on a 50 : 50 ratio of PTCDA and C_{60}, as shown in Figure 7.16 for devices with the channel length of 5 μm and a channel width of 2000 μm, describes a similar behavior to the previously discussed blend. Breakdown voltages were observed at lower values compared to the PTCDA-only device. However, drain currents are lower than for the 75:25 case, and a higher C_{60} content could be associated with more defects in the PTCDA lattice.

For all of the devices using C_{60} air exposure can limit or destroy per-

formance, however, this effect might be less pronounced in the PTCDA:C_{60} blends where the C_{60} content would be encapsulated in a matrix of PTCDA. The exact state of the crystal structure is not understood as the Xray diffraction measurements have not shown a crystallinity for PTCDA:C_{60} as a blend and thus whether the molecules arrange as a perfect blend or domains are formed could not be determined. The blending of the two acceptors would likely lead to structural defects and could therefore generate a high amount of electronic trap states compared to a pure material. This could be an additional cause for poor charge transport [84], beside the air contamination of the C_{60} content.

It becomes obvious from the OFET experiments that adding major defects to a lattice by blending C_{60} into PTCDA does not seem to improve but rather significantly decreases the electronic transport properties. Although further research in better improvements in device manufacturing such as adding heat to the substrate during deposition might prove otherwise, at this point an improvement of blending acceptors to fabricate inverted OPVs cannot be expected.

7.7 Summary

In this preliminary study it was attempted to modify the acceptor material in order to find a concept to build better GLAD-structured OPVs. PTCDA and blends of PTCDA:C_{60} were successfully structured using GLAD. In addition, it was shown that those GLAD structures are probably stable against non-polar organic solvents, such as DCB. When combining PTCDA and C_{60} in blended films, the overall absorbance spectrum could be controlled by controlling the composition of both molecules. In addition, UPS results have

shown that the overall work function and overall HOMO level can change in the film, dependent on PTCDA:C_{60} composition.

These results suggest that the acceptor blends might be favorably incorporated into inverted OPVs. However, our OFET fabrication and characterization attempts have shown when blending both materials MIM behavior was observed and no charge accumulation due to an applied gate voltage could be shown. This is a strong indication that blending of both acceptor materials might decrease charge transport through the acceptor film and thus a favorable application of these acceptor blends in OPVs is unlikely. For this reason, this approach has not been further pursued and no inverted OPV devices were fabricated.

If this fabrication route was to be pursued in further research work, a different acceptor combination with PTCDA replaced with a higher mobility material might yield better results. In addition, substrate heating during deposition, as applied by many research groups to fabricate OFETs might decrease probable structural defects in the acceptor films. In this case however, this approach might not be suitable for GLAD since low surface diffusion and therefore little to no substrate heating is more favorable to build nanostructures. Lastly, using a top-contact transistor architecture instead of bottom contacts could enable encapsulation of the organic films, avoiding air exposure of C_{60}. In particular, a top-contact with a top-gate architecture is generally more favorable to bottom-contacts as the top-contact structure is known to have an improved contact resistance [74, 150, 216].

CHAPTER 8

CONCLUSIONS AND FUTURE RESEARCH

8.1 Morphology Engineering for OPVs

In the initial part of this thesis GLAD structuring of C_{60} films is investigated. Nanocolumnar morphologies were successfully achieved and the GLAD apparatus allowed for the control of film thickness and intercolumn spacing. In order to eliminate competitive shadowing and to alter the diameter of the C_{60} nanocolumns, ϕ-sweep motion control was successfully employed. The GLAD C_{60} films exhibited polycrystalline growth on glass/ITO substrates.

As described in chapter 4, GLAD provided a broad space of options for morphology engineering of OPVs without a need for more complex patterning methods such as photolithography. The the control of intercolumn spacing of the acceptor is a crucial parameter for inverted OPV design and this could be achieved by adjusting the substrate angle during deposition. Thus, GLAD provides a possible approach for the nanostructuring of OPVs.

8.2 OPV Device Performance

The investigated nanocolumnar C_{60} morphologies were applied to the fabrication of OPVs. A major challenge was to find a process solvent which can dissolve a donor material but would leave the GLAD C_{60} morphologies intact. A combination of dimethyl-sulfoxide as process solvent together with P3CBT as donor polymer was found. However, the filling process through spin-coating of P3CBT resulted in voids when being filled into the GLAD structured C_{60} films.

Nevertheless, the goal to investigate the effect of morphology engineering on device performance was successfully met. Three main morphologies were compared: planar devices, bulk heterojunctions, and GLAD structured devices. The morphology engineering in the GLAD devices did significantly improve OPV performance over the conventional structuring methods such as planar devices or bulk heterojunctions. A fourfold increase in PCE between a planar device and the GLAD device at $\alpha = 75^\circ$ as well as a twofold increase in PCE between an optimized bulk heterojunction and the same GLAD device architecture was observed and could be attributed to the GLAD structuring. In particular, intercolumn spacing played an important role for exciton harvesting. For a wide intercolumn spacing a lower number of excitons would diffuse to the heterointerface, while a short intercolumn spacing could lead to more voids in the donor filling and thus reduce the active heterointerface area. The donor filling into the GLAD C_{60} structures improved when employing a combination of acetone as process solvent and the 3-Q star molecule as donor. In addition, a similar trend was observed where GLAD structured devices significantly outperformed optimized planar morphologies and bulk heterojunction cells.

A major limiting factor for device performance, however, are the used solvent-donor combinations of DMSO with P3CBT and acetone with 3-Q, since with these materials state-of-the-art performances could not be reached. While GLAD structuring clearly improves device efficiency when using the same materials over planar devices and bulk heterojunctions, finding a better solvent-donor combination could potentially yield better results.

8.3 Acceptor Blends and OFETs

The biggest of the challenges presented in this work was the dissolution of GLAD C_{60} films in conventionally used non-polar solvents such as CB, DCB or chloroform, which does not allow use of state-of-the-art low bandgap polymers. Instead of adapting the donor material to the solvent and to test for compatibility with GLAD structured C_{60} films, the acceptor was changed directly. The co-deposition of two acceptor materials was not widely researched to date and could be a strong niche for GLAD structured acceptor films.

A series of PTCDA:C_{60} blends was investigated where 25 *at*.% of C_{60} was incrementally added to PTCDA. By blending PTCDA together with C_{60}, an acceptor combination was found which could successfully be GLAD structured. In addition, this acceptor morphology remained stable after spin-coating with DCB, one of the most widely used solvent for low bandgap polymers. The absorption spectra of both materials complemented each other as C_{60} is more absorbing in the near UV wavelengths while PTCDA absorbs more light in the red. The blending of both materials enabled a useful combination of these absorption ranges. Measuring the blended films by UPS has shown that with changing PTCDA:C_{60} composition the overall HOMO

level as well as the overall work function of the overall acceptor blend films shifted. Interfacial layers between electrode and photoactive layer in OPVs are widely researched, and a tuning in work function might allow new avenues for OPV performance improvement.

While a PTCDA transistor with comparable device performance to previously reported results in the literature could be fabricated, no C_{60} OFETs were successfully made. This could be attributed to the air exposure of the C_{60} OFET devices. Further, when using the acceptor blends in OFETs, no charge accumulation due to a gate-effect was observed. The drain current characteristics were indicative for a change of charge injection with increasing gate voltage, however no transistor behavior could be measured.

Hence, while the blending of PTCDA and C_{60} seemed to be a strong approach at first with significant benefits such as morphology stability in non-polar organic solvents, charge mobility is likely lower due to the acceptor blending. This unfortunately indicates that the approach of acceptor blending using PTCDA:C_{60} is not yet suitable for use in inverted OPVs.

8.4 Future Work

For further research, more regular morphologies could be investigated such as a "chess board" patterned distribution of nanocolumns on the substrate. This could be achieved by using a periodic pattern of film growth seeds. Similar approaches were previously successful with the patterning of GLAD structured silicon films [220]. Since one of the main motivations for OPV fabrication is a lower cost per power output compared with competing PV technologies, the patterning of the substrate would have to become cheaper. Thus, methods such as nanoimprint lithography or self-assembly could be

employed for an inexpensive substrate patterning of periodicly distributed seeds.

The OPV results for GLAD structured OPVs are promising, particularly if a solvent-donor combination could be found which would allow use of the best performing low bandgap polymers used in the champion OPV devices today, thus further improving performance. The GLAD structured devices exhibited a PCE up to twice as high as in bulk heterojunctions. Commonly used low bandgap polymer OPVs achieve about 5% PCE in inverted OPVs. If these polymers could be used in GLAD structured inverted OPVs, device efficiency could possibly further increase.

Reduction in device performance due to air contamination or exposure was a significant challenge when using C_{60} films. There are two fabrication routes in order to minimize exposure to air. One approach is to deposit the acceptor and donor without breaking vacuum in one process chamber. This approach has been avoided in this work due to challenges in filling the nanostructured GLAD C_{60} films with an evaporated donor. Advanced substrate motion control could be investigated in order to better fill a nanocolumnar film. Another approach to minimize exposure to air is to use an integrated fabrication assembly which connects a process chamber for GLAD evaporation together with a glovebox in which spin-coating and electronic characterization can be performed. This way devices would entirely be fabricated in inert atmosphere. This state of the art fabrication approach is currently pursued in our research group, and an integrated glovebox is under construction.

Although the approach using PTCDA:C_{60} blends was not entirely successful, this direction could nevertheless be further investigated. In particular, other material combinations might be more suitable. Another route is

to use one different acceptor material altogether. GLAD is very successful at nanostructuring materials which can be evaporated. This broad versatility of GLAD will allow for new solutions based on new morphologies, device architectures, and materials choices in OPVs.

REFERENCES

[1] Frost & Sullivan, "Global Solar Power Markets," tech. rep., 2009.

[2] Frost & Sullivan, "Third Generation Photovoltaics: Strategic R & D Portfolio Management (Technical Insights)," tech. rep., 2010.

[3] NanoMarkets LC, "Thin-Film, Organic, and Printable Photovoltaic Markets: 2007-2015," tech. rep., 2007.

[4] NanoMarkets LC, "Organic Photovoltaic Markets," tech. rep., 2008.

[5] T. D. Nielsen, C. Cruickshank, S. Foged, J. Thorsen, and F. C. Krebs, "Business, market and intellectual property analysis of polymer solar cells," *Solar Energy Materials and Solar Cells*, vol. 94, pp. 1553–1571, Oct. 2010.

[6] C. W. Tang, "Two-layer organic photovoltaic cell," *Applied Physics Letters*, vol. 48, no. 2, p. 183, 1986.

[7] N. S. Sariciftci, L. Smilowitz, A. J. Heeger, and F. Wudl, "Photoinduced electron transfer from a conducting polymer to buckminsterfullerene.," *Science (New York, N.Y.)*, vol. 258, pp. 1474–1476, Nov. 1992.

[8] J. J. M. Halls, C. A. Walsh, N. C. Greenham, E. A. Marseglia, R. H. Friend, S. C. Moratti, and A. B. Holmes, "Efficient photodiodes from interpenetrating polymer networks," *Nature*, vol. 376, pp. 498–500, Aug. 1995.

[9] S. E. Shaheen, C. J. Brabec, N. S. Sariciftci, F. Padinger, T. Fromherz, and J. C. Hummelen, "2.5% efficient organic plastic solar cells," *Applied Physics Letters*, vol. 78, no. 6, pp. 841–843, 2001.

[10] J. Xue, S. Uchida, B. P. Rand, and S. R. Forrest, "Asymmetric tandem organic photovoltaic cells with hybrid planar-mixed molecular heterojunctions," *Applied Physics Letters*, vol. 85, no. 23, p. 5757, 2004.

[11] K. M. Coakley and M. D. McGehee, "Conjugated Polymer Photovoltaic Cells," *Chemistry of Materials*, vol. 16, pp. 4533–4542, Nov. 2004.

[12] H. Spanggaard and F. C. Krebs, "A brief history of the development of organic and polymeric photovoltaics," *Solar Energy Materials and Solar Cells*, vol. 83, pp. 125–146, June 2004.

[13] J. Roncali, "Linear π-conjugated systems derivatized with C_{60}-fullerene as molecular heterojunctions for organic photovoltaics," *Chemical Society Reviews*, vol. 34, no. 6, pp. 483–495, 2005.

[14] S. E. Gledhill, B. Scott, and B. A. Gregg, "Organic and nano-structured composite photovoltaics: An overview," *Journal of Materials Research*, vol. 20, pp. 3167–3179, Mar. 2005.

[15] P. Blom, V. Mihailetchi, L. Koster, and D. Markov, "Device Physics of Polymer:Fullerene Bulk Heterojunction Solar Cells," *Advanced Materials*, vol. 19, pp. 1551–1566, June 2007.

[16] C. Lungenschmied, G. Dennler, H. Neugebauer, N. S. Sariciftci, M. Glatthaar, and T. Meyer, "Flexible, long-lived, large-area, organic solar cells," *Solar Energy Materials and Solar Cells*, vol. 91, pp. 379–384, Mar. 2007.

[17] B. R. Saunders and M. L. Turner, "Nanoparticle-polymer photovoltaic cells.," *Advances in Colloid and Interface Science*, vol. 138, pp. 1–23, Apr. 2008.

[18] B. C. Thompson and J. M. J. Fréchet, "Polymer-fullerene composite solar cells.," *Angewandte Chemie (International ed. in English)*, vol. 47, pp. 58–77, Jan. 2008.

[19] M. C. Scharber, D. Mühlbacher, M. Koppe, P. Denk, C. Waldauf, A. J. Heeger, and C. J. Brabec, "Design Rules for Donors in Bulk-Heterojunction Solar Cells - Towards 10 % Energy-Conversion Efficiency," *Advanced Materials*, vol. 18, pp. 789–794, Mar. 2006.

[20] S. E. Gledhill, B. Scott, and B. A. Gregg, "Organic and nano-structured composite photovoltaics: An overview," *Journal of Materials Research*, vol. 20, pp. 3167–3179, Mar. 2011.

[21] H.-Y. Chen, J. Hou, S. Zhang, Y. Liang, G. Yang, Y. Yang, L. Yu, Y. Wu, and G. Li, "Polymer solar cells with enhanced open-circuit voltage and efficiency," *Nature Photonics*, vol. 3, pp. 649–653, Oct. 2009.

[22] P. Peumans, A. Yakimov, and S. R. Forrest, "Small molecular weight organic thin-film photodetectors and solar cells," *Journal of Applied Physics*, vol. 93, pp. 3693–3723, Apr. 2003.

[23] J. Xue, B. P. Rand, S. Uchida, and S. R. Forrest, "A Hybrid Planar-Mixed Molecular Heterojunction Photovoltaic Cell," *Advanced Materials*, vol. 17, pp. 66–71, Jan. 2005.

[24] F. Yang and S. R. Forrest, "Photocurrent generation in nanostructured organic solar cells," *ACS nano*, vol. 2, pp. 1022–1032, May 2008.

[25] K. Robbie, M. J. Brett, and A. Lakhtakia, "Chiral sculptured thin films," *Nature*, vol. 384, pp. 616–616, Dec. 1996.

[26] M. M. Hawkeye and M. J. Brett, "Glancing angle deposition: Fabrication, properties, and applications of micro- and nanostructured thin films," *Journal of Vacuum Science & Technology A: Vacuum, Surfaces, and Films*, vol. 25, no. 5, pp. 1317–1335, 2007.

[27] J. S. Kim, Y. Park, D. Y. Lee, J. H. Lee, J. H. Park, J. K. Kim, and K. Cho, "Poly(3-hexylthiophene) Nanorods with Aligned Chain Orientation for Organic Photovoltaics," *Advanced Functional Materials*, vol. 20, pp. 540–545, Feb. 2010.

[28] W. Ma, C. Yang, X. Gong, K. Lee, and A. J. Heeger, "Thermally Stable, Efficient Polymer Solar Cells with Nanoscale Control of the Interpenetrating Network Morphology," *Advanced Functional Materials*, vol. 15, pp. 1617–1622, Oct. 2005.

[29] M. Thomas, B. J. Worfolk, D. A. Rider, M. T. Taschuk, J. M. Buriak, and M. J. Brett, "C_{60} fullerene nanocolumns–polythiophene heterojunctions for inverted organic photovoltaic cells.," *ACS Applied Materials & Interfaces*, vol. 3, pp. 1887–1894, June 2011.

[30] M. Thomas, W. Li, Z. Bo, and M. Brett, "Inverted photovoltaic cells of nanocolumnar C_{60} filled with solution processed small molecule 3-Q," *Organic Electronics*, vol. 13, pp. 2647–2652, Nov. 2012.

[31] M. Thomas, B. J. Worfolk, D. A. Rider, M. T. Taschuk, J. M. Buriak, and M. J. Brett, "Controlling C_{60} fullerene nanocolumn morphology for organic photovoltaic applications," in *2011 37th IEEE Photovoltaic Specialists Conference*, (Seattle), pp. 744–747, IEEE, June 2011.

[32] B. J. Worfolk, D. A. Rider, A. L. Elias, M. Thomas, K. D. Harris, and J. M. Buriak, "Bulk Heterojunction Organic Photovoltaics Based on Carboxylated Polythiophenes and PCBM on Glass and Plastic Substrates," *Advanced Functional Materials*, vol. 21, pp. 1816–1826, Apr. 2011.

[33] M. Ohring, *Materials Science of Thin Films*. Academic Press, 2nd ed., 2002.

[34] L. Maissel and R. Glang, *Handbook of Thin Film Technology*. 1970.

[35] H. Hertz, "Ueber die Verdunstung der Flüssigkeiten, insbesondere des Quecksilbers, im luftleeren Raume," *Annalen der Physik*, vol. 253, no. 10, pp. 177–193, 1882.

[36] M. Knudsen, "Die maximale Verdampfungsgeschwindigkeit des Quecksilbers," *Annalen der Physik*, vol. 352, no. 13, pp. 697–708, 1915.

[37] P. de Gennes, "Wetting: statics and dynamics," *Reviews of Modern Physics*, vol. 57, pp. 827–863, July 1985.

[38] T. Young, "An Essay on the Cohesion of Fluids," *Philosophical Transactions of the Royal Society of London*, vol. 95, pp. 65–87, Jan. 1805.

[39] B. A. Movchan and A. V. Demchishin, "No Title," *Physics of Metals and Metallography*, vol. 28, pp. 83–90, 1969.

[40] A. Kundt, "Über Doppelbrechung des Lichtes in Metallschichten, welche durch Zerstäuben einer Kathode hergestellt sind," *Annalen der Physik*, vol. 27, pp. 59–71, 1886.

[41] F. Kämpf, "Größe und Ursache der Doppelbrechung in Kundtschen Spiegeln und Erzeugung von Doppelbrechung in Metallspiegeln durch Zug," *Annalen der Physik*, vol. 26, pp. 308–333, 1905.

[42] C. Maurin, "Dirchroisme, birefringence et conductibilite de lames metalliques mince obtenues par pulverisation cathodique," *Comptes Rendus Hebdomaires des Seances de l'Academie des Sciences*, vol. 142, pp. 870–872, 1906.

[43] C. Bergholm, "Über Doppelbrechung in Kathodenzerstäubten Metallschichten," *Annalen der Physik*, vol. 43, pp. 1–23, 1914.

[44] N. O. Young and J. Kowal, "Optically Active Fluorite Films," *Nature*, vol. 183, pp. 104–105, Jan. 1959.

[45] M. T. Taschuk, M. M. Hawkeye, and M. J. Brett, "Glancing Angle Deposition," in *Handbook of Deposition Technologies for Films and Coatings: Science, Applications and Technology* (P. Martin, ed.), William Andrew Publishing, 3rd ed.

[46] J. M. Nieuwenhuizen and H. B. Haanstra, "Microfactography of Thin Films," *Philips Tech. Review*, vol. 27, pp. 87–91, 1966.

[47] A. G. Dirks and H. J. Leamy, "Columnar microstructure in vapor-deposited films," *Thin Solid Films*, vol. 47, pp. 219–233, 1977.

[48] S. Lichter and J. Chen, "Model for columnar microstructure of thin solid films," *Physical Review Letters*, vol. 56, pp. 1396–1399, 1986.

[49] P. Maekin, "Ballistic deposition onto inclined surfaces," *Physical Review A*, vol. 38, pp. 994–1004, 1988.

[50] R. N. Tait, T. Smy, and M. J. Brett, "Modelling and characterization of columnar growth in evaporated films," *Thin Solid Films*, vol. 226, pp. 196–201, Apr. 1993.

[51] B. Dick, M. J. Brett, and T. Smy, "Investigation of substrate rotation at glancing-incidence on thin-film morphology," *Journal of Vacuum Science & Technology B: Microelectronics and Nanometer Structures*, vol. 21, pp. 2569–2575, 2003.

[52] J. J. Steele and M. J. Brett, "Nanostructure engineering in porous columnar thin films: recent advances," *Journal of Materials Science: Materials in Electronics*, vol. 18, pp. 367–379, Oct. 2006.

[53] M. O. Jensen and M. J. Brett, "Porosity engineering in glancing angle deposition thin films," *Applied Physics A: Materials Science & Processing*, vol. 80, no. 4, pp. 763–768, 2005.

[54] C. Brabec, V. Dyanokov, J. Parisi, and N. S. Sariciftci, eds., *Organic photovoltaics : concepts and realization*. New York: Springer Series in Materials Science, 2003.

[55] N. E. R. . B. S. I. Center, "Solar Spectra."

[56] H. B. Serreze, H. M. Sobhie, and S. J. Hogan, "Solar Simulators - Beyond Class A," *2009 34th IEEE Photovoltaic Specialists Conference, Vols 1-3*, pp. 1665–1670, 2009.

[57] B. A. Gregg and M. C. Hanna, "Comparing organic to inorganic photovoltaic cells: Theory, experiment, and simulation," *Journal of Applied Physics*, vol. 93, no. 6, pp. 3605–3614, 2003.

[58] C. J. Brabec, A. Cravino, D. Meissner, N. S. Sariciftci, T. Fromherz, M. T. Rispens, L. Sanchez, and J. C. Hummelen, "Origin of the Open Circuit Voltage of Plastic Solar Cells," *Advanced Functional Materials*, vol. 11, pp. 374–380, Oct. 2001.

[59] H. Hoppe and N. S. Sariciftci, "Polymer Solar Cells," in *Photoresponsive Polymers II*, vol. 214 of *Advances in Polymer Science*, pp. 1–86, 2008.

[60] H. Ishii, K. Sugiyama, E. Ito, and K. Seki, "Energy Level Alignment and Interfacial Electronic Structures at Organic/Metal and Organic/Organic Interfaces," *Advanced Materials*, vol. 11, pp. 605–625, June 1999.

[61] S. R. Forrest, "The limits to organic photovoltaic cell efficiency," *MRS Bulletin*, vol. 30, no. 1, pp. 28–32, 2005.

[62] G. Li, V. Shrotriya, J. Huang, Y. Yao, T. Moriarty, K. Emery, and Y. Yang, "High-efficiency solution processable polymer photovoltaic cells by self-organization of polymer blends," *Nature Materials*, vol. 4, pp. 864–868, Oct. 2005.

[63] F. Yang, M. Shtein, and S. R. Forrest, "Controlled growth of a molecular bulk heterojunction photovoltaic cell," *Nature Materials*, vol. 4, pp. 37–41, Dec. 2004.

[64] M. D. Irwin, D. B. Buchholz, A. W. Hains, R. P. H. Chang, and T. J. Marks, "p-Type semiconducting nickel oxide as an efficiency-enhancing anode interfacial layer in polymer bulk-heterojunction solar cells," *Proceedings of the National Academy of Sciences*, vol. 105, pp. 2783–2787, Feb. 2008.

[65] J. Xue, S. Uchida, B. P. Rand, and S. R. Forrest, "4.2% efficient organic photovoltaic cells with low series resistances," *Applied Physics Letters*, vol. 84, no. 16, pp. 3013–3015, 2004.

[66] J. D. Servaites, S. Yeganeh, T. J. Marks, and M. A. Ratner, "Efficiency Enhancement in Organic Photovoltaic Cells: Consequences of Optimizing Series Resistance," *Advanced Functional Materials*, vol. 20, pp. 97–104, Jan. 2010.

[67] S. Dongaonkar, J. D. Servaites, G. M. Ford, S. Loser, J. Moore, R. M. Gelfand, H. Mohseni, H. W. Hillhouse, R. Agrawal, M. A. Ratner, T. J. Marks, M. S. Lundstrom, and M. A. Alam, "Universality of non-Ohmic shunt leakage in thin-film solar cells," *Journal of Applied Physics*, vol. 108, no. 12, p. 124509, 2010.

[68] M. Riede, T. Mueller, W. Tress, R. Schueppel, and K. Leo, "Small-molecule solar cells - status and perspectives," *Nanotechnology*, vol. 19, p. 424001, Oct. 2008.

[69] A. Facchetti, "π-Conjugated Polymers for Organic Electronics and Photovoltaic Cell Applications," *Chemistry of Materials*, vol. 23, pp. 733–758, Feb. 2011.

[70] A. Pron and P. Rannou, "Processible conjugated polymers: from organic semiconductors to organic metals and superconductors," *Progress in Polymer Science*, vol. 27, no. 1, pp. 135–190, 2002.

[71] Y. Kim, S. Cook, S. M. Tuladhar, S. A. Choulis, J. Nelson, J. R. Durrant, D. D. C. Bradley, M. Giles, I. McCulloch, C. S. Ha, and M. Ree,

"A strong regioregularity effect in self-organizing conjugated polymer films and high-efficiency polythiophene: fullerene solar cells," *Nature Materials*, vol. 5, no. 3, pp. 197–203, 2006.

[72] Y. Shen, A. R. Hosseini, M. H. Wong, and G. G. Malliaras, "How to make ohmic contacts to organic semiconductors.," *Chemphyschem : a European journal of chemical physics and physical chemistry*, vol. 5, pp. 16–25, Jan. 2004.

[73] S. M. Sze and K. K. Ng, *Physics of Semiconductor Devices*. John Wiley & Sons, Inc, 2006.

[74] Z. Bao and J. J. Locklin, *Organic Field-Effect Transistors*. CRC Press, 2007.

[75] A. Crispin, X. Crispin, M. Fahlman, M. Berggren, and W. R. Salaneck, "Transition between energy level alignment regimes at a low band gap polymer-electrode interfaces," *Applied Physics Letters*, vol. 89, no. 21, p. 213503, 2006.

[76] N. Koch and A. Vollmer, "Electrode-molecular semiconductor contacts: Work-function-dependent hole injection barriers versus Fermi-level pinning," *Applied Physics Letters*, vol. 89, no. 16, p. 162107, 2006.

[77] H. Fukagawa, S. Kera, T. Kataoka, S. Hosoumi, Y. Watanabe, K. Kudo, and N. Ueno, "The Role of the Ionization Potential in Vacuum-Level Alignment at Organic Semiconductor Interfaces," *Advanced Materials*, vol. 19, pp. 665–668, Mar. 2007.

[78] E. J. Meijer, A. V. G. Mangnus, C. M. Hart, D. M. de Leeuw, and T. M. Klapwijk, "Frequency behavior and the Mott-Schottky analysis in poly(3-hexyl thiophene) metal-insulator-semiconductor diodes," *Applied Physics Letters*, vol. 78, no. 24, p. 3902, 2001.

[79] R. Gupta, S. C. K. Misra, B. D. Malhotra, N. N. Beladakere, and S. Chandra, "Metal/semiconductive polymer Schottky device," *Applied Physics Letters*, vol. 58, no. 1, p. 51, 1991.

[80] P. Stallinga, H. Gomes, M. Murgia, and K. Müllen, "Interface state mapping in a Schottky barrier of the organic semiconductor terrylene," *Organic Electronics*, vol. 3, pp. 43–51, Mar. 2002.

[81] A. Pivrikas, N. S. Sariciftci, G. Juska, and R. Osterbacka, "A review of charge transport and recombination in polymer/fullerene organic solar cells," *Progress in Photovoltaics*, vol. 15, no. 8, pp. 677–696, 2007.

[82] H. Hoppe and N. S. Sariciftci, "Morphology of polymer/fullerene bulk heterojunction solar cells," *Journal of Materials Chemistry*, vol. 16, no. 1, pp. 45–61, 2006.

[83] J. R. Ostrick, A. Dodabalapur, L. Torsi, a. J. Lovinger, E. W. Kwock, T. M. Miller, M. Galvin, M. Berggren, and H. E. Katz, "Conductivity-type anisotropy in molecular solids," *Journal of Applied Physics*, vol. 81, no. 10, p. 6804, 1997.

[84] J. J. Kwiatkowski, J. M. Frost, and J. Nelson, "The effect of morphology on electron field-effect mobility in disordered C_{60} thin films.," *Nano Letters*, vol. 9, pp. 1085–1090, Mar. 2009.

[85] H. Bässler, "Charge Transport in Disordered Organic Photoconductors - A Monte-Carlo Simulation Study," *Physica Status Solidi B-Basic Research*, vol. 175, no. 1, pp. 15–56, 1993.

[86] C. J. Brabec, "Organic photovoltaics: technology and market," *Solar Energy Materials and Solar Cells*, vol. 83, no. 2-3, pp. 273–292, 2004.

[87] C. Dimitrakopoulos and P. Malenfant, "Organic Thin Film Transistors for Large Area Electronics," *Advanced Materials*, vol. 14, pp. 99–117, Jan. 2002.

[88] R. C. Haddon, A. S. Perel, R. C. Morris, T. T. M. Palstra, A. F. Hebard, and R. M. Fleming, "C_{60} Thin-Film Transistors," *Applied Physics Letters*, vol. 67, no. 1, pp. 121–123, 1995.

[89] J. Kastner, J. Paloheimo, and H. Kuzmany, *Solid State Sciences*. Berlin: Springer Verlag, 1993.

[90] Z. Bao, A. J. Lovinger, and J. Brown, "New Air-Stable n-Channel Organic Thin Film Transistors," vol. 7863, no. 23, pp. 207–208, 1998.

[91] J. Burroughes, C. Jones, and R. Friend, "New semiconductor device physics in polymer diodes and transistors," *Nature*, vol. 335, no. 6186, pp. 137–141, 1988.

[92] H. Sirringhaus, N. Tessler, and R. H. Friend, "Integrated Optoelectronic Devices Based on Conjugated Polymers," *Science*, vol. 280, pp. 1741–1744, June 1998.

[93] Y.-Y. Lin, D. Gundlach, S. Nelson, and T. Jackson, "Stacked pentacene layer organic thin-film transistors with improved characteristics," *IEEE Electron Device Letters*, vol. 18, pp. 606–608, Dec. 1997.

[94] N. R. E. Laboratory, "NREL Best Research-Cell Efficiencies Chart," 2012.

[95] J. Nelson, "Organic photovoltaic films," *Current Opinion in Solid State & Materials Science*, vol. 6, no. 1, pp. 87–95, 2002.

[96] V. Bulović, P. Burrows, S. Forrest, J. Cronin, and M. Thompson, "Study of localized and extended excitons in 3,4,9,10-perylenetetracarboxylic dianhydride (PTCDA) I. Spectroscopic properties of thin films and solutions," *Chemical Physics*, vol. 210, pp. 1–12, Oct. 1996.

[97] M. Hoffmann, K. Schmidt, T. Fritz, T. Hasche, V. Agranovich, and K. Leo, "The lowest energy Frenkel and charge-transfer excitons in quasi-one-dimensional structures: application to MePTCDI and PTCDA crystals," *Chemical Physics*, vol. 258, pp. 73–96, Aug. 2000.

[98] B. A. Gregg, "The photoconversion mechanism of excitonic solar cells," *MRS Bulletin*, vol. 30, no. 1, pp. 20–22, 2005.

[99] B. A. Gregg, "Excitonic Solar Cells," *The Journal of Physical Chemistry B*, vol. 107, pp. 4688–4698, May 2003.

[100] A. L. Fahrenbruch and R. H. Bube, *Fundamentals of Solar Cells. Photovoltaic Solar Energy Conversion*. 1983.

[101] A. Goetzberger, C. Hebling, and H. W. Schock, "Photovoltaic materials, history, status and outlook," *Materials Science & Engineering R-Reports*, vol. 40, no. 1, pp. 1–46, 2003.

[102] A. Morteani, P. Sreearunothai, L. Herz, R. Friend, and C. Silva, "Exciton Regeneration at Polymeric Semiconductor Heterojunctions," *Physical Review Letters*, vol. 92, June 2004.

[103] I.-W. Hwang, Q.-H. Xu, C. Soci, B. Chen, A. K.-Y. Jen, D. Moses, and A. J. Heeger, "Ultrafast Spectroscopic Study of Photoinduced Electron Transfer in an Oligo(thienylenevinylene):Fullerene Composite," *Advanced Functional Materials*, vol. 17, pp. 563–568, Mar. 2007.

[104] D. Veldman, O. Ipek, S. C. J. Meskers, J. Sweelssen, M. M. Koetse, S. C. Veenstra, J. M. Kroon, S. S. van Bavel, J. Loos, and R. A. J. Janssen, "Compositional and electric field dependence of the dissociation of charge transfer excitons in alternating polyfluorene copolymer/-fullerene blends.," *Journal of the American Chemical Society*, vol. 130, pp. 7721–7735, June 2008.

[105] S. Westenhoff, I. A. Howard, J. M. Hodgkiss, K. R. Kirov, H. A. Bronstein, C. K. Williams, N. C. Greenham, and R. H. Friend, "Charge recombination in organic photovoltaic devices with high open-circuit voltages.," *Journal of the American Chemical Society*, vol. 130, pp. 13653–8, Oct. 2008.

[106] J.-L. Brédas, J. E. Norton, J. Cornil, and V. Coropceanu, "Molecular understanding of organic solar cells: the challenges.," *Accounts of chemical research*, vol. 42, pp. 1691–1699, Nov. 2009.

[107] J. J. M. Halls, K. Pichler, R. H. Friend, S. C. Moratti, and A. B. Holmes, "Exciton diffusion and dissociation in a poly(p-phenylenevinylene)/C_{60} heterojunction photovoltaic cell," *Applied Physics Letters*, vol. 68, no. 22, pp. 3120–3122, 1996.

[108] P. Peumans, S. Uchida, and S. R. Forrest, "Efficient bulk heterojunction photovoltaic cells using small-molecular-weight organic thin films.," *Nature*, vol. 425, pp. 158–162, Sept. 2003.

[109] A. L. Briseno, T. W. Holcombe, A. I. Boukai, E. C. Garnett, S. W. Shelton, J. J. M. Fréchet, and P. Yang, "Oligo- and polythiophene/ZnO hybrid nanowire solar cells.," *Nano Letters*, vol. 10, pp. 334–340, Jan. 2010.

[110] L. Chen, K. Yao, and Y. Chen, "Can morphology tailoring based on functionalized fullerene nanostructures improve the performance of organic solar cells?," *Journal of Materials Chemistry*, vol. 22, no. 36, p. 18768, 2012.

[111] D. Gebeyehu, C. J. Brabec, F. Padinger, T. Fromherz, J. C. Hummelen, D. Badt, H. Schindler, and N. S. Sariciftci, "The interplay of efficiency and morphology in photovoltaic devices based on interpenetrating networks of conjugated polymers with fullerenes," *Synthetic Metals*, vol. 118, no. 1-3, pp. 1–9, 2001.

[112] E. Moons, "Conjugated polymer blends: linking film morphology to performance of light emitting diodes and photodiodes," *Journal of Physics-Condensed Matter*, vol. 14, no. 47, pp. 12235–12260, 2002.

[113] H. Hoppe, M. Niggemann, C. Winder, J. Kraut, R. Hiesgen, A. Hinsch, D. Meissner, and N. S. Sariciftci, "Nanoscale morphology of conjugated polymer/fullerene-based bulk-heterojunction solar cells," *Advanced Functional Materials*, vol. 14, no. 10, pp. 1005–1011, 2004.

[114] A. Kumar, G. Li, Z. Hong, and Y. Yang, "High efficiency polymer solar cells with vertically modulated nanoscale morphology.," *Nanotechnology*, vol. 20, p. 165202, Apr. 2009.

[115] B. Walker, A. B. Tamayo, X.-D. Dang, P. Zalar, J. H. Seo, A. Garcia, M. Tantiwiwat, and T.-Q. Nguyen, "Nanoscale Phase Separation and High Photovoltaic Efficiency in Solution-Processed, Small-Molecule Bulk Heterojunction Solar Cells," *Advanced Functional Materials*, vol. 19, pp. 3063–3069, Oct. 2009.

[116] G. Chamberlain, "Organic solar cells: A review," *Solar Cells*, vol. 8, pp. 47–83, Feb. 1983.

[117] G. Yu, J. Gao, J. C. Hummelen, F. Wudl, and A. J. Heeger, "Polymer Photovoltaic Cells: Enhanced Efficiencies via a Network of Internal Donor-Acceptor Heterojunctions," *Science*, vol. 270, pp. 1789–1791, Dec. 1995.

[118] M. Reyes-Reyes, K. Kim, J. Dewald, R. López-Sandoval, A. Avadhanula, S. Curran, and D. L. Carroll, "Meso-structure formation for enhanced organic photovoltaic cells.," *Organic Letters*, vol. 7, pp. 5749–5752, Dec. 2005.

[119] H. Xin, F. S. Kim, and S. A. Jenekhe, "Highly efficient solar cells based on poly(3-butylthiophene) nanowires.," *Journal of the American Chemical Society*, vol. 130, pp. 5424–5425, Apr. 2008.

[120] S. S. Van-Bavel, E. Sourty, G. de With, and J. Loos, "Three-dimensional nanoscale organization of bulk heterojunction polymer solar cells.," *Nano Letters*, vol. 9, pp. 507–513, Feb. 2009.

[121] S. A. McClure, B. J. Worfolk, D. A. Rider, R. T. Tucker, J. A. M. Fordyce, M. D. Fleischauer, K. D. Harris, M. J. Brett, and J. M. Buriak, "Electrostatic layer-by-layer assembly of CdSe nanorod/polymer nanocomposite thin films.," *ACS applied materials & interfaces*, vol. 2, pp. 219–29, Jan. 2010.

[122] M. Hirade, H. Nakanotani, M. Yahiro, and C. Adachi, "Formation of organic crystalline nanopillar arrays and their application to organic photovoltaic cells.," *ACS Applied Materials & Interfaces*, vol. 3, pp. 80–3, Jan. 2011.

[123] J. L. Yang, S. Schumann, and T. S. Jones, "Nanowire-array films of copper hexadecafluorophthalocyanine (F_{16}CuPc) fabricated by templated growth," *Journal of Materials Chemistry*, vol. 21, no. 15, p. 5812, 2011.

[124] D. A. Rider, K. D. Harris, D. Wang, J. Bruce, M. D. Fleischauer, R. T. Tucker, M. J. Brett, and J. M. Buriak, "Thienylsilane-modified indium tin oxide as an anodic interface in polymer/fullerene solar cells.," *ACS applied materials & interfaces*, vol. 1, pp. 279–88, Feb. 2009.

[125] G. K. Kiema, M. J. Colgan, and M. J. Brett, "Dye sensitized solar cells incorporating obliquely deposited titanium oxide layers," *Solar Energy Materials & Solar Cells*, vol. 85, pp. 321–331, Jan. 2005.

[126] N. J. Gerein, M. D. Fleischauer, and M. J. Brett, "Effect of TiO_2 film porosity and thermal processing on TiO_2-P3HT hybrid materials and photovoltaic device performance," *Solar Energy Materials & Solar Cells*, vol. 94, pp. 2343–2350, Sept. 2010.

[127] J. G. Van Dijken, M. D. Fleischauer, and M. J. Brett, "Morphology Control of CuPc Thin Films Using Glancing Angle Deposition," *PVSC: 2008 33rd IEEE Photovoltaic Specialists Conference*, vol. 1-4, pp. 1222–1225, 2008.

[128] N. Li and S. R. Forrest, "Tilted bulk heterojunction organic photovoltaic cells grown by oblique angle deposition," *Applied Physics Letters*, vol. 95, no. 12, p. 123309, 2009.

[129] J. G. Van Dijken, M. D. Fleischauer, and M. J. Brett, "Solvent effects on ZnPc thin films and their role in fabrication of nanostructured organic solar cells," *Organic Electronics*, vol. 12, pp. 2111–2119, Dec. 2011.

[130] J. G. Van Dijken, M. D. Fleischauer, and M. J. Brett, "Controlled nanostructuring of CuPc thin films via glancing angle deposition for idealized organic photovoltaic architectures," *Journal of Materials Chemistry*, vol. 21, pp. 1013–1019, Jan. 2011.

[131] R. Steim, S. A. Choulis, P. Schilinsky, and C. J. Brabec, "Interface modification for highly efficient organic photovoltaics," *Applied Physics Letters*, vol. 92, no. 9, 2008.

[132] R. Steim, F. R. Kogler, and C. J. Brabec, "Interface materials for organic solar cells," *Journal of Materials Chemistry*, vol. 20, no. 13, p. 2499, 2010.

[133] H. Ma, H.-L. Yip, F. Huang, and A. K.-Y. Jen, "Interface Engineering for Organic Electronics," *Advanced Functional Materials*, vol. 20, pp. 1371–1388, Apr. 2010.

[134] H. Ma, H.-L. Yip, F. Huang, and A. K.-Y. Jen, "Interface Engineering for Organic Electronics," *Advanced Functional Materials*, vol. 20, pp. 1371–1388, Apr. 2010.

[135] C. H. Hsieh, Y. J. Cheng, P. J. Li, C. H. Chen, M. Dubosc, R. M. Liang, and C. S. Hsu, "Highly Efficient and Stable Inverted Polymer Solar Cells Integrated with a Cross-Linked Fullerene Material as an Interlayer," *Journal of the American Chemical Society*, vol. 132, no. 13, pp. 4887–4893, 2010.

[136] V. Shrotriya, G. Li, Y. Yao, C. W. Chu, and Y. Yang, "Transition metal oxides as the buffer layer for polymer photovoltaic cells," *Applied Physics Letters*, vol. 88, no. 7, 2006.

[137] G. Li, C.-W. Chu, V. Shrotriya, J. Huang, and Y. Yang, "Efficient inverted polymer solar cells," *Applied Physics Letters*, vol. 88, no. 25, p. 253503, 2006.

[138] L. Motiei, Y. Yao, J. Choudhury, H. Yan, T. J. Marks, M. E. van der Boom, and A. Facchetti, "Self-propagating molecular assemblies as interlayers for efficient inverted bulk-heterojunction solar cells.," *Journal of the American Chemical Society*, vol. 132, pp. 12528–12530, Sept. 2010.

[139] H.-H. Liao, L.-M. Chen, Z. Xu, G. Li, and Y. Yang, "Highly efficient inverted polymer solar cell by low temperature annealing of Cs_2CO_3 interlayer," *Applied Physics Letters*, vol. 92, no. 17, p. 173303, 2008.

[140] C. Uhrich, D. Wynands, S. Olthof, M. K. Riede, K. Leo, S. Sonntag, B. Maennig, and M. Pfeiffer, "Origin of open circuit voltage in planar and bulk heterojunction organic thin-film photovoltaics depending on doped transport layers," *Journal of Applied Physics*, vol. 104, no. 4, 2008.

[141] M. Glatthaar, M. Niggemann, B. Zimmermann, P. Lewer, M. Riede, A. Hinsch, and J. Luther, "Organic solar cells using inverted layer sequence," *Thin Solid Films*, vol. 491, no. 1-2, pp. 298–300, 2005.

[142] T. Ameri, G. Dennler, C. Waldauf, P. Denk, K. Forberich, M. C. Scharber, C. J. Brabec, and K. Hingerl, "Realization, characterization, and optical modeling of inverted bulk-heterojunction organic solar cells," *Journal of Applied Physics*, vol. 103, no. 8, 2008.

[143] T. Ameri, G. Dennler, C. Lungenschmied, and C. J. Brabec, "Organic tandem solar cells: A review," *Energy & Environmental Science*, vol. 2, no. 4, pp. 347–363, 2009.

[144] J. Y. Kim, K. Lee, N. E. Coates, D. Moses, T.-Q. Nguyen, M. Dante, and A. J. Heeger, "Efficient tandem polymer solar cells fabricated by all-solution processing.," *Science (New York, N.Y.)*, vol. 317, pp. 222–5, July 2007.

[145] G. Dennler, M. C. Scharber, T. Ameri, P. Denk, K. Forberich, C. Waldauf, and C. J. Brabec, "Design rules for donors in bulk-heterojunction tandem solar cells-towards 15 % energy-conversion efficiency," *Advanced Materials*, vol. 20, no. 3, pp. 579–583, 2008.

[146] S. Duclos, R. Haddon, S. Glarum, A. Hebard, and K. Lyons, "The influence of oxygen on the Raman spectrum of C_{60} films," *Solid State Communications*, vol. 80, pp. 481–484, Nov. 1991.

[147] L. Tsetseris and S. Pantelides, "Oxygen and water-related impurities in C_{60} crystals: A density-functional theory study," *Physical Review B*, vol. 82, pp. 1–5, July 2010.

[148] A. Fartash, "Dielectric properties of orientationally ordered/disordered C_{60}(111) films," *Physical Review B*, vol. 54, pp. 17215–17222, Dec. 1996.

[149] E. J. Meijer, C. Detcheverry, P. J. Baesjou, E. van Veenendaal, D. M. de Leeuw, and T. M. Klapwijk, "Dopant density determination in disordered organic field-effect transistors," *Journal of Applied Physics*, vol. 93, no. 8, pp. 4831–4835, 2003.

[150] I. Kymissis, C. Dimitrakopoulos, and S. Purushothaman, "High-performance bottom electrode organic thin-film transistors," *IEEE Transactions on Electron Devices*, vol. 48, pp. 1060–1064, June 2001.

[151] C. Reese and Z. Bao, "Organic single-crystal field-effect transistors," *Materials Today*, vol. 10, pp. 20–27, Mar. 2007.

[152] H. E. Katz, A. J. Lovinger, J. Johnson, C. Kloc, T. Siegrist, W. Li, Y. Y. Lin, and A. Dodabalapur, "A soluble and air-stable organic semiconductor with high electron mobility," *Nature*, vol. 404, no. 6777, pp. 478–481, 2000.

[153] M. Kitamura and Y. Arakawa, "High-performance pentacene thin-film transistors with high dielectric constant gate insulators," *Applied Physics Letters*, vol. 89, no. 22, p. 223525, 2006.

[154] M. Kitamura, Y. Kuzumoto, W. Kang, S. Aomori, and Y. Arakawa, "High conductance bottom-contact pentacene thin-film transistors with gold-nickel adhesion layers," *Applied Physics Letters*, vol. 97, no. 3, p. 033306, 2010.

[155] D. Kumaki, T. Umeda, and S. Tokito, "Reducing the contact resistance of bottom-contact pentacene thin-film transistors by employing a MoO_x carrier injection layer," *Applied Physics Letters*, vol. 92, no. 1, p. 013301, 2008.

[156] M. Kitamura, S. Aomori, J. H. Na, and Y. Arakawa, "Bottom-contact fullerene C_{60} thin-film transistors with high field-effect mobilities," *Applied Physics Letters*, vol. 93, no. 3, p. 033313, 2008.

[157] M. Kitamura, Y. Kuzumoto, S. Aomori, M. Kamura, J. H. Na, and Y. Arakawa, "Threshold voltage control of bottom-contact n-channel organic thin-film transistors using modified drain/source electrodes," *Applied Physics Letters*, vol. 94, no. 8, p. 083310, 2009.

[158] M. Kitamura, Y. Kuzumoto, M. Kamura, S. Aomori, and Y. Arakawa, "High-performance fullerene C_{60} thin-film transistors operating at low voltages," *Applied Physics Letters*, vol. 91, no. 18, p. 183514, 2007.

[159] S. Tiwari and N. C. Greenham, "Charge mobility measurement techniques in organic semiconductors," *Optical and Quantum Electronics*, vol. 41, pp. 69–89, Aug. 2009.

[160] A. F. Stassen, R. W. I. de Boer, N. N. Iosad, and A. F. Morpurgo, "Influence of the gate dielectric on the mobility of rubrene single-crystal field-effect transistors," *Applied Physics Letters*, vol. 85, no. 17, p. 3899, 2004.

[161] W. Li, C. Du, F. Li, Y. Zhou, M. Fahlman, Z. Bo, and F. Zhang, "Benzothiadiazole-Based Linear and Star Molecules: Design, Synthesis, and Their Application in Bulk Heterojunction Organic Solar Cells," *Chemistry of Materials*, vol. 21, pp. 5327–5334, Nov. 2009.

[162] D. S. Park, S. J. Kang, H. J. Kim, M. H. Jang, M. Noh, K.-H. Yoo, C. N. Whang, Y. S. Lee, and M. H. Lee, "Characteristics of perylene-based organic thin-film transistor with octadecyltrichlorosilane monolayer," *Journal of Vacuum Science & Technology B: Microelectronics and Nanometer Structures*, vol. 23, no. 3, p. 926, 2005.

[163] A. R. Spurr, "A low-viscosity epoxy resin embedding medium for electron microscopy," *Journal of Ultrastructure Research*, vol. 26, pp. 31–43, Jan. 1969.

[164] W. Krakow, N. M. Rivera, R. A. Roy, R. S. Ruoff, and J. J. Cuomo, "The growth of crystalline vapor deposited C_{60} thin films," *Applied Physics A: Materials Science & Processing*, vol. 56, pp. 185–192, Mar. 1993.

[165] W. Krakow, N. Rivera, R. Roy, R. Ruoff, and J. Cuomo, "Epitaxial growth of C_{60} thin films on mica," *Journal of Materials Research*, vol. 7, pp. 784–787, Jan. 1992.

[166] H. Zhang, C. Wu, L. Liang, Y. Chen, Y. He, Y. Zhu, N. Ke, J. B. Xu, S. P. Wong, A. Wei, and S. Peng, "Structural, morphological and optical properties of C_{60} cluster thin films produced by thermal evaporation under argon gas," *Journal of Physics: Condensed Matter*, vol. 13, pp. 2883–2889, Apr. 2001.

[167] U. Schwarz, W. Allers, G. Gensterblum, J.-J. Pireaux, and R. Wiesendanger, "Growth of C_{60} thin films on GeS(001) studied by scanning force microscopy," *Physical Review B*, vol. 52, pp. 5967–5976, Aug. 1995.

[168] D. Vick, T. Smy, and M. J. Brett, "Growth behavior of evaporated porous thin films," *Journal of Materials Research*, vol. 17, pp. 2904–2911, Jan. 2002.

[169] S. Günes, H. Neugebauer, and N. S. Sariciftci, "Conjugated polymer-based organic solar cells.," *Chemical reviews*, vol. 107, pp. 1324–1338, Apr. 2007.

[170] Y. Yoshida, T. Nobutaka, and Y. Kiyoshi, "In situ observation of the in-plane structure of C_{60} thin films on metal substrates prepared by molecular beam deposition," *Thin Solid Films*, vol. 281-282, pp. 80–83, 1996.

[171] J. Zhang, I. Salzmann, S. Rogaschewski, J. P. Rabe, N. Koch, F. Zhang, and Z. Xu, "Arrays of crystalline C_{60} and pentacene nanocolumns," *Applied Physics Letters*, vol. 90, no. 19, p. 193117, 2007.

[172] C. Elschner, A. A. Levin, L. Wilde, J. Grenzer, C. Schroer, K. Leo, and M. Riede, "Determining the C_{60} molecular arrangement in thin films by means of X-ray diffraction," *Journal of Applied Crystallography*, vol. 44, pp. 983–990, 2011.

[173] M. Birkholz, P. F. Fewster, and C. Genzel, *Thin Film Analysis by X-Ray Scattering*. Weinheim: WILEY-VCH Verlag GmbH & Co. KGaA, 2005.

[174] T. Karabacak, A. Mallikarjunan, J. P. Singh, D. Ye, G.-C. Wang, and T.-M. Lu, "β-phase tungsten nanorod formation by oblique-angle sputter deposition," *Applied Physics Letters*, vol. 83, no. 15, pp. 3096–3098, 2003.

[175] J. Huang, Z. Xu, and Y. Yang, "Low-Work-Function Surface Formed by Solution-Processed and Thermally Deposited Nanoscale Layers of Cesium Carbonate," *Advanced Functional Materials*, vol. 17, pp. 1966–1973, Aug. 2007.

[176] "CRC Handbook of Chemistry and Physics (Internet Version 2013)," ch. Section 15, Boca Raton, FL: CRC Press / Taylor and Francis, 93rd ed., 2013.

[177] Z. Bao and A. J. Lovinger, "Soluble Regioregular Polythiophene Derivatives as Semiconducting Materials for Field-Effect Transistors," *Chemistry of Materials*, vol. 11, pp. 2607–2612, Sept. 1999.

[178] P. C. Ewbank, R. S. Loewe, L. Zhai, J. Reddinger, G. Sauvé, and R. D. McCullough, "Regioregular poly(thiophene-3-alkanoic acid)s: water soluble conducting polymers suitable for chromatic chemosensing in solution and solid state," *Tetrahedron*, vol. 60, pp. 11269–11275, Nov. 2004.

[179] P. Bäuerle, K.-U. Gaudl, F. Würthner, N. S. Sariciftci, M. Mehring, H. Neugebauer, C. Zhong, and K. Doblhofer, "Synthesis and properties of carboxy-functionalized poly(3-alkylthienylenes)," *Advanced Materials*, vol. 2, pp. 490–494, Oct. 1990.

[180] K. D. Harris, K. L. Westra, and M. J. Brett, "Fabrication of Perforated Thin Films with Helical and Chevron Pore Shapes," *Electrochemical and Solid-State Letters*, vol. 4, no. 6, pp. C39–C42, 2001.

[181] V. D. Mihailetchi, H. Xie, B. de Boer, L. M. Popescu, J. C. Hummelen, P. W. M. Blom, and L. J. A. Koster, "Origin of the enhanced performance in poly(3-hexylthiophene): [6,6]-phenyl C_{61}-butyric acid methyl ester solar cells upon slow drying of the active layer," *Applied Physics Letters*, vol. 89, no. 1, p. 012107, 2006.

[182] M. D. Perez, C. Borek, S. R. Forrest, and M. E. Thompson, "Molecular and morphological influences on the open circuit voltages of organic photovoltaic devices.," *Journal of the American Chemical Society*, vol. 131, pp. 9281–9286, July 2009.

[183] T. Ohno, Y. Chen, S. Harvey, G. Kroll, J. Weaver, R. Haufler, and R. Smalley, "C_{60} bonding and energy-level alignment on metal and semiconductor surfaces," *Physical Review B*, vol. 44, pp. 13747–13755, Dec. 1991.

[184] S. L. Ren, Y. Wang, A. M. Rao, E. McRae, J. M. Holden, T. Hager, K. Wang, W.-T. Lee, H. F. Ni, J. Selegue, and P. C. Eklund, "Ellipsometric determination of the optical constants of C_{60} (Buckminsterfullerene) films," *Applied Physics Letters*, vol. 59, no. 21, pp. 2678–2680, 1991.

[185] S. Pfuetzner, J. Meiss, A. Petrich, M. Riede, and K. Leo, "Improved bulk heterojunction organic solar cells employing C_{70} fullerenes," *Applied Physics Letters*, vol. 94, no. 22, p. 223307, 2009.

[186] M. Shtein, H. F. Gossenberger, J. B. Benziger, and S. R. Forrest, "Material transport regimes and mechanisms for growth of molecular organic thin films using low-pressure organic vapor phase deposition," *Journal of Applied Physics*, vol. 89, no. 2, pp. 1470–1476 ST – Material transport regimes and mec, 2001.

[187] G. Wei, S. Wang, K. Renshaw, M. E. Thompson, and S. R. Forrest, "Solution-processed squaraine bulk heterojunction photovoltaic cells.," *ACS nano*, vol. 4, pp. 1927–34, Apr. 2010.

[188] A. Sánchez-Díaz, R. Pacios, U. Muñecas, T. Torres, and E. Palomares, "Charge transfer reactions in near IR absorbing small molecule solution processed organic bulk-heterojunction solar," *Organic Electronics*, vol. 12, pp. 329–335, Feb. 2011.

[189] R. Pandey and R. J. Holmes, "Graded donor-acceptor heterojunctions for efficient organic photovoltaic cells.," *Advanced materials (Deerfield Beach, Fla.)*, vol. 22, pp. 5301–5, Dec. 2010.

[190] Y. Zheng, R. Bekele, J. Ouyang, and J. Xue, "Organic photovoltaic cells with vertically aligned crystalline molecular nanorods," *Organic Electronics*, vol. 10, pp. 1621–1625, Dec. 2009.

[191] P. Sullivan, S. Heutz, S. M. Schultes, and T. S. Jones, "Influence of codeposition on the performance of CuPc-C_{60} heterojunction photovoltaic devices," *Applied Physics Letters*, vol. 84, no. 7, p. 1210, 2004.

[192] F. Machui, S. Rathgeber, N. Li, T. Ameri, and C. J. Brabec, "Influence of a ternary donor material on the morphology of a P3HT:PCBM blend for organic photovoltaic devices," *Journal of Materials Chemistry*, vol. 22, no. 31, p. 15570, 2012.

[193] M. Anderson, V. Williams, T. Schuerlein, G. Collins, C. England, L.-K. Chau, P. Lee, K. Nebesny, and N. Armstrong, "RHEED and optical characterization of ordered multilayers of phthalocyanine/C_{60} and phthalocyanine/perylene-tetracarboxylicdianhydride (PTCDA)," *Surface Science*, vol. 307-309, pp. 551–558, Apr. 1994.

[194] J. Danziger, J. P. Dodelet, P. Lee, K. W. Nebesny, and N. R. Armstrong, "Heterojunctions formed from phthalocyanine and perylene thin films: photoelectrochemical characterization," *Chemistry of Materials*, vol. 3, pp. 821–829, Sept. 1991.

[195] R. Lof, M. van Veenendaal, B. Koopmans, H. Jonkman, and G. Sawatzky, "Band gap, excitons, and Coulomb interaction in solid C_{60}," *Physical Review Letters*, vol. 68, pp. 3924–3927, June 1992.

[196] I. Hill, A. Kahn, Z. Soos, and R. Pascal, Jr, "Charge-separation energy in films of π-conjugated organic molecules," *Chemical Physics Letters*, vol. 327, pp. 181–188, Sept. 2000.

[197] R. Schlaf, B. A. Parkinson, P. A. Lee, K. W. Nebesny, and N. R. Armstrong, "HOMO/LUMO Alignment at PTCDA/ZnPc and PTCDA/-ClInPc Heterointerfaces Determined by Combined UPS and XPS Measurements," *The Journal of Physical Chemistry B*, vol. 103, pp. 2984–2992, Apr. 1999.

[198] N. C. Nicolaidis, B. S. Routley, J. L. Holdsworth, W. J. Belcher, X. Zhou, and P. C. Dastoor, "Fullerene Contribution to Photocurrent Generation in Organic Photovoltaic Cells," *The Journal of Physical Chemistry C*, vol. 115, pp. 7801–7805, Apr. 2011.

[199] Y. Yao, C. Shi, G. Li, V. Shrotriya, Q. Pei, and Y. Yang, "Effects of C_{70} derivative in low band gap polymer photovoltaic devices: Spectral complementation and morphology optimization," *Applied Physics Letters*, vol. 89, no. 15, p. 153507, 2006.

[200] S. T. Lee, X. Y. Hou, M. G. Mason, and C. W. Tang, "Energy level alignment at Alq/metal interfaces," *Applied Physics Letters*, vol. 72, no. 13, p. 1593, 1998.

[201] C. Shen and A. Kahn, "The role of interface states in controlling the electronic structure of Alq3/reactive metal contacts," *Organic Electronics*, vol. 2, pp. 89–95, Sept. 2001.

[202] E. Tsiper, Z. Soos, W. Gao, and A. Kahn, "Electronic polarization at surfaces and thin films of organic molecular crystals: PTCDA," *Chemical Physics Letters*, vol. 360, pp. 47–52, July 2002.

[203] J. S. Kim, M. Granström, R. H. Friend, N. Johansson, W. R. Salaneck, R. Daik, W. J. Feast, and F. Cacialli, "Indium-tin oxide treatments for single- and double-layer polymeric light-emitting diodes: The relation between the anode physical, chemical, and morphological properties and the device performance," *Journal of Applied Physics*, vol. 84, no. 12, p. 6859, 1998.

[204] I. G. Hill, A. Rajagopal, A. Kahn, and Y. Hu, "Molecular level alignment at organic semiconductor-metal interfaces," *Applied Physics Letters*, vol. 73, no. 5, p. 662, 1998.

[205] S. Veenstra, A. Heeres, G. Hadziioannou, G. Sawatzky, and H. Jonkman, "On interface dipole layers between C_{60} and Ag or Au," *Applied Physics A: Materials Science & Processing*, vol. 75, pp. 661–666, Dec. 2002.

[206] D. Purdie, H. Bernhoff, and B. Reihl, "The electronic structure of Ag(110)c(4x4)C_{60} and Au(110)(6x5)C_{60}," *Surface Science*, vol. 364, pp. 279–286, Sept. 1996.

[207] S. W. Cho, L. F. J. Piper, A. DeMasi, A. R. H. Preston, K. E. Smith, K. V. Chauhan, P. Sullivan, R. A. Hatton, and T. S. Jones, "Electronic Structure of C_{60} /Phthalocyanine/ITO Interfaces Studied using Soft X-ray Spectroscopies," *The Journal of Physical Chemistry C*, vol. 114, pp. 1928–1933, Feb. 2010.

[208] S. H. Park, J. G. Jeong, H. J. Kim, M. H. Cho, S. W. Cho, Y. Yi, M. Y. Heo, and H. Sohn, "The electronic structure of C_{60}/ZnPc interface for organic photovoltaic device with blended layer architecture," *Applied Physics Letters*, vol. 96, no. 1, 2010.

[209] Y. Hirose, A. Kahn, V. Aristov, P. Soukiassian, V. Bulovic, and S. Forrest, "Chemistry and electronic properties of metal-organic semiconductor interfaces: Al, Ti, In, Sn, Ag, and Au on PTCDA," *Physical Review B*, vol. 54, pp. 13748–13758, Nov. 1996.

[210] S. Duhm, A. Gerlach, I. Salzmann, B. Bröker, R. Johnson, F. Schreiber, and N. Koch, "PTCDA on Au(111), Ag(111) and Cu(111): Correlation

of interface charge transfer to bonding distance," *Organic Electronics*, vol. 9, pp. 111–118, Feb. 2008.

[211] E. Kawabe, H. Yamane, R. Sumii, K. Koizumi, Y. Ouchi, K. Seki, and K. Kanai, "A role of metal d-band in the interfacial electronic structure at organic/metal interface: PTCDA on Au, Ag and Cu," *Organic Electronics*, vol. 9, pp. 783–789, Oct. 2008.

[212] Y. Zou, L. Kilian, A. Schöll, T. Schmidt, R. Fink, and E. Umbach, "Chemical bonding of PTCDA on Ag surfaces and the formation of interface states," *Surface Science*, vol. 600, pp. 1240–1251, Mar. 2006.

[213] P. Avouris, P. Bagus, and C. Nelin, "Unfilled levels and excited states of adsorbates on metal surfaces," *Journal of Electron Spectroscopy and Related Phenomena*, vol. 38, pp. 269–287, Jan. 1986.

[214] C. Dimitrakopoulos and P. Malenfant, "Organic Thin Film Transistors for Large Area Electronics," *Advanced Materials*, vol. 14, pp. 99–117, Jan. 2002.

[215] J. R. Ostrick, A. Dodabalapur, L. Torsi, A. J. Lovinger, E. W. Kwock, T. M. Miller, M. Galvin, M. Berggren, and H. E. Katz, "Conductivity-type anisotropy in molecular solids," *Journal of Applied Physics*, vol. 81, no. 10, p. 6804, 1997.

[216] C. D. Dimitrakopoulos, A. R. Brown, and A. Pomp, "Molecular beam deposited thin films of pentacene for organic field effect transistor applications," *Journal of Applied Physics*, vol. 80, no. 4, p. 2501, 1996.

[217] T. Matsushima, M. Yahiro, and C. Adachi, "Estimation of electron traps in C_{60} field-effect transistors by a thermally stimulated current technique," *Applied Physics Letters*, vol. 91, no. 10, p. 103505, 2007.

[218] X. Lu, T. Minari, A. Kumatani, C. Liu, and K. Tsukagoshi, "Effect of air exposure on metal/organic interface in organic field-effect transistors," *Applied Physics Letters*, vol. 98, no. 24, p. 243301, 2011.

[219] M. Kitamura, S. Aomori, J. H. Na, and Y. Arakawa, "Bottom-contact fullerene C_{60} thin-film transistors with high field-effect mobilities," *Applied Physics Letters*, vol. 93, no. 3, p. 033313, 2008.

[220] M. O. Jensen and M. J. Brett, "Periodically structured glancing angle deposition thin films," *IEEE Transactions on Nanotechnology*, vol. 4, no. 2, pp. 269–277, 2005.